# Natural and Mixed Convection in Coarse-grained Porous Media

Ataei Dadavi, Iman

**DOI**
10.4233/uuid:0eee75bb-fe64-4d21-939c-6d1180673cd7

**Publication date**
2020

**Document Version**
Final published version

**Citation (APA)**
Ataei Dadavi, I. (2020). *Natural and Mixed Convection in Coarse-grained Porous Media*. [Dissertation (TU Delft), Delft University of Technology]. https://doi.org/10.4233/uuid:0eee75bb-fe64-4d21-939c-6d1180673cd7

**Important note**
To cite this publication, please use the final published version (if applicable).
Please check the document version above.

# Natural and Mixed Convection in Coarse-grained Porous Media

# Natural and Mixed Convection in Coarse-grained Porous Media

## Dissertation

for the purpose of obtaining the degree of doctor
at Delft University of Technology
by the authority of the Rector Magnificus, Prof. dr. ir. T.H.J.J. van der Hagen,
chair of the Board for Doctorates
to be defended publicly on
Wednesday 29 April 2020 at 10:00 o'clock

by

**Iman ATAEI DADAVI**

Master of Science in Aerospace Engineering, Sharif University of Technology, Iran

born in Qaemshahr, Iran

This dissertation has been approved by the promotors.

Composition of the doctoral committee:

| | |
|---|---|
| Rector Magnificus, | chairperson |
| Prof. dr. ir. C. R. Kleijn | Delft University of Technology, promotor |
| Dr. ir. M. J. Tummers | Delft University of Technology, copromotor |

Independent members:

| | |
|---|---|
| Prof. dr. ir. J. Westerweel | Delft University of Technology |
| Prof. dr. ir. B. J. Boersma | Delft University of Technology |
| Prof. dr. ir. D. M. J. Smeulders | Eindhoven University of Technology |
| Prof. dr. Philipp Rudolf von Rohr | ETH Zurich |

Other members:

| | |
|---|---|
| Ir. D. van der Plas | Tata Steel in Europe |

This research was carried out at Delft University of Technology under project number S41.5.14526b in the framework of the Partnership Program of the Material innovation institute M2i (www.m2i.nl) and the Technology Foundation TTW (www.stw.nl), which is part of the Netherlands Organization for Scientific Research (www.nwo.nl). This work is also partly funded by Tata Steel in Europe.


*Keywords:* Natural convection; Mixed convection; Heat transfer; Porous media; Particle Image Velocimetry; Liquid Crystal Thermography

*Cover:* An image taken from liquid crystals in water in a side-heated cavity. The color distribution qualitatively represents the temperature distribution.

*Printed by:* Ridderprint | www.ridderprint.nl



ISBN 978-94-6375-893-2

An electronic version of this dissertation is available at

http://repository.tudelft.nl/

To my beautiful and lovely wife, Afsane,

to my devoted mother, Moluk,

and to the soul of my beloved father, Ali.

# Contents

# Summary

In the chain of steel production, the blast furnace converts iron ore into liquid iron. The hearth of the blast furnace, where the liquid metal is collected and tapped off, is filled with relatively large coke particles ($D$ ~ 20 – 100 mm). The meandering flow of hot liquid metal in the coarse-grained porous medium in the hearth causes erosion of the refractory walls containing the hearth through the formation of hot spots. This has a severe impact on the lifetime of blast furnaces. Therefore, it is crucial to understand the liquid metal flow and heat transfer through the packed bed of relatively large coke particles.

With the hot metal flowing in from the top and the refractory walls being cooled, the flow of the liquid metal in the hearth is a natural and mixed convection flow characterized by the dimensionless Rayleigh and Reynolds numbers, and their ratio, *viz.* the Richardson number. Since the pores between the large coke particles are not small compared to the flow and thermal length scales, there is a strong interaction between the flow and the pore geometry. Therefore, it is important to capture the details of fluid flow and temperature distribution at the pore level and to resolve the strong interaction between the flow and the solid grains.

In order to gain a fundamental understanding of the above types of flow, this dissertation reports on experimental investigations of natural and mixed convection in cubical cavities filled with coarse-grained porous media consisting of packed beds of relatively large solid spheres. Bottom-heated natural convection, side-heat natural convection, and vented mixed convection configurations have been considered. Accurate global heat transfer measurements have been performed for various sphere packings, sphere sizes, and sphere conductivities in a wide range of Rayleigh numbers (and Reynolds numbers in the mixed convection case). Refractive index matching between water and hydrogel spheres enabled the use of optical measurement techniques, *i.e.* Particle Image Velocimetry and Liquid Crystal Thermography, to obtain highly-resolved pore-scale velocity and temperature fields.

In bottom-heated natural convection, it was observed that at lower Rayleigh numbers, the Nusselt numbers for the porous medium-filled cavity are reduced compared to the pure-fluid cavity (Rayleigh-Bénard convection) and the Nusselt number reduction strongly depends on packing type, size, and conductivity of spheres. However, at high Rayleigh numbers, when the flow and thermal length scales become sufficiently smaller than the pore length scale, the flow penetrates into the pores with much higher velocities and is not obstructed by the presence of coarse-grained porous media. This leads to an asymptotic regime in which the convective heat transfer for all sphere conductivities, sizes and packing types converge into a single curve which is very close to the pure Rayleigh-Bénard

convection curve. The results indicate that the ratio between the thermal length scale and the pore length scale is a determining factor in the effect of porous media on flow and heat transfer.

In side-heated natural convection, the presence of the porous medium decreases the heat transfer compared to the corresponding pure-fluid cavity. This is due to the fact that the layers of the spheres touching the isothermal side walls hinder the boundary layers along these walls and divert a portion of the boundary layer fluid away from the walls. This subsequently alters the temperature distribution and reduces the mean temperature gradient at the walls. The heat transfer measurements demonstrate a transition from Darcy to non-Darcy regime by increasing the Rayleigh number and the size of spheres. A new Nusselt number correlation for coarse-grained porous is presented which takes into account the strong effect of the porous medium conductivity.

In vented mixed convection, three flow and heat transfer regimes were observed depending on the Richardson number. For $Ri < 10$, the porous medium directs a portion of the strong forced inflow downward towards the hot wall, and therefore the flow structure and the Nusselt number scaling are similar to pure forced convection and are independent of Rayleigh number. For $Ri > 40$, the strong upward directed natural convection flow dominates and the Nusselt number becomes less sensitive to the Reynolds number. For $10 < Ri < 40$, the upward directed natural convection flow competes with the downward directed forced flow at the hot wall, leading to a minimum effective Nusselt number. A Nusselt number correlation is presented which covers all three regimes.

This dissertation concludes by discussing the contribution of this work in improving the knowledge on the physics of natural and mixed convection in coarse-grained porous media and its relevance for understanding and modelling of the fluid flow and heat transfer processes in the blast furnace hearth, as well as in other application fields such as in air ventilation and in the food industry.

# Samenvatting

In het proces van staalproductie, converteert een hoogoven ijzererts in vloeibaar ijzer. De haard van de hoogoven, waar het vloeibare ijzer wordt verzameld en afgetapt, bevat een groot aantal brokken cokes ($D$ ~ 20 – 100 mm). De meanderende stroming van heet vloeibaar ijzer rondom het grofkorrelige poreuze medium in de haard van de hoogoven zorgt ervoor dat de vuurvaste muren eroderen door de formatie van hot-spots. Dit heeft tot directe gevolg dat de levensduur van de hoogoven omlaag gaat. Vandaar dat het essentieel is om te begrijpen hoe het vloeibare metaal en de warmte stroomt door het gepakte bed van relatief grote brokken cokes.

Met het hete vloeibare metaal wat van boven naar beneden vloeit en de wanden van de hoogoven die gekoeld worden, ontstaat er een natuurlijke en gemixte convectieve vloeistofstroming die gekarakteriseerd kan worden door de dimensie-loze Rayleigh en Reynolds getallen, en hun onderlinge ratio, *viz.* het Richardson getal. Vanwege het feit dat de poriën tussen de relatief grote coke-brokken niet kleiner zijn dan de vloeistof- en warmte lengte schalen, kan er gezegd worden dat er een sterke interactie bestaat tussen de vloeistofstroming en de geometrie van de poriën. Daarom is het belangrijk om de details van de vloeistofstroming en de temperatuur distributie vast te leggen op de schaal van de poriën en om de interactie tussen de stroming en de vaste brokken te bestuderen.

Om een fundamenteel begrip te kunnen krijgen van de bovengenoemde stromingstypen, rapporteert dit proefschrift op experimentele onderzoeken van natuurlijke en gemixte convectie in kubusvormige holtes gevuld met grofkorrelige poreuze media wat bestaat uit gepakte bedden van relatief grote bollen. Van onder verwarmde natuurlijke convectie, vanaf de zijkant verwarmde natuurlijke convectie en geventileerde gemixte convectie configuraties zijn in dit onderzoek overwogen en verricht. Nauwkeurige globale warmte transport meting zijn uitgevoerd voor verschillende bolpakkingen, bol-dimensies en bol-geleidingseigenschappen in een breed bereik van Rayleigh getallen (en Reynolds getallen in het geval van de gemixte convectie). Brekingsindex overeenkomsten tussen water en hydrogel-ballen maakte het gebruik van optische meetinstrumenttechnieken mogelijk, zoals Particle Image Velocimetry en Liquid Crystal Thermography, om op deze manier hoog kwalitatieve snelheids en temperatuurvelden te verkrijgen op de schaal van de poriën, waarmee wordt bedoeld de ruimte tussen de bollen en het vloeistof.

In het geval waar van onder verwarmde natuurlijke convectie werd bestudeerd, werden bij lage Rayleigh waarden, lagere Nusselt getallen geobserveerd voor het geval dat de kubusvormige holte was gevuld met de grofkorrelige poreuze media dan in het geval waarin de holte met enkel de vloeistof was gevuld (Rayleigh-Bénard convectie). Bovendien hangt in dit geval de reductie in het Nusselt getal sterk af van de pakkingsstructuur, dimensie en geleidingseigenschappen van de bollen. Hoewel, bij hogere Rayleigh waarden, wanneer de vloeistof- en warmtestroming lengte schalen

vele malen kleiner worden dan de poriën lengte-schalen, penetreert de stroming in de poriën met veel hogere stromingssnelheden en wordt het niet tegengehouden door de aanwezigheid van de grofkorrelige poreuze media. Dit leidt tot een asymptotisch regime waarin de convectieve warmte-transport voor alle geleidingseigenschappen, dimensies en pakkingsstructuren convergeert in een enkele curve die erg dichtbij de pure Rayleigh-Bénard convectie curve ligt. De resultaten laten zien dat de ratio tussen de warmte lengte schalen en de poriën lengte schalen een bepalende factor zijn in het effect van poreuze media op de vloeistof- en warmte transport.
In het geval waar vanaf de zijkant verwarmde convectie werd bestudeerd, werd geobserveerd dat de aanwezigheid van het poreuze medium de warmte-transport verminderd wanneer het wordt vergeleken met het geval dat de kubusvormige holte enkel gevuld was met de vloeistof. Dit is vanwege het feit dat de lagen van de bollen de isotherme zijwanden raken en zo de grenslagen langs deze wanden hinderen en op deze manier een gedeelte van de grenslaagvloeistof omleiden van de zijwanden. Dit zorgt er vervolgens voor dat de temperatuurs-distributie verandert en vermindert de gemiddelde temperatuurs-gradient langs de zijwanden. De warmtetransport metingen laten een transitie zien van het Darcy naar het non-Darcy regime door de Rayleigh-waarde te verhogen en de dimensies van de bollen. Een nieuwe Nusselt-correlatie voor grofkorrelige poreuze media wordt gepresenteerd waarin rekening wordt gehouden met het sterke effect van de geleidingseigenschappen van het poreuze medium.
In geventileerde gemixte convectie, zijn er in totaal drie vloeistofstromen en warmtetransport regimes geobserveerd die afhangen van het Richardson getal. Voor het geval waarin $Ri < 10$, wordt een deel van de sterk geforceerde instroom door het poreuze medium naar beneden richting de hete wand geleidt. Hierdoor zijn de stromingsstructuur en het geschaalde Nusselt-getal gelijk aan de pure geforceerde convectie geval en zijn op hun beurt onafhankelijk van het Rayleigh-getal. Voor het geval dat $Ri > 40$, domineert de sterke naar boven gerichte natuurlijke convectieve stroming en wordt het Nusselt-getal minder gevoelig voor het Reynolds getal. Voor het geval dan $10 < Ri < 40$, concurreert de naar boven gerichte natuurlijke convectieve stroming met de omlaag gerichte geforceerde stroming langs de hete wand, wat vervolgens leidt tot een minimaal effectieve Nusselt-waarde. Een Nusselt getal correlatie wordt gepresenteerd waarin alle drie bovengenoemde regimes mee worden genomen.
Dit proefschrift concludeert met het bediscussiëren van de contributie van dit werk in het verbeteren van de kennis omtrent de fysica van natuurlijke en gemixte convectie in grofkorrelige poreuze media en de relevantie voor het begrijpen en modelleren van vloeistofstromen en warmtestromen processen in de haard van de hoogoven, alsmede in andere toepassingsvelden zoals in luchtventilatie en in de voedselindustrie.

# Chapter 1

## Introduction

## 1.1 Application background

A blast furnace is a crucial element in the steelmaking industry. It is a complex counter-current reactor that converts iron ore into liquid iron. Fig. 1.1 shows a schematic of a typical blast furnace. Iron ore together with limestone and coke are added to the blast furnace from the top. Hot blast air is injected into the furnace through large nozzles and subsequently reacts with the ore and coke in the lower region of the blast furnace at high temperatures in the order of 2000 °C. The process gas flows up while molten iron flows down. At the bottom of the blast furnace, which is called hearth, the hot liquid metal is collected and tapped off. Apart from liquid metal, the hearth contains relatively large unburnt coke particles with a typical size of 5 to 10 cm. The meandering flow of hot liquid metal through the packed bed of coke particles in the hearth can cause erosion and wear of the refractory walls containing the hearth. Of particular importance is the formation of hot spots due to local temperature and heat transfer non-uniformities which have a severe negative impact on the lifetime of the refractory walls containing the hearth and thus on the productivity of the blast furnace. Therefore, it is crucial to understand the physics underlying the liquid metal flow and heat transfer through the packed bed of coke particles in the blast furnace hearth. The relatively large coke particles form a coarse-grained porous medium in which the pore length scale is not small compared to the flow and thermal length scales, resulting in a strong interaction between the pore geometry and the flow. With the hot liquid metal flowing into the hearth from the top and the walls containing the hearth being cooled from the outside, the flow of liquid metal in the hearth is in principle a natural convection flow in a coarse-grained porous medium. During the tapping process, the liquid metal in the hearth flows out via the tapholes. This imposes a forced flow on the system which has a comparable strength to that of the buoyancy-induced natural convection flow. The combination of natural and forced convection results in a complex mixed convection flow in a coarse-grained porous medium. The existing methods for simulation of fluid flow and heat transfer in porous media are not suitable for the flow condition in the hearth. The combination of very high Rayleigh number, high Reynolds number, low Prandtl number, and the coarse nature of the porous medium makes computational studies of such phenomenon very challenging [1]. Therefore, experimental studies of mixed convection flow in coarse-grained porous media in simplified geometries are needed to improve the understanding of the relevant physics and to provide detailed data on flow, temperature and heat transfer to validate developed simulation models.

## 1.2 Scientific background

The hearth of a blast furnace has a typical diameter of 5 – 8 m and a typical height of 2 – 3 m and is filled with a coarse-grained porous medium with typical pore length scales of 5 – 10 cm. Relevant dimensionless numbers and their typical values are the Rayleigh number $Ra \approx 10^{11}$, the Reynolds number $Re \approx 10^{5}$, and the Prandtl number $Pr \approx 10^{-1}$. This results in a mixed convection flow with intermediate Richardson numbers in the order of $Ri\ (= Ra/(Pr\ Re^2)) \approx 10 - 100$. This section gives an overview of the relevant literature on natural and mixed convection in porous media.

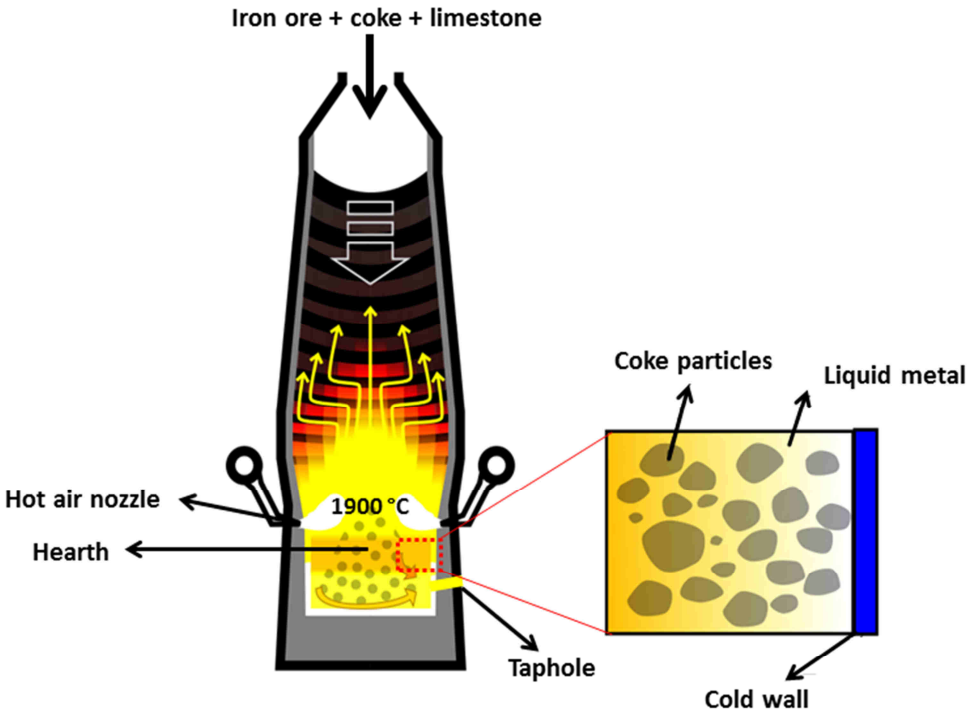


Fig. 1.1 Schematic representation of a blast furnace. In the hearth, hot liquid metal flows through a coarse-grained porous medium consisting of relatively large coke particles. The hearth is contained by refractory (side) walls that are cooled on the outside.

### 1.2.1 Natural and mixed convection

Natural convection occurs due to buoyancy as a result of density gradients in a fluid, which are induced by imposed temperature differences. Examples of natural convection in nature include atmospheric flows [2], oceanic flows [3,4], earth mantle convection [5,6], and convection in stars [7]. In engineering, natural convection plays an important role in, for example, building environment control [8], metal production [9], crystal growth [10], and electronics cooling [11]. For a given geometry, natural convection is characterized by two non-dimensional numbers: the Rayleigh number, which represents the ratio of buoyancy and

diffusive forces, and the Prandtl number, which is the ratio of kinematic viscosity and thermal diffusivity. The most important response of a fluid system to the Rayleigh number is the Nusselt number which is the dimensionless heat transfer coefficient.

There are two main categories in natural convection: heating from below and heating from the side. The case when a fluid is heated from below and cooled from above is known as Rayleigh-Bénard convection, and has attracted extensive research attention due to its simple geometry and rich physics. When the Rayleigh number exceeds a critical value, the stagnant fluid becomes unstable and the buoyancy-driven convection sets in. Different aspects that were considered in Rayleigh-Bénard studies, include the theoretical [12–14] and experimental [15–18] scaling rules for the Nusselt number, flow structures and the large scale circulation [19–22], the behavior of the boundary layers [23–25], and the effect of non-Boussinesq conditions [26–28]. Reviews on Rayleigh-Bénard convection are provided by Siggia [29] and Ahlers et al. [30].

In natural convection in enclosures that are differentially heated at two opposite vertical walls, there is no threshold for the onset of natural convection and the fluid becomes immediately unstable due to any small temperature difference. This results in ascending motion near the hot wall and descending motion near the cold wall. Flow and temperature fields, as well as the Nusselt number measurements in this configuration, have been the subject of several numerical [31–34] and experimental [35,36] investigations.

When a forced flow is added to a natural convection system, mixed convection occurs due to the mutual interaction of natural and forced convection. During the past decades, mixed convection has received considerable attention mainly due to its increasing importance in many engineering applications such as heat exchangers [37], chemical vapor deposition reactors [38,39], cooling of electronic devices [40,41], buildings ventilation [42,43] and urban air investigations [44,45].

In mixed convection, in addition to the Rayleigh and Prandtl numbers, the Reynolds number (representing the ratio of inertia forces to viscous forces) is also relevant. Furthermore, the Richardson number is frequently used to express the relative strength of natural convection and forced convection. Aside from the above-mentioned dimensionless numbers, the orientation of the forced flow with respect to the buoyancy-induced flow is a determining factor influencing the flow field and heat transfer in mixed convection. Consequently, mixed convection could also be divided into assisting mixed convection and opposing mixed convection. Both heat transfer behavior and flow structure have been studied in various mixed convection configurations such as mixed convection in rectangular channels [40,46], between horizontal plates [47,48], in vented enclosures [49,50], and in lid-driven enclosures [51–53]. In this investigation, we consider the vented enclosures

since it is more relevant to the mixed convection situation in the blast furnace hearth.

### 1.2.2 Natural and mixed convection in porous media

Convection in porous media has been the subject of many investigations due to its importance to applications in geothermal energy [54], chemical industry [55], oil production [56], and hydrogeology [57]. A large number of theoretical and numerical studies modeled convection in porous media using Darcy's law in conjunction with a volume-averaging approach [58–63]. Darcy's law is based on the assumption that inertia is negligible compared to viscous effects and thus the pore Reynolds number is in the order of 1 or less [64]. At high values of the Rayleigh number (which is the case in most engineering applications such as in blast furnace hearth), the inertia effects are important and Darcy's law does not hold. Moreover, when the pore length scales are not small compared to the flow and thermal length scales (i.e. in coarse-grained porous media), the Darcy model is no longer valid. Several studies have attempted to include inertia (Forchheimer extension) and viscous forces (Brinkman extension) to account for non-Darcian effects in convection in porous media [65–67]. Relatively few experimental studies have been conducted to verify the theoretical models and the studies are mostly limited to Nusselt number measurements [68–72].

The volume averaging approach has been used to solve the Darcy model and its extensions. In this approach, the porosity is accounted for in a volume-averaged sense, and quantities such as velocity and temperature are defined as spatial averages over sufficiently large volumetric elements that contain multiple pores; the so-called representative elementary volumes (REV). The length scale of a REV should be much larger than the pore length scale but yet smaller than the bulk flow and thermal length scales. Therefore, this approach is only valid for the fluid flow through fine-grained porous media e.g. through soil and sand in which the pore length scale is much smaller than the flow and thermal length scales.

In many engineering applications, such as the flow of liquid iron through the relatively large coke particles in the hearth of blast furnaces, the pore length scale is not small compared to flow and thermal length scales. Other examples include electronics cooling [73] and the cooling of agricultural products [74,75]. In these cases, there is a strong interaction between the flow and the pore geometry, and the suitability of Darcy's law and the volume-averaging approach is questionable, and it becomes more important to capture the details of fluid flow and temperature distribution at the pore level and to resolve the strong interaction between the flow and the solid grains.

During the last two decades with the increase of computational capacities, attempts have been made to numerically solve the Navier-Stokes and energy equations for

convection in porous media by using the high-resolution direct CFD approach, to determine the velocity and temperature fields at the pore level. These studies have mostly focused on either natural convection in two-dimensional differentially heated enclosures containing several disconnected solid blocks [76,77] or forced convection in fixed bed reactors [78,79]. A few studies have compared volume-averaged Darcy-based simulation results with direct CFD results for natural convection in porous media [80,81]. Despite the mentioned attempts to numerically simulate convection in porous media using CFD, detailed experimental data on velocity and temperature fields to validate these simulations is still missing. This investigation provides - for the first time - experimental high-resolution velocity and temperature measurements in natural and mixed convection flow in porous media to validate the existing and future CFD results.

### 1.2.3 Experimental study of convection in porous media/ refractive index matching

Previous experimental studies on natural convection in porous media have focused on overall heat transfer measurements. Due to technical difficulties, experimental data on the velocity and temperature fields in the pores had been missing. Over the past decades, many researchers have attempted to visualize and measure convection in porous media. The earliest studies were either qualitative flow visualizations [69,82,83] or single-point temperature measurements [71,80,84]. Shattuck et al. [41] were the first to measure velocity profiles in natural convection in a packed bed of spheres heated from below. They measured the vertically-averaged vertical velocity by using Magnetic Resonance Imaging (MRI). Since then, there have been no significant improvements in velocity and temperature measurements of natural convection flows inside the pores of porous media. In the present study, we have performed optical measurements using refractive index matching to determine the flow velocity and temperature fields in porous media at the pore level.

Particle Image Velocimetry (PIV) is an important optical technique to measure fluid flow characteristics with high spatial and temporal resolutions. However, this technique is not easily applicable in porous media, because the solid porous material interferes with the laser light sheet and the optical pathline of the camera by generating shadows or scattering light. A solution to this problem is to use transparent solid materials that have the same refractive index as that of the surrounding fluid. Refractive index matching is a well-established approach to visualize fluid flow in porous media [85], complex geometries [86], and particle suspensions [87]. Two categories of liquids have been considered to match the refractive index of transparent solid materials: aqueous salt solutions [88,89] and organic liquids [85,90]. The refractive indices of most of these refractive index

matching liquids are strongly temperature-dependent. Therefore, this method has only been used in isothermal flows, and PIV measurements in natural and mixed convection flows inside porous media have not been realized before due to the inherent temperature variations across the flow domain. This investigation uses a refractive index-matched fluid/solid pair with refractive indices that are much less sensitive to temperature variations, thus making it well-suited for refractive index matching in thermally driven flows.

## 1.3 Objectives

The main objective of this investigation is to improve the fundamental understanding of the underlying physics of natural and mixed convection flow and heat transfer in coarse-grained porous media and to provide insights into the flow and heat transfer processes in the blast furnace hearth. To achieve this objective, this research thoroughly investigates bottom-heated natural convection, side-heated natural convection, and vented mixed convection in cubical cavities filled with a porous medium consisting of relatively large spheres. Optical measurements (particle image velocimetry and liquid crystal thermography) in conjunction with accurate global heat transfer measurements were performed. This investigation addresses the question of whether the presence of coarse-grained porous media gives rise to hot spots as a result of local non-uniformities in heat transfer to the enclosure walls. The use of refractive index matching enabled measurement of the local pore-scale flow and temperature distributions inside the porous media and to visualize the interaction between the forced flow, the buoyancy-induced flow, and the grains. A secondary objective of this investigation is to provide detailed experimental data on flow, temperature, and heat transfer to validate and improve computational models which can be used in the steelmaking industry to enhance the understanding of the factors influencing the hearth process and to optimize the process towards improved protection of the hearth.

## 1.4 Outline of the thesis

The flow and heat transfer characteristics of bottom-heated natural convection, side-heated natural convection, and vented mixed convection in cubical cavities filled with coarse-grained porous media are investigated in chapters 2, 3 and 4, respectively. These chapters are self-contained articles that are published in scientific journals. The details of the experimental setups and the measurement techniques are described in each chapter.

Chapter 2 presents the results on the overall Nusselt number measurements in a bottom-heated cavity for various sphere conductivities, spheres sizes, and sphere packings. The measured flow and temperature fields were used to explain the

existence of two different heat transfer regimes, i.e., the reduced heat transfer regime and the asymptotic regime with high heat transfer.

Chapter 3 reports on the results of the same type of measurements for a side-heated cavity. The results indicate that the interaction between natural convection flow and the porous media is very different from that in the bottom-heated cavity. The measured flow and temperature fields show the mechanism by which the heat transfer is reduced. A new Nusselt number correlation for coarse-grained porous media is presented, and the transition from Darcy to non-Darcy behavior is discussed.

Chapter 4 presents the mixed convection heat transfer, flow and temperature fields results in a vented side-heated cavity for a wide range of Reynolds and Rayleigh numbers. Three heat transfer regimes are identified and discussed in detail using the flow, temperature, and heat transfer results. A Nusselt number correlation as a function of the Rayleigh and the Reynolds number is derived that is valid in all three regimes.

Chapter 5 presents the overall conclusions of the work and discuss the broader applicability of the findings and an outlook of future possibilities in this field.

# Chapter 2

## Flow and Heat Transfer Measurements in Natural Convection in Coarse-grained Porous Media*

This chapter reports on an experimental study of natural convection in an enclosure that is heated at the bottom and cooled at the top, filled with a packed bed of relatively large solid spheres. Nusselt numbers were measured for various sphere conductivities, spheres sizes and sphere packings for Rayleigh numbers varying between $10^7$ and $10^9$. The Nusselt number measurements showed that at lower Rayleigh numbers, the heat transfer is lower than that for pure Rayleigh-Bénard convection, with the difference depending on packing type, size, and conductivity of the spheres. However, at high Rayleigh numbers, there exists an asymptotic regime where the convective contribution of the total heat transfer for all sphere conductivities, sizes, and packing types collapse on a single curve which is very close to the curve for pure Rayleigh-Bénard convection. Refractive index-matching of the fluid and the solid spheres enabled the use of particle image velocimetry and liquid crystal thermography to obtain highly resolved velocity and temperature fields. The comparison of the velocity and temperature fields for the two heat transfer regimes showed that the velocity magnitudes inside the pores in the core region are much higher in the asymptotic regime than those in the low Rayleigh number regime, which lead to a deeper penetration of cold and hot fluid elements and higher heat transfer.

* This chapter has been published in the *International Journal of Heat and Mass Transfer*, 130, 575-584 (2019).

## 2.1 Introduction

Natural convection in porous media plays an important role in a range of physical and industrial applications such as steel and iron production, geothermal energy, chemical industries, oil production, and hydrogeology and therefore has attracted a great deal of attention. The most widely studied configuration in this field is that of a fluid-saturated porous medium bounded between two horizontal impermeable walls with the lower wall hotter than the upper one. A large number of numerical and theoretical studies have focused on modeling flow and heat transfer in this configuration. The frequently used Darcy model [61,91,92] assumes that inertia is negligible compared to viscous effects, and that the flow and thermal length scales are much larger than porous length scales. Other studies added inertia terms [62] or a quadratic drag term (Forchheimer equation) [67] to the Darcy model. Relatively few experimental studies have been performed to verify these models and most of them were only dedicated to heat transfer measurements at low Rayleigh numbers using fine grains where the Darcy assumptions hold [62,69,93].

In coarse-grained porous media, the length scales of the solid porous material are not small compared to the flow and thermal length scales in the fluid. This results in complex interactions between the flow and the solid, and the Darcy model is no longer valid. Very few experimental studies have been conducted using coarse-grained porous media. Kladias and Prasad [68] measured heat transfer in packed beds of spheres of varying bead diameters, solid materials, and fluids to validate the Darcy-Brinkman-Forchheimer (DBF) flow model. They observed that the DBF solutions are in agreement with the experimental results only at low Ra-numbers and for small spheres (low Darcy numbers). Keene and Goldstein [70] studied heat transfer across a 279×279×279 $mm^3$ cubical cell filled with 25.4 mm spherical polypropylene beads in simple cubic packing. They achieved high fluid Ra-numbers $1.68\times10^9 < Ra < 3.86\times10^{11}$ by using compressed argon as the saturating fluid with pressure varying from 5.6 to 77 bar. They also employed the data sets from [68] and reported that at high Ra-numbers the heat transfer in porous media asymptotes to the behavior of a homogeneous fluid layer, unless the solid phase is highly conductive. Despite these studies, the heat transfer characteristics of natural convection in coarse-grained porous media still leave many open questions. In particular, the effect of the conductivity of spheres, packing structure of the porous matrix, and size of the spheres have not been systematically characterized and understood in terms of Nusselt vs. Rayleigh (Nu-Ra) relations for different flow regimes.

To explain the behavior of Nu-Ra data of natural convection in porous media, and to obtain a deeper understanding of the underlying physics, it is important to study the fluid flow at the pore scale. Previous experimental studies on natural convection in porous media mainly focused on the overall heat transfer, and data

on the structure and dynamics of the flow and temperature fields are still lacking. Over the past decades, several researchers have attempted to visualize convection in porous media. The earliest studies were either qualitative flow visualizations [69,82,83] or single-point intrusive temperature measurements [71]. Shattuck et al. [94] were the first to measure velocity profiles of natural convection in a packed bed of 3.2 mm plastic beads heated from below. They were able to measure the vertically-averaged vertical velocity by using Magnetic Resonance Imaging (MRI). The most important drawback of their measurements was the limited spatial and temporal resolution. Since Shattuck et al. velocity measurements of thermal convective flows inside porous media have not improved significantly, and highly resolved velocity fields have not been measured yet.

Optical flow measurement techniques such as Particle Image Velocimetry (PIV) for velocity measurements and Liquid Crystal Thermography (LCT) for temperature measurements cannot be used easily in porous media, because these methods obviously require optical access both for illumination and imaging of tracer particles. A possible approach to overcome this challenge is to match the refractive index of a (transparent) porous medium to that of the liquid. Refractive index matching has been applied in several studies to visualize fluid flow in porous media by minimizing image distortion and providing optical access. Two categories of liquids were considered to match the refractive index of transparent solid materials: (i) aqueous salt solutions [88,89], and (ii) organic fluids [85,90]. Unfortunately, the refractive indices of all frequently-used refractive index matched liquids are strongly temperature dependent. This adversely affects the refractive index matching and causes optical distortions in non-isothermal flows. As a consequence, all the refractive index matching works so far have been done only in isothermal flows and, to the knowledge of the authors, refractive index matched liquids have never been used to visualize thermal convection in porous media.

In this study, water was chosen as the liquid since its refractive index has the lowest sensitivity to temperature variations among all other refractive index matched liquids. Polyacrylamide hydrogel spheres were used to match the refractive index of water. A few recent studies have reported on the use of hydrogel and water for refractive index matching. Byron and Variano [95] and Weitzman et al. [96] fabricated solid objects from hydrogel material and explored the use of hydrogel for refractive index matching to study flow-solid interaction. Klein et al. [97] used hydrogel spherical particles in water to study the dynamics of inertial particles in a turbulent flow.

The main objective of the present study is to provide a better understanding of natural convection flow and heat transfer in wall-bounded coarse-grained porous media heated from below. To achieve this objective we carried out detailed heat

transfer experiments for different sphere diameters, sphere thermal properties, and packing types. By matching the refractive index of the fluid and the spheres, optical measurement techniques like PIV and LCT could be applied to determine spatially and temporally resolved velocity and temperature fields in the cell.

## 2.2 Experimental Setup

### 2.2.1 Test Cell

The experiments were performed in two cubical convection cells with internal dimensions 77×77×77 $mm^3$ and 155×155×155 $mm^3$, see Fig. 2.1a. Each cell has copper top and bottom plates that serve as isothermal cold and hot walls, respectively. The four side walls are made of glass. The bottom plate is heated with electrical heating foils (Minco HK5955). The top plate is kept at a (relatively) low temperature by water from a thermostatic bath (Julabo FP51) that flows through channels, see Fig. 2.1a. In the heat transfer measurements, the side walls and the bottom plate are covered with polystyrene insulation panels of 30 mm thickness to minimize the heat losses to the surroundings. Pt100 resistance thermometers (Omega Engineering RTD-3-1PT100K2528-1M-T-1/10) with an inaccuracy of ±0.03 °C are used to measure the temperatures of the top and bottom plates. The temperature readings are collected by a data acquisition module (Omega Engineering PT-104A) and displayed in the logging software. Copper plates with very high thermal conductivity were used as the bottom and top plates to enhance the temperature uniformity of the plates. This was examined by measuring the temperature at different parts of the hot and cold plates. The maximum temperature non-uniformity observed was ~ 0.04 °C for the hot plate and ~ 0.01 °C for the cold plate. The average of two temperature sensors in each plate was used as the plate temperature. The temperature non-uniformity was considered in the calculation of the uncertainty of the temperature measurements.

### 2.2.2 Heat Transfer measurements

In the heat transfer measurements, the temperature difference between the bottom and top plates, $\Delta T$, was varied between 2 °C and 20 °C in a number of steps. In each step, the electrical power fed to the heating foils, $P$, and the thermostatic bath temperature were adjusted. The temperatures of the top and bottom plates were then monitored in time until a steady state was reached. The temperature difference between the plates, $\Delta T$, and the electrical power, $P$, were then measured. The temperatures of the hot and cold plates were always kept symmetrically around the ambient temperature of 22 °C to guarantee that the average Prandtl number of the working fluid remained constant during the experiment. This

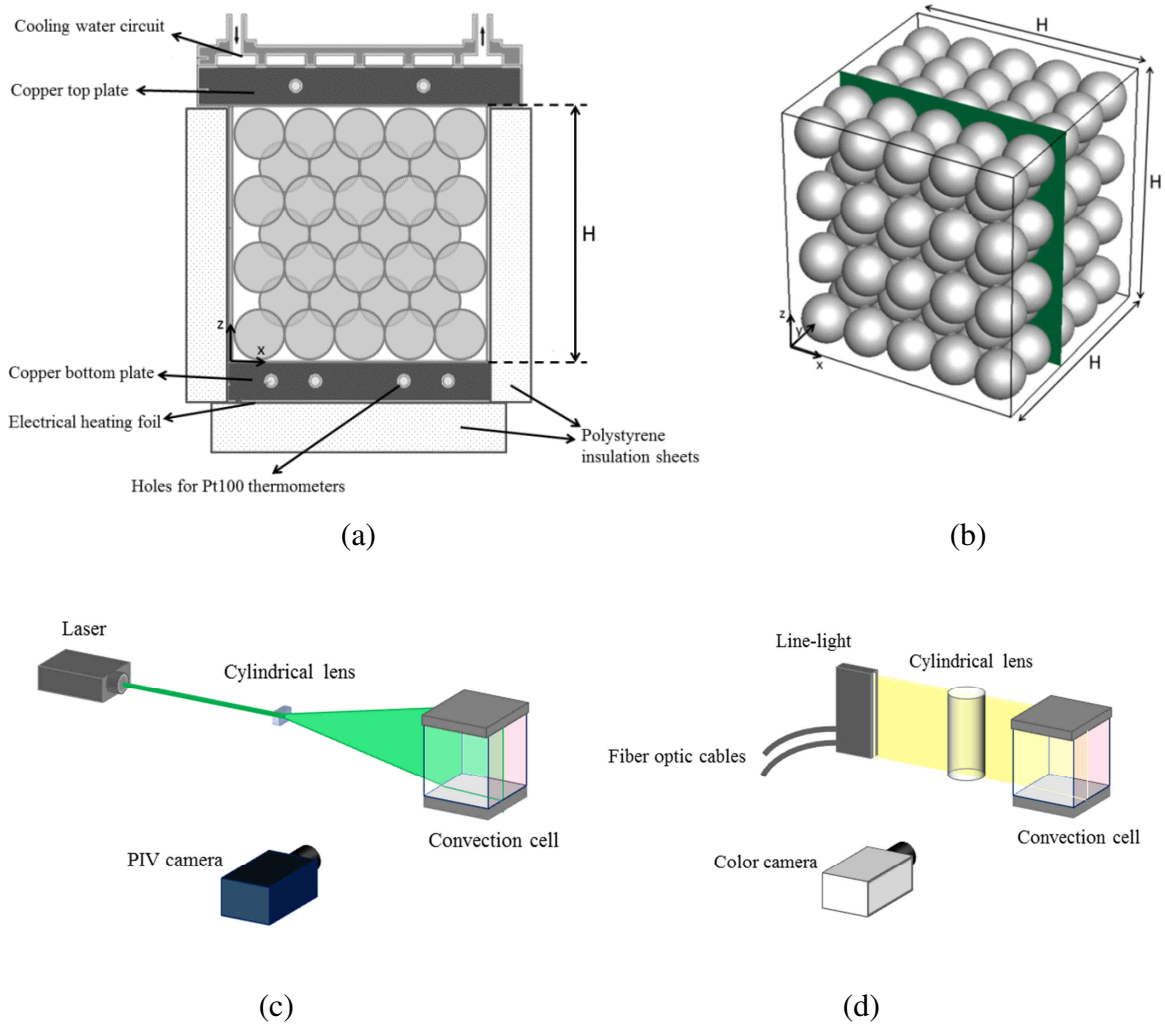


Fig. 2.1 (a) Schematic of the convection cell filled with spheres in BCT packing. (b) Schematic view of BCT packing and the PIV/LCT measurement plane. (c) Schematic of the PIV setup. (d) Schematic of the LCT setup.

procedure also minimizes temperature differences between the cell and the ambient, thus minimizing heat losses to the surroundings. Taking into account the estimated heat conduction from the hot to the cold wall through the side walls, and neglecting heat losses to the surroundings since the side walls were well insulated and the average temperature of the cell $(T_{hot}+T_{cold})/2$ was kept equal to the ambient temperature, the overall Nusselt number Nu was computed from

$$\mathrm{Nu} = (P - A_w k_w \Delta T/H) / (A_f k_f \Delta T/H) = P H/ (A_f k_f \Delta T) - A_w k_w/(A_f k_f), \quad (2.1)$$

where $H$ is the distance between the top and bottom plates, and $k_f$ and $k_w$ are the thermal conductivities of the fluid and the side-wall material, respectively. $A_f$ is the inner cross-sectional area of the cell and is equal to $A_f = H^2$, and $A_w$ is the side-wall

cross-sectional area and is equal to $A_w = 4w(H+w)$, where $w$ is the side-wall thickness. The temperature difference $\Delta T$ was used to compute the Rayleigh number as in

$$\mathrm{Ra} = \beta \Delta T\, g\, H^3/(\alpha \nu), \tag{2.2}$$

where $g$ is the gravitational acceleration, $\beta$ is the thermal expansion coefficient, $\alpha$ is the thermal diffusion coefficient, and $\nu$ is the kinematic viscosity of the fluid. Note that the Nusselt number and the Rayleigh number defined in Eqs. (2.1) and (2.2) are based on fluid properties and not on properties of the porous medium. This is motivated by the observation that (for sufficiently high Ra-numbers) different heat transfer data sets group much better in Nu-number versus Ra-number graphs when fluid properties are used instead of porous medium properties. This was also observed by Keene and Goldstein [70].

The Ra-number was varied over the range $1.5\times10^7 \leq \mathrm{Ra} \leq 1.5\times10^9$. The high Ra-numbers were achieved by either using methanol as a working fluid in the small cell (in heat transfer measurements), or by using water in the large cell (in PIV and LCT measurements). Water and methanol have similar Prandtl numbers; i.e. Pr = 6.75 for water and Pr = 7.63 for methanol (both at 22 °C). The maximum uncertainty in the heat transfer experiments occurs at the lowest temperature difference and is 2.8% for the Ra-number and 2.9% for the Nu-number.

In the heat transfer measurements, two different sphere diameters (10.5 mm and 15.3 mm) and four different sphere materials (brass, steel, glass, and polypropylene) were used. The spheres were arranged in a body-centered tetragonal (BCT) packing (see Fig. 2.1b), but simple cubic packing (SCP) and "random packings" were also considered.

### 2.2.3 PIV and LCT measurements

As mentioned above, refractive index matching is required to perform optical measurements (PIV and LCT) in porous media. To achieve this, water and hydrogel spheres were chosen as the working fluid and solid material, respectively. Hydrogel spheres are made of superabsorbent polymers and absorb more than 200 times their initial volume in water, resulting in a refractive index very close to that of the surrounding water (~0.1% difference).

Hydrogel spheres were arranged in BCT packing for PIV and LCT measurements. The measurement plane was located at y/H = 0.4 where y is the distance from the front wall, see Fig. 2.1b.

Particle Image Velocimetry (PIV) measurements were performed to obtain highly resolved 2D velocity fields. Fig. 2.1c shows the main components of the PIV

setup. A diode-pumped solid-state laser (Pegasus) with a power of 0.8 W and a wavelength of 532 nm was used to create a light sheet with a thickness of approximately 2 mm. The flow was seeded with Polyamide tracer particles (Dantec Dynamics) with a mean diameter of 5 μm. A PIV camera (LaVision Imager Intense) with a resolution of 1376×1040 pixels was used to record images. The camera is equipped with a 28 mm Nikon lens with an f-number of 2.8. The magnification factor of the recordings is $M$ = 0.083 for the small cell and $M$ = 0.042 for the large cell. The resulting spatial resolution of images is around 80 μm/pixel for the small cell and 160 μm/pixel for the large cell. Raw PIV images were processed by commercial LaVision software (Davis 7.2). Velocity vectors were calculated based on a multi-pass cross-correlation with final interrogation windows of 16×16 pixels and an overlap of 50% which corresponds to a vector resolution of 0.64 mm in the small cell, and 1.28 mm in the large cell. The laser was triggered with a pulse separation time of 60 ms, which leads to particle image displacement of about 6 pixels in the regions with the highest velocity.

Liquid Crystal Thermography (LCT) was used to visualize and obtain highly resolved temperature fields. The main components of the LCT setup are shown in Fig. 2.1d Micro-encapsulated liquid crystal tracers (Hallcrest R25C60W) with a mean diameter of 10-15 μm were added to the working fluid with a concentration of 0.01 vol.%. The light source consisted of a LED lamp (Waldmann MCXFLS3) and a halogen lamp (Schott-Fostec, LLC). Since LED light is stronger in the range of lower wavelengths of the visible light spectrum (blue and green), whereas halogen light mostly contains higher wavelengths (yellow and red), the combination of the two lighting types gave a more uniform distribution of all colors in the visible spectrum. The light from these sources was transferred through fiber optic cables to a line-light (Schott-Fostec A08912). A cylindrical lens was then used to convert the diverging sheet coming from the line-light into a light sheet with a thickness of 2 mm inside the convection cell. A PCO Sensicam color camera with a resolution of 1280×1024 was used to record images of the liquid crystal particles.

In the LCT experiments, the reflected light was recorded in a direction normal to the light sheet, i.e. the viewing angle is 90° (see Fig. 2.1d). For this viewing angle, both the red start temperature and the bandwidth were reduced to about ~ 18.4 °C and ~ 11 °C, respectively. Therefore, the effective temperature range of the liquid crystals in this lightsheet configuration (with 90° viewing angle) was found to be from 18.4 °C to 29.4 °C. This $\Delta T$ = 11 °C temperature difference leads to Ra = $8.5\times10^7$ in the small cell and Ra = $7.3\times10^8$ in the large cell. To determine quantitative temperature distributions from the recorded color images, a temperature-hue calibration was performed. Each calibration run involves imposing a constant temperature to both top and bottom plates, using a stirrer in

the cell to ensure a uniform temperature, and at the same time monitoring the temperature of a Pt100 thermometer inserted into the cell. After achieving the steady state, the temperature was acquired by the thermometer and color images were taken to obtain the hue value. This was achieved by converting the recorded RGB images to HSV color space using the algorithm proposed by Smith [98] and extracting the hue component to generate a temperature-hue calibration curve. A sixth-order polynomial was fitted to the resulting calibration curve which then was used to obtain quantitative temperature fields. The uncertainty of the temperatures measured by LCT method was calculated to be around ± 0.5 °C.

## 2.3 Results and Discussion

### 2.3.1 Results of the Heat Transfer Measurements

Fig. 2.2 shows the Nu-Ra data-points for the BCT packing of glass spheres with 15.3 mm diameter measured in the small cell. As discussed in the previous section, the Nu-number and Ra-number are determined using fluid properties. The Nu-Ra data-points for pure Rayleigh-Bénard (RB) convection as determined in the same experimental setup, but in absence of the porous medium, are also shown in Fig. 2.2. In this figure, the closed and open markers represent results for experiments with water and methanol, respectively. The power-law that best fits the RB data-points over the range of Ra-numbers between $1.5 \times 10^7$ and $1.5 \times 10^9$ was determined as $Nu = 0.119\ Ra^{0.306}$, which is in good agreement with the RB theoretical models and experimental data [99]. This relation is shown as a solid line in Fig. 2.2, and it serves as a reference in the remainder of the chapter.

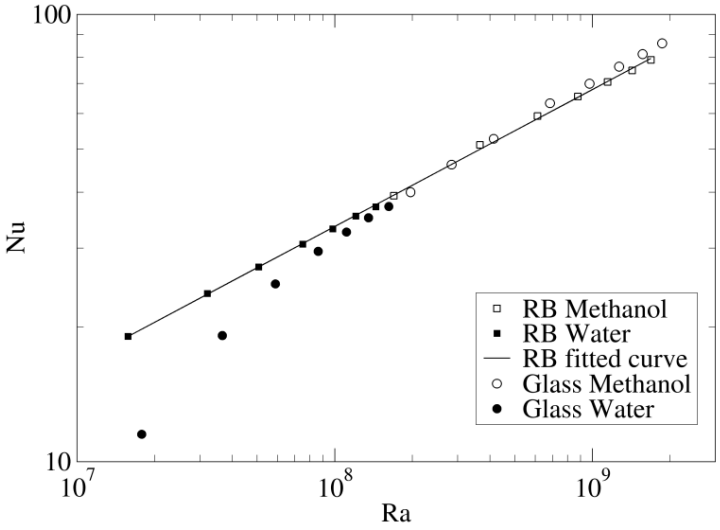


Fig. 2.2. Heat transfer data for BCT packing of $d$ = 15.3 mm glass spheres, compared to that for pure Rayleigh-Bénard convection.

Fig. 2.2 indicates that the presence of the glass spheres reduces the Nu-number (relative to the pure RB convection) at lower Ra-numbers. However, at high Ra-numbers, the Nu-Ra data-points line up with and slightly exceed those for pure RB. This is in accordance with what Keene and Goldstein [70] observed in their experimental results.

#### *2.3.1.1 Effect of Packing Type and Size of the Spheres*

The effect of the packing type on the heat transfer was investigated by using three different packings of glass spheres with the same size in water and in methanol. The different packings have different porosities. For the studied small cubical cell, the BCT packing has a porosity $\phi = 0.420$; the simple cubic packing has a porosity $\phi = 0.486$; and the random packing has a porosity of $\phi = 0.454$. The results shown in Fig. 2.3 demonstrate that at lower Ra-numbers, the heat transfer is the lowest for the BCT packing, which is less permeable to the fluid flow as compared to the other two packing types. However, at higher Ra-numbers, the Nu-Ra curves for all three packings converge, and heat transfer across the porous media becomes independent of the packing of the spheres.

Furthermore, the effect of the size of the spheres on the heat transfer has been studied by using random packings of glass spheres with diameters d = 15.3 mm and d = 10.5 mm and almost equal porosities of $\phi \sim 0.46$. Fig. 2.4 shows that the sphere size has a substantial effect on the heat transfer at lower Ra-numbers, with a factor ~1.5 higher heat transfer for the larger spheres at Ra ~ $1.5\times10^7$. However, at high Ra-numbers, both curves converge, differing by less than 3% for Ra > $6\times10^8$, and both lining up with the RB curve. This implies that the heat transfer is independent of the size of spheres if the Ra-number is sufficiently high.

The results of heat transfer measurements in the packed beds of spheres with different packing structure and sphere size showed that two heat transfer regimes can be distinguished. One is the reduced heat transfer regime at lower Ra-numbers, where the Nu-number values are lower than that of pure RB convection. In this regime, the Nu-number depends on the porous media packing and the grain size. The other regime is the *asymptotic regime*, at higher Ra-numbers, where the data from different packings and sphere sizes collapse and line up with the pure RB power-law curve with slightly higher Nu-number values. Therefore, in this regime, the heat transfer through porous media is independent of the permeability or the Darcy number. Fig. 2.4 also shows that the onset of the asymptotic regime is influenced by the size of the spheres in the packing bed. The onset occurs at a higher Ra-number for the smaller spheres (lower Darcy numbers).

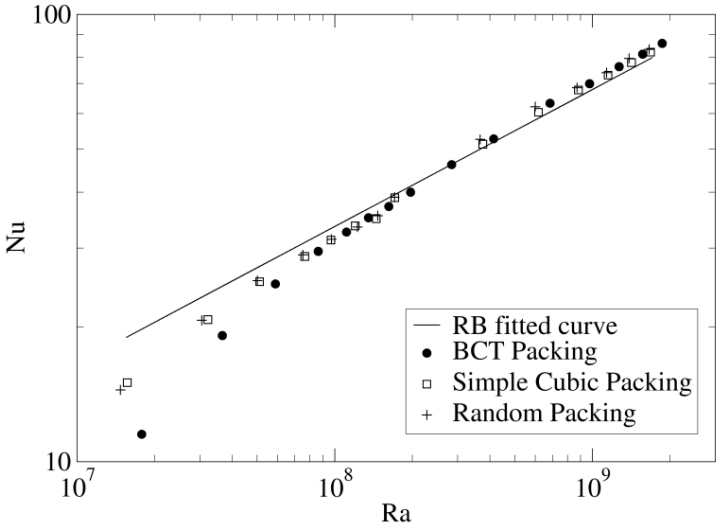


Fig. 2.3. Effect of packing type: heat transfer data for different packing structures of $d$ = 15.3 mm glass spheres, compared to that for pure Rayleigh-Bénard convection.

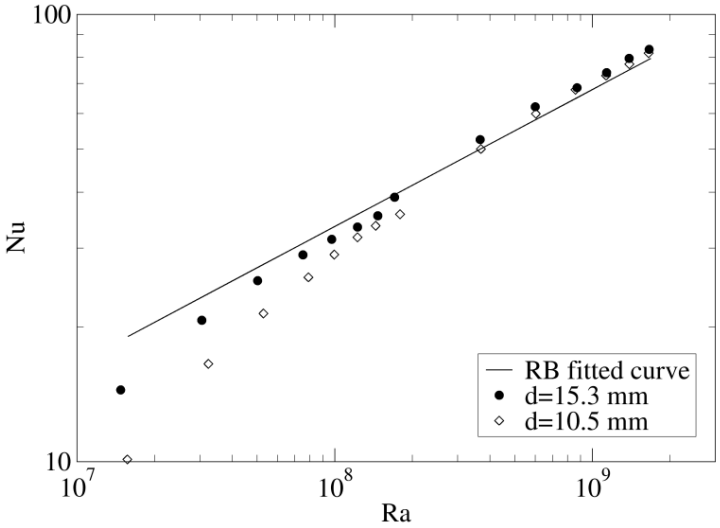


Fig. 2.4. Effect of size of spheres: heat transfer data for random packing of $d$ = 10.5 mm and $d$ = 15.3 mm glass spheres, compared to that for pure Rayleigh-Bénard convection.

#### *2.3.1.2 Effect of Thermal Conductivity of the Spheres*

Experiments were carried out with spheres made of four different materials (brass, steel, glass, polypropylene) to gain insight into the effects of the thermal properties of the spheres on the overall heat transfer. Table 2.1 lists the ratios of solid and fluid thermal conductivities for all combinations of solid and fluid considered in this study. Fig. 2.5 shows the Nu-Ra data-points obtained with 15.3 mm diameter spheres in BCT packing for the four different materials. The results show that for the entire range of Ra-numbers, Nu increases with increasing conductivity ratio. The increased heat transfer can be attributed to the increased conduction through

the porous medium, which can be characterized by effective thermal conductivity of porous media.

The effective thermal conductivity is an important characteristic of a fluid-saturated porous medium. The most widely used correlations for the effective thermal conductivity of packed beds of particles are the correlations by Kunii and Smith [100] and Zehner and Schlunder [101]. These correlations were derived based on one-dimensional heat conduction models in a unit cell. Later, a modification of Zehner-Schlunder model was proposed by Hsu et al. [102]. However, these correlations were developed for the bulk region of the packed bed and are not valid in the vicinity of walls, as discussed by van Antwerpen et al. [103]. In addition, the effective thermal conductivity not only depends on the porosity and thermal conductivities of solid and fluid phases but also on the structural arrangement of the packed bed and the contact points between the solid particles [24]. In the absence of useable correlations for the effective conductivity, in the present work, the conduction heat transfer for exactly the same geometries as used in the experiments for each combination of fluid and sphere material was computed by solving the 3-dimensional conjugate heat conduction using the commercial CFD code ANSYS Fluent. The resulting effective conductivities are listed in Table 2.1.

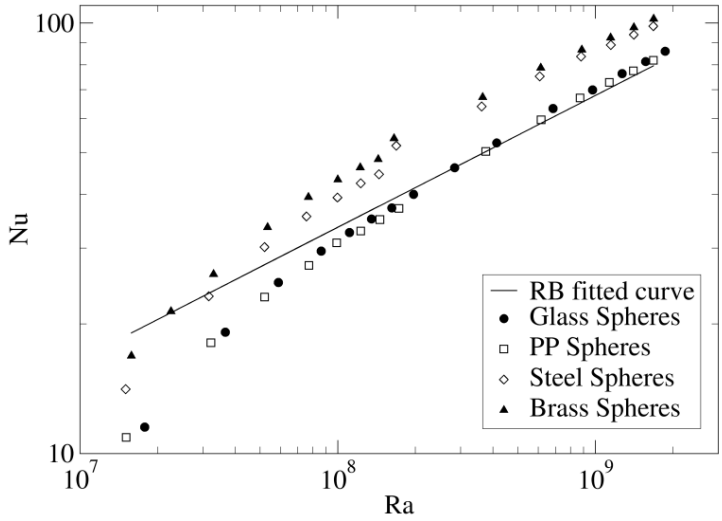


Fig. 2.5. Heat transfer data for BCT packing of $d$ = 15.3 mm spheres with different thermal conductivities, compared to that for pure Rayleigh-Bénard convection.

Using the computationally determined effective thermal conductivity values $k_{eff}$ of the various fluid-solid combinations from Table 2.1, we may compute the overall heat transfer due to combined conduction in the solid and fluid in the absence of convection (as e.g. in zero gravity), indicated here by $Nu_{cond} = k_{eff}/k_f$. The overall measured heat transfer, indicated by Nu, can now be split into contributions from

Table 2.1. Solid to fluid conductivity ratio and the ratio of effective thermal conductivity to fluid conductivity.

| Spheres and fluid materials | $\frac{k_s}{k_f}$ | $\frac{k_{eff}}{k_f}$ |
|---|---|---|
| Brass-Methanol | 618 | 17.3 |
| Brass-Water | 196 | 13.6 |
| Steel-Methanol | 222 | 14.0 |
| Steel-Water | 70.4 | 9.45 |
| Glass-Methanol | 4.19 | 2.30 |
| Glass-Water | 1.33 | 1.22 |
| Polypropylene-Methanol | 1.00 | 1.00 |
| Polypropylene-Water | 0.32 | 0.79 |

conduction and convection, where the latter is obtained by subtracting the conduction term from the measured overall heat transfer, which gives

$$\mathrm{Nu_{conv}} = \mathrm{Nu} - \mathrm{Nu_{cond}} = \mathrm{Nu} - k_{\mathrm{eff}}/k_{\mathrm{f}}. \quad (2.3)$$

The resulting convective Nusselt numbers $\mathrm{N_{conv}}$ are plotted in Fig. 2.6. It shows that at high Ra-numbers, the convective heat transfer data of various materials with different thermal conductivities group well together and line up with the convective pure RB curve which is given by Nu-1. Hence, the converging asymptotic regime is observed also for different conductivities, when the conduction contribution, $k_{\mathrm{eff}}/k_{\mathrm{f}}$, is subtracted. At lower Ra-numbers, the convective heat transfer highly depends on the conductivity of spheres and the lowest values of convective heat transfer are found for the cases with the highest conductivity of the solid spheres (brass and steel). That is mainly due to the fact that heat is primarily transported by conduction through the conductive spheres at lower Ra-numbers, enforcing a stratified temperature distribution in which convective motion of the fluid is suppressed. However, as the Ra-number increases, the convective heat transfer values for highly conductive spheres gradually approach (and in the asymptotic regime reach) those for low conductive spheres. The

convective heat transfer contribution for all experiments with various sphere size, packing types and conductivities are gathered in Fig. 2.7. This figure clearly shows the converging power-law asymptotic regime for Ra > $6\times10^8$ (for 15.3 mm spheres) and the reduced heat transfer regime at lower Ra-numbers. The existence of the two heat transfer regimes can be explained by comparing the thermal length scale and the porous length scale. At low Ra-numbers, in the reduced heat transfer regime, the thickness $\delta$ of the thermal boundary layers is not sufficiently small compared to the size of the spheres *d*. Consequently, the flow cannot penetrate into the pores easily and experiences a resistance due to the presence of the spheres.

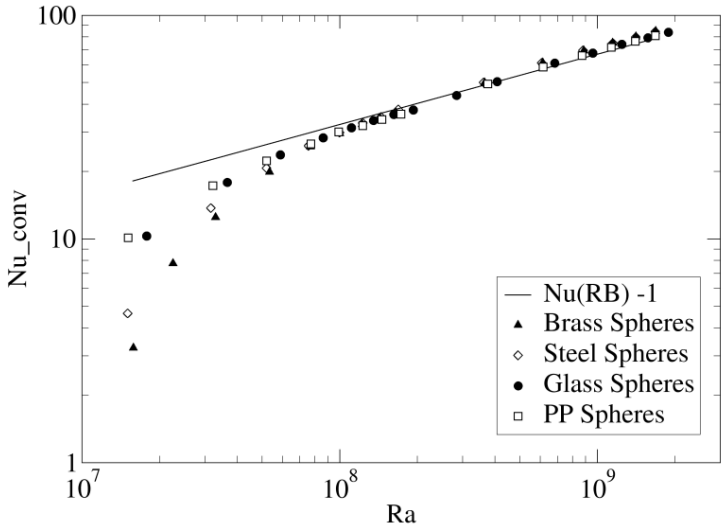


Fig. 2.6. Convective heat transfer for BCT packing of *d* = 15.3 spheres with different thermal conductivities, compared to that for pure Rayleigh-Bénard convection.

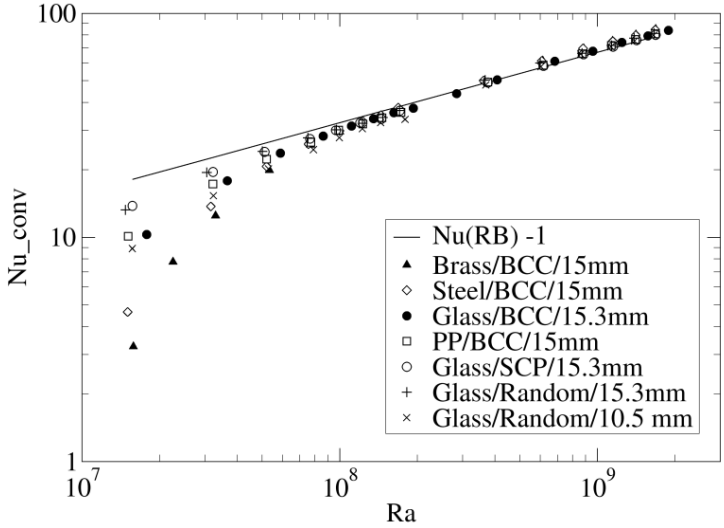


Fig. 2.7. Convective heat transfer for different sphere conductivities, packing types, and sphere sizes, compared to that for pure Rayleigh-Bénard convection.

This leads to a significant reduction of the heat transfer. For highly conductive spheres, the convective heat transfer is even more suppressed due to the dominance of conduction at low Ra-numbers enforcing a stratified temperature distribution. However, at high Ra-numbers, in the asymptotic regime, the thermal boundary layers are sufficiently thin, such that the flow can penetrate into the pores and carry the heat efficiently through the porous medium regardless of packing structure, size of spheres, and their conductivity. Therefore, the convective part of heat transfer data lines up with the RB curve, and with the addition of conduction contribution, the overall heat transfer becomes even higher depending on the sphere conductivity. For the smaller spheres, the thermal boundary layer thickness $\delta$ has to become even smaller in order for the flow to penetrate into the pores. Hence the onset of the asymptotic regime occurs at higher Ra-numbers. The thermal boundary layer thickness $\delta$ is estimated by using the relation $\delta = H/(2\mathrm{Nu})$ and compared to the sphere sizes. The comparison of scales for all the data sets suggests that the asymptotic regime is reached when $\delta/d$ becomes less than approximately 0.045. To confirm the above-mentioned explanation, the velocity and temperature fields of the two heat transfer regimes are compared in the next section.

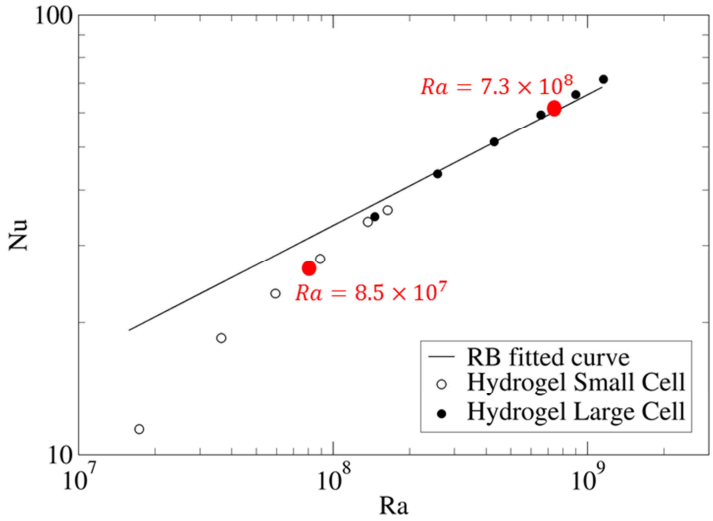


Fig. 2.8. Convective heat transfer for Hydrogel spheres in water. PIV/LCT measurement points are shown in red.

### 2.3.2 Results of the PIV and LCT measurements

To better understand the physics of natural convection flow in coarse-grained porous media and enhance knowledge of the mechanisms influencing the heat transfer in the two regimes, velocity and temperature fields were measured at two different Ra-numbers, i.e. Ra = $8.5\times10^7$ which is in the reduced heat transfer regime and Ra = $7.3\times10^8$ which is in the asymptotic regime. Fig. 2.8 shows the

Nu-Ra data-points for BCT packing of hydrogel spheres in water, and the two data-points where the velocity and temperature measurements were carried out.

Water and hydrogel form a fully transparent refractive index matched liquid-solid pair that enabled the use of the optical measurement techniques, PIV and LCT, to study natural convection velocity and temperature fields in porous media for the first time. Fig. 2.9 shows the mean velocity fields for the reduced heat transfer regime at Ra = $8.5\times10^7$ (left) and the asymptotic regime at Ra = $7.3\times10^8$ (right). The mean velocity fields were determined from 10000 double snapshots that were acquired at a frequency of 1 Hz. The velocity vectors are shown in black and are overlaid on a color map which describes the local velocity magnitude. The velocity fields clearly show that at Ra = $8.5\times10^7$, in the reduced heat transfer regime, the flow velocities in the central region inside the pores are very small, whereas flow with high velocity is observed only in a thin layer near the periphery of the cell. However, at Ra = $7.3\times10^8$, in the asymptotic regime, high velocities occur inside the pores as well as near the walls. To make a better and more quantitative comparison of the local velocity distribution at the two different Ra-numbers, vertical velocity component ($v_z$) profiles along three different horizontal lines $z/H = 0.37$, $z/H = 0.63$, and $z/H = 0.90$ and also along three different vertical lines $x/H = 0.3$, $x/H = 0.5$, and $x/H = 0.7$ are shown in Fig. 2.10. The increased penetrating velocities in the pores at the higher Ra-number is clearly observed at various vertical and horizontal positions, whereas near-wall velocities remained almost unchanged. The overall mean velocity fields and the local mean velocity profiles obtained by PIV experiments clearly supports the explanation that the ratio between the thermal length scales and pore length scales determines the flow structure and heat transfer in porous media. At low Ra-numbers, $\delta/d$ is not sufficiently small, therefore the flow cannot easily penetrate into the pores and it prefers to move along the walls where more space is available due to higher local porosity. However, in the asymptotic regime, $\delta/d$ becomes sufficiently small such that the flow can penetrate into the pores with high velocities and carry the heat to the opposite plate without experiencing resistance from the presence of the spheres, and the convection heat transfer can reach values as high as those in RB convection.

Fig. 2.11 shows the qualitative and quantitative steady state temperature distributions obtained from LCT measurements at Ra = $8.5\times10^7$ (left) and Ra = $7.3\times10^8$ (right). At both Ra-numbers, the temperatures of the cooling and heating plates were set to 18.4 °C and 29.4 °C, respectively. In the qualitative images, the red color corresponds to the lowest temperature and the blue color represents the highest temperature. The obtained temperature fields show that at both studied Ra-

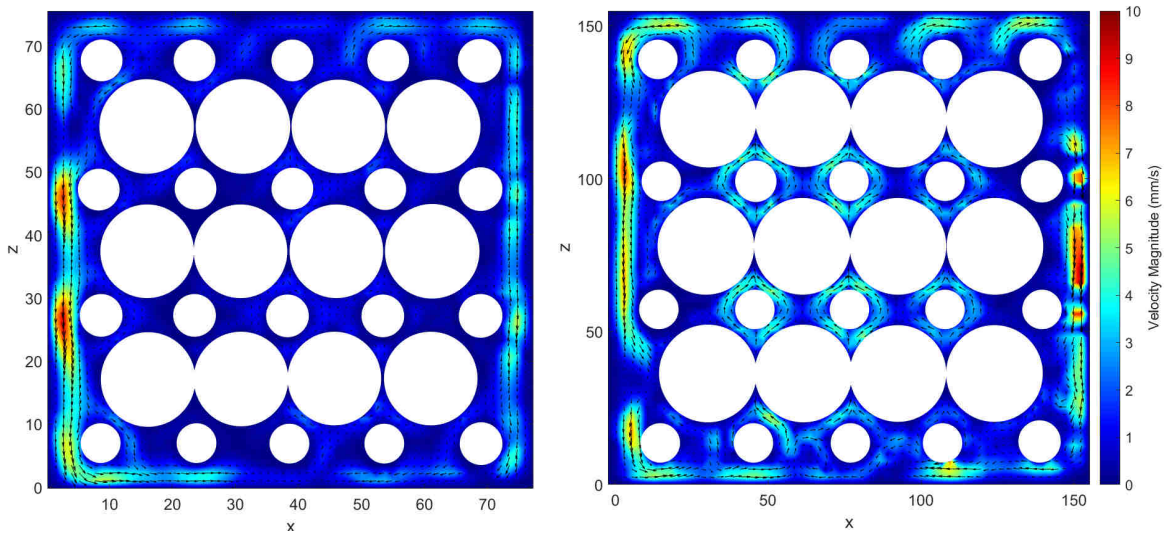


(a) (b)

Fig. 2.9. Mean velocity fields in a vertical plane at (a) Ra = $8.5\times10^7$ and (b) Ra = $7.3\times10^8$.

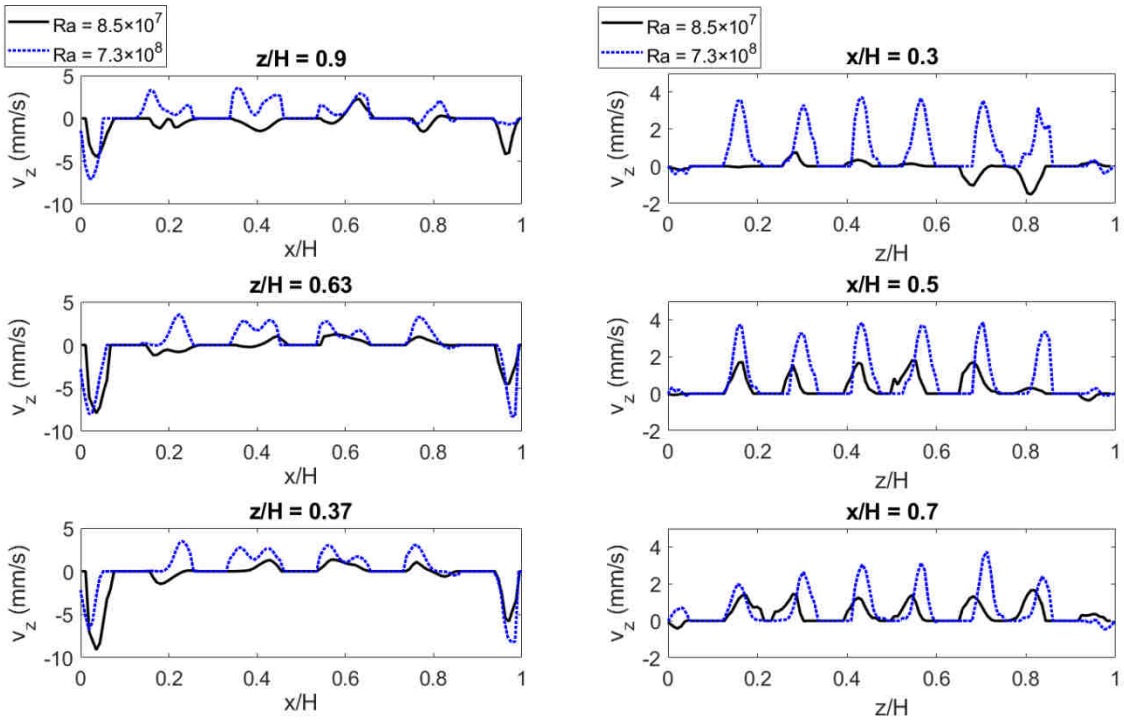


(a) (b)

Fig. 2.10. Profiles of the mean vertical velocity component for Ra = $8.5\times10^7$ (black line) and Ra = $7.3\times10^8$ (blue dotted line) along (a) three different horizontal lines ($z/H$ = 0.37, $z/H$ = 0.63, and $z/H$ = 0.90) and (b) three different vertical lines ($x/H$ = 0.3, $x/H$ = 0.5, and $x/H$ = 0.7)

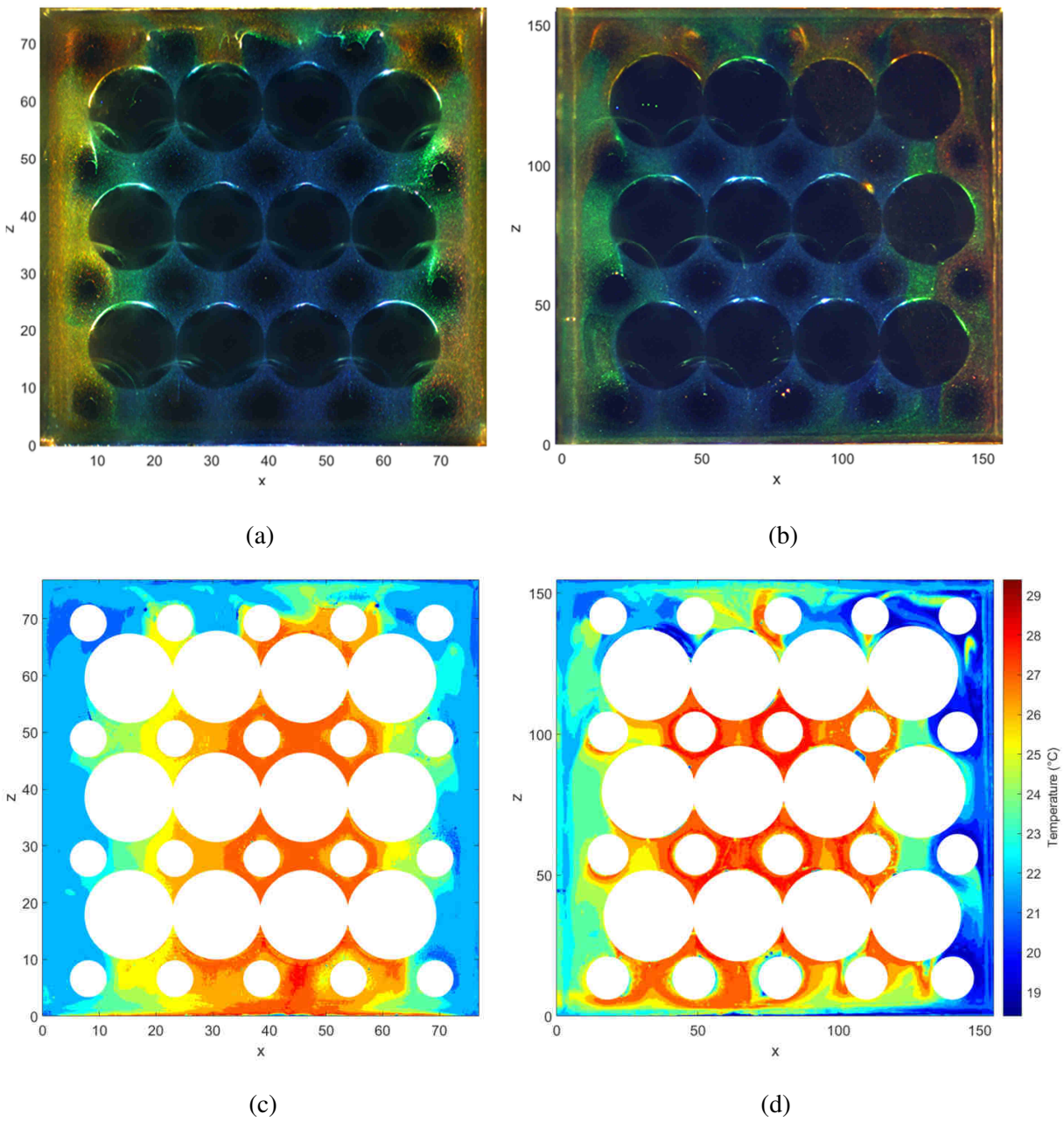


Fig. 2.11. Qualitative instantaneous temperature distribution at (a) Ra = $8.5\times10^7$ and (b) Ra = $7.3\times10^8$. In these images, the red color corresponds to the lowest temperature and the blue color represents the highest temperature. Quantitative mean temperature distribution at (c) Ra = $8.5\times10^7$ and (d) Ra = $7.3\times10^8$. In these measurements, the temperatures of the cooling and heating plates were set to 18.4 °C and 29.4 °C, respectively.

numbers, warmer fluid moves upward in the central region (hot core) and colder fluid moves downward near the side walls. These vertical columnar structures spanning the height of the cell were also observed by Hewitt et al. [104] in their 2D direct numerical simulation using Darcy's law, and were called "mega

plumes". Despite the similarities in flow structure, some differences can be also observed. The most important one is that at high Ra-number, relatively cold fluid can be observed just adjacent to the heating plate, and also hot fluid very close to the cooling plate. This means that hot and cold fluid can penetrate very deeply up to the opposite solid boundaries and consequently enhance the heat transfer. That is mainly due to the much higher penetrating velocities through the porous medium which enhance the strength of thermal advection compared to thermal diffusion. However, at low Ra-number the heat diffuses to a greater extent from the hot central region to the cold regions along the side walls, leading to a narrower temperature range in the cell.

Overall, the flow and temperature visualization results confirm that the ratio between the thermal boundary layer thickness and the sphere size determines the flow structure and subsequently governs the corresponding heat transfer to be either in the reduced heat transfer regime or in the asymptotic regime. Therefore, the comparison between thermal length scales and porous length scales plays a central role in natural convection flow in porous media.

## 2.4 Conclusions

An experimental study of bottom-heated natural convection in coarse-grained porous media, where the porous length scale is not small compared to the flow and thermal length scales, was carried out. Nusselt numbers were measured for various sphere conductivities, spheres sizes, and sphere packings at Rayleigh numbers between $10^7$ and $10^9$. Particle image velocimetry and liquid crystal thermography were used to determine planar velocity and temperature fields in the natural convection cell filled with porous media by using water and hydrogel as refractive index matched pairs.

Nusselt number measurements showed two heat transfer regimes: (i) reduced heat transfer regime at lower Rayleigh numbers, and (ii) asymptotic regime at higher Rayleigh numbers. The Nusselt numbers in the asymptotic regime are independent of packing type and sphere size but clearly depend on the conductivity ratio of the fluid and porous medium. However, the convective contribution of heat transfer converges and lines up with the curve for pure Rayleigh-Bénard convection, for all sphere conductivities, sizes, and packings.

Visualization of the velocity and temperature fields of the two heat transfer regimes showed that in the reduced heat transfer regime, the flow hardly penetrates into the pores, and it is mostly confined to a (thin) region along the periphery of the cell. However, in the asymptotic regime, since the thermal boundary layers become sufficiently thin, the flow penetrates considerably into the porous layer leading to much higher velocity magnitudes in the core region, a deeper penetration of hot and cold fluid up to the opposite solid boundaries, and

consequently higher heat transfer across the porous medium. The obtained results confirm that the comparison between thermal length scales and porous length scales determine the flow structure and the corresponding heat transfer in natural convection in porous media.

# Chapter 3

## An Experimental Study of Flow and Heat Transfer in a Differentially Side-heated Cavity Filled with Coarse Porous Media*

Flow and heat transfer in a differentially side heated cubic cavity filled with relatively large solid spheres forming a coarse porous medium has been studied experimentally. Nusselt numbers were measured for Rayleigh numbers between $1.9\times10^7$ and $1.7\times10^9$, solid-to-fluid conductivity ratios between 0.32 and 618, and for different sphere sizes ($d/H$ = 0.065, 0.14, 0.20), and packing geometries. The heat transfer results indicate that the presence of a porous medium in the cavity decreases the heat transfer compared to the pure-fluid cavity unless the solid spheres are highly conductive. We present a new Nusselt number correlation for coarse porous media based on porous medium dimensionless numbers. Particle image velocimetry and liquid crystal thermography measurements were performed in a refractive index-matched porous medium to obtain pore-scale velocity and temperature fields. The results show that the layers of spheres adjacent to the hot/cold walls play the most prominent role in the heat transfer reduction by hindering the formation of high-velocity boundary layers along the hot/cold walls, causing a portion of the boundary layer fluid to divert away from these walls, thus changing the stratified temperature distribution to a tilted one which leads to a lower overall heat transfer.

* This chapter has been published in the *International Journal of Heat and Mass Transfer*, 143, 118591 (2019).

## 3.1 Introduction

Natural convection in enclosures differentially heated from the sides and containing porous media or solid obstacles has attracted a great deal of attention due to its fundamental nature and the broad range of applications in, for example, iron and steel making [105], food processing [75], electronics cooling [73], and indoor air conditioning [106].

Most theoretical and computational studies in the field of natural convection in differentially side heated cavities filled with porous media have been based on Darcy's law and its extensions to include inertia and viscous diffusion effects (Forchheimer and Brinkman modifications), using so-called volume averaging over representative elementary volumes (REVs) [58,65,66,107]. This is a suitable approach when the pore length scale is much smaller than the macroscopic flow length scales. Lauriat and Prasad [66] numerically solved the Darcy-Brinkman-Forchheimer equations for a differentially heated cavity and reported that the heat transfer rate always increases with the fluid Rayleigh number, Ra, the Darcy number, Da, and the effective thermal conductivity of the porous medium, $k_{\text{eff}}$. They concluded that a porous medium can transport more heat than a pure fluid if the porous matrix is highly permeable and the thermal conductivity of solid particles is higher than that of the fluid.

There are only a few experimental studies on natural convection in differentially side heated cavities filled with porous media and these are limited to heat transfer measurements to verify the mentioned theoretical and computational models [72,108].

Other researchers have studied natural convection in 2D differentially side heated enclosures containing disconnected solid objects [73,76,77,81,109]. They considered solid and fluid constituents separately and solved the Navier-Stokes equations to obtain detailed information on the interaction between the flow and temperature fields with the discrete solid objects. Merrikh and Lage [76] numerically studied natural convection in a differentially heated square enclosure containing several disconnected and conducting solid blocks for Rayleigh numbers between $10^5$ and $10^8$ and solid-to-fluid conductivity ratios between 0.1 and 100. They found that the flow tends to migrate away from the vertical hot/cold walls and penetrates into the interior channels as the number of blocks increases (and the size of the blocks decreases). They derived an analytical expression for the minimum number of blocks necessary for the flow to divert from the hot/cold walls. Raji et al. [81] carried out a similar numerical study for Rayleigh numbers $10^3 \leq \text{Ra} \leq 10^8$, solid-to-fluid conductivity ratios $10^{-3} \leq k_s/k_f \leq 10^3$, and a varying number of solid blocks. They observed that by increasing the number of blocks the heat transfer and flow intensity are significantly reduced, especially at low and

moderate Rayleigh numbers ($Ra \leq 10^5$). They also reported that the blocks with lower conductivity enhance the convection heat transfer.

With the above literature focusing on either Darcy-type modeling of convection and heat transfer in fine-grained porous media with an REV approach, or on convection around disconnected coarse-grained solid objects, in many applications natural convection occurs in porous media consisting of relatively large solid objects which are in contact with each other. Examples include stacks of agricultural products for drying or in cold storages [74] and relatively large coke particles in the hearth of blast furnaces [110]. In the chain of steel production, the blast furnace converts iron ore into hot liquid iron. The furnace hearth has a coarse-grained porous carbon structure with a typical grain size up to 100 mm. With the hot metal flowing in from the top and the walls of the hearth being cooled, the flow of liquid metal in the hearth is a natural convection flow in a coarse-grained porous medium. This flow can cause erosion of refractory walls due to the local wall heat transfer non-uniformities (hot spots). This has a severe impact on the lifetime of the blast furnaces. For such coarse-grained porous media, the REV approach and the use of (extended) Darcy laws are questionable. Therefore, Laguerre et al. [80] compared direct CFD and volume averaged Darcy-Brinkman-Forchheimer to experiments for natural convection in a differentially side heated enclosure filled with a 6×6×5 cubic arrangement of spheres at $Ra = 2.3\times10^8$. Both modeling approaches were found to lead to good agreement with fluid and solid temperatures measured at various locations using thermocouples. Velocities in the pores between the spheres, however, could not be measured to validate the CFD velocity results.

Indeed, visualizing natural convection flow in porous media has always been a challenge. Shattuck et al. [94] measured vertically-averaged vertical velocities in bottom-heated natural convection cells filled with packings of spheres using magnetic resonance imaging (MRI). Laguerre et al. [111] used Particle Image Velocimetry to partially visualize the air flow in a differentially heated rectangular cavity containing cylindrical obstacles which occupied about 15% of the cavity volume. They were not able to visualize the areas behind the obstacles and also at the bottom of the cavity since the laser light sheet was blocked by the obstacles and a support plate at the bottom. Recently, experimental [112] and numerical [1] studies have investigated detailed flow and temperature structures in bottom-heated natural convection cavities filled with relatively large spheres.

In summary, there are still many open questions regarding differentially side-heated natural convection flow and heat transfer in media with a relatively large porous length scale, where (extended) Darcy models are not valid and the relatively large solid particles are in contact with each other. For such systems, the heat transfer, the pore-scale flow structure and the interaction between natural

convection flow and coarse-grained porous media need to be studied in more detail. Detailed experimental data on flow and heat transfer are also required for the development and validation of computational models.

The objective of the present study is to improve the understanding of differentially side heated natural convection flow and heat transfer in coarse porous media in the form of a packed bed of relatively large spheres. We carried out a series of heat transfer measurements in a differentially side heated cubic $H \times H \times H$ cavity to identify the effect of different parameters such as sphere size ($d/H$ = 0.065-0.20), solid-to-fluid conductivity ratio ($k_s/k_f$ = 0.32-618), and packing structure on the overall heat transfer. To obtain detailed information on the pore-scale velocity and temperature distribution throughout the porous medium we performed Particle Image Velocimetry (PIV) and Liquid Crystal Thermography (LCT) measurements in a refractive index matched porous medium (hydrogel spheres in water).

## 3.2 Experimental setup

The experimental setup is very similar to our recent work and is described in [112] in more details. Herein, only the main and novel features of the experimental setup will be described. The same cubical cavity with internal dimensions of 77×77×77 $mm^3$ was used in all the experiments (see Fig. 3.1a). The main difference is that in the present study the cavity is rotated over 90° resulting in a differentially side heated configuration. The left and right walls of the cavity are made of copper plates, serving as isothermal hot wall and cold wall, respectively. The other four walls are made of glass. The left wall was heated with an electrical heating foil attached to the copper plate. Cold water from a thermostatic bath flows through channels inside the right wall to keep it at a lower temperature. The temperatures of the isothermal walls were measured with Pt100 temperature sensors with an inaccuracy of ±0.03 °C. The temperature non-uniformities were measured to be below 0.06 °C for the hot wall and below 0.02 °C for the cold wall.

In the heat transfer measurements, the temperature difference $\Delta T$ between the isothermal walls, and the electrical power of the heating foil, $P$, were used to obtain the Rayleigh and Nusselt numbers. The overall Nusselt number Nu is determined by subtracting the total heat loss $Q_{loss}$ from the electrical power supplied to the heating foil as in

$$\mathrm{Nu} = (P - Q_{loss}) / (A_f k_f \Delta T/H), \tag{3.1}$$

where $H$ is the height of the cubical cavity (77 mm), and $k_f$ is the thermal conductivity of the fluid. $A_f$ is the internal cross-sectional area of the cavity $A_f = H^2$. The electrical power of the heating foil, $P$, was determined by measuring the

electrical current and the voltage difference at the electrical connections near the heating foil. The total heat loss $Q_{loss}$ was determined by performing experiments in the same cavity with the hot plate at the top and the cold plate at the bottom filled with the working fluids (water or methanol). In this configuration, the convective heat transfer is zero and only conduction takes place. The heat that is supplied in addition to the expected fluid conductive heat transfer was taken as the total heat loss.

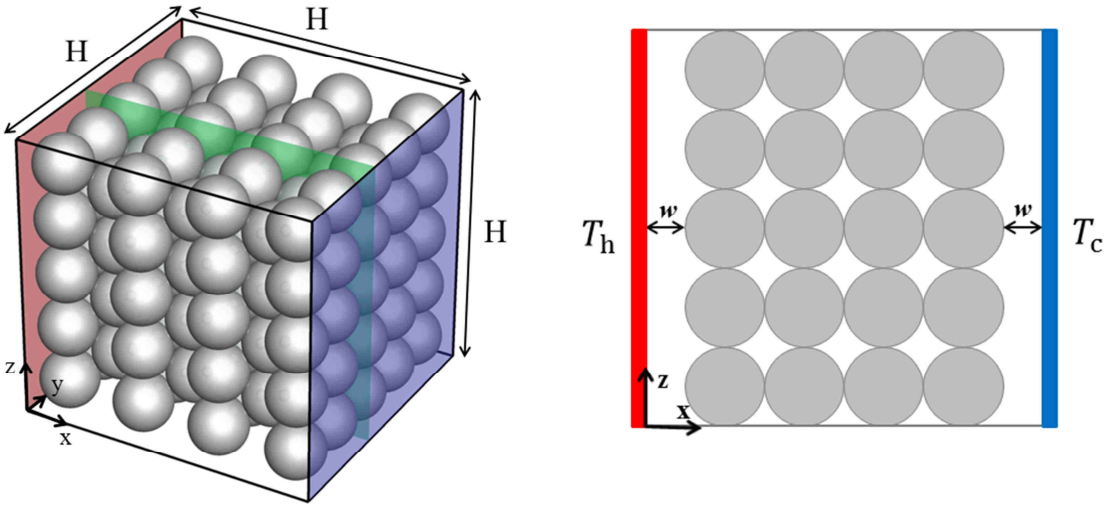


(a) (b)

Fig. 3.1. (a) Sketch of the test cavity filled with spheres with size $d/H = 0.20$ in body-centered tetragonal (BCT) packing, and the location of the light sheet in the PIV/LCT measurements at $y/H = 0.4$. (b) Front view of the 3D printed 4×5×5 simple cubing packing with a gap of $w/H = 0.10$ between the porous medium and the hot/cold walls.

Using the temperature difference between the hot and cold walls, $\Delta T$, the Rayleigh number Ra is determined as

$$\mathrm{Ra} = \beta \Delta T\, g\, H^3/(\alpha \nu), \tag{3.2}$$

where $\beta$ is the thermal expansion coefficient of the fluid, $g$ is the gravitational acceleration, ν is the kinematic viscosity of the fluid and $\alpha$ is its thermal diffusivity. The Nusselt number and the Rayleigh number in Eqs. (3.1) and (3.2) are defined based on the fluid properties rather than the porous medium properties. In this way, the overall heat transfer results can be compared to that of the pure-fluid cavity. In the experiments, the Rayleigh number was varied in the range $1.9\times10^7 \leq \mathrm{Ra} \leq 1.7\times10^9$. The first decade was achieved by varying $\Delta T$ using water

as a working fluid, and the second decade was reached by varying $\Delta T$ using methanol. The two fluids have very similar Prandtl numbers, i.e. $Pr_{water} = 6.75$; $Pr_{methanol} = 7.63$ at 22 °C. The maximum uncertainties in the measured values of the Rayleigh and Nusselt numbers occur at the lowest temperature difference and are equal to 2.8% and 3.0%, respectively.

Four different sphere solid materials (polypropylene, glass, steel, and brass), three different sphere sizes (5.0 mm, 10.5 mm, and 15.3 mm, corresponding to $d/H = 0.065$, 0.14, and 0.20), and three different packing structures were examined in the heat transfer measurements. The spheres were packed in simple cubic (SC), body-centered tetragonal (BCT) (see Fig. 3.1a), and random packing structures. To study the effect of a gap between the hot/cold walls and the porous medium, a 4×5×5 simple cubic packing structure of 15.3 mm polypropylene spheres was build using a 3D printer (Seido Systems Object500 Connex 3), see Fig. 3.1b.

In section 3.3.1.5, a heat transfer scaling based on porous medium dimensionless groups is presented. These porous medium dimensionless numbers are defined as

$$\mathrm{Ra_m} = \mathrm{Ra\ Da}\ k_f/k_{eff}, \tag{3.3}$$

and

$$\mathrm{Nu_m} = \mathrm{Nu}\ k_f/k_{eff}, \tag{3.4}$$

where Da is the Darcy number defined as $\mathrm{Da} = K/H^2$ and $K$ is the permeability of the packed bed of spheres. The value of $K$ is estimated using the Ergun expression [113], $K = \phi^3 d^2/(150(1-\phi)^2)$, where $\phi$ is the porosity of the packed bed and $d$ is the diameter of the spheres. In Eqs. (3.3) and (3.4), $k_{eff}$ is the effective thermal conductivity of the porous medium which is defined as the overall thermal conductivity through the combination of solid and fluid constituents, in the absence of fluid motion. As discussed in [112], the effective thermal conductivities for the geometries and the solid-fluid combinations considered in this study were numerically computed from the 3D heat conduction equation for solid and stagnant fluid. For completeness, the resulting values are shown again in the present chapter in Table 3.1.

To be able to visualize the flow in between the spheres at the core of the porous media, we used water as the liquid and hydrogel spheres - which consist of approximately 99.5 % water, are transparent and have virtually the same refractive index as that of water – for the solid packing. This makes the porous medium optically accessible both for illumination and imaging, thus enabling the use of the optical measurement techniques PIV and LCT. As discussed in our recent work [112], the advantage of using water as working fluid, over frequently-used refractive index matching liquids, is that the refractive index of water has the

lowest sensitivity to temperature variations which makes it an ideal liquid for refractive index matching to study a thermally-driven flow. As a result, the refractive index of the hydrogel spheres matches the refractive index of water at various temperatures with a difference less than 0.1%.

In the PIV and LCT experiments, hydrogel spheres with a diameter of approximately 15.3 mm ($d/H = 0.20$) were arranged in a BCT packing. The measurements were performed in a vertical plane at $y/H = 0.4$ (see Fig. 3.1a).

The same PIV system as described in [112] was used to obtain velocity fields with high spatial resolution. Velocity vectors were calculated from the raw images based on a multi-pass cross-correlation with a final interrogation window size of 16×16 pixels and an overlap of 50% using the LaVision software (Davis 8.4.0). The resulting vector spacing resolution is 0.60 mm.

LCT measurements were performed to obtain planar temperature fields inside the cavity. The LCT experimental setup is described in details in [112]. In the lightsheet configuration with a 90° viewing angle, the measurable temperature range of the liquid crystals was found to be between 20.0 °C and 30.2 °C. Fully making use of this temperature range leads to $\Delta T = 10.2$ °C and hence $\mathrm{Ra} = 9.0\times10^7$.

Temperature-hue calibration as described in [112] was carried out to quantitatively determine temperatures from the LCT color images. The uncertainty of the measured temperatures was estimated to be ± 0.5 °C.

## 3.3 Results and discussion

### 3.3.1 Heat transfer measurements

Fig. 3.2 presents the Nu-Ra data points obtained from heat transfer measurements in the side-heated cavity filled with 15.3 mm ($d/H = 0.20$) polypropylene spheres in BCT packing, along with the results obtained from the same cavity filled with the fluids only. In this figure, the results obtained in water (lower Ra range) and in methanol (higher Ra range) are depicted by closed and open markers, respectively. In the remainder of the chapter, we do not distinguish between measurements in water and methanol and use the same marker for both. The Nu-Ra data for the pure-fluid cavity are fitted well by a power-law

$$\mathrm{Nu} = 0.250\ \mathrm{Ra}^{0.264} \tag{3.5}$$

for $1.9\times10^7 < \mathrm{Ra} < 1.7\times10^9$. The maximum deviation of the experimental data from the power-law curve is 1.2%. This relation agrees well with the findings of studies on differentially side heated cubic cavities in this range of Rayleigh

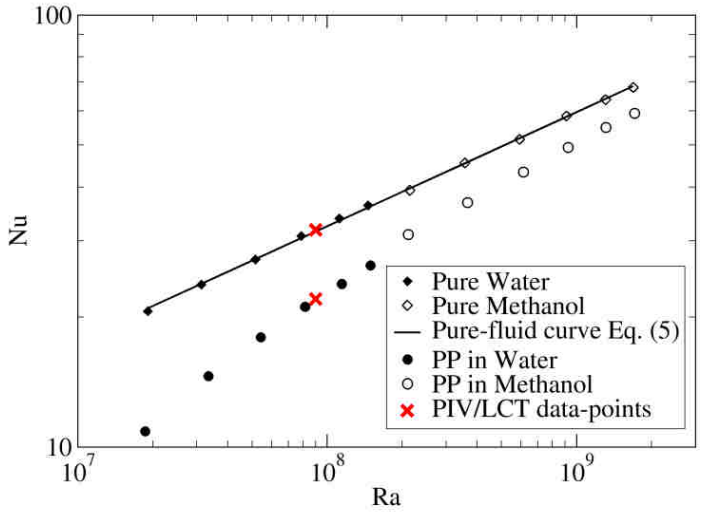


Fig. 3.2. Nu-Ra data for the differentially side-heated cubic cavity filled with a porous medium consisting of 15.3 mm ($d/H = 0.20$) polypropylene (PP) spheres in BCT packing, compared to that for the pure-fluid cavity. The measurements in water and methanol are indicated by closed and open markers, respectively. The solid line denotes the fit to the Nu-Ra data for the pure-fluid cavity, Eq. (3.5). The red crosses pertain to the PIV and LCT measurements described in section 3.3.2.

numbers [33,114]. The power-law curve, Eq. (3.5), is presented as a solid line in Fig. 3.2 and is used as a reference curve in the rest of the chapter. Fig. 3.2 clearly shows that the addition of polypropylene spheres to the cavity reduces the Nusselt number compared to that for the pure-fluid cavity. The reduction continues to exist at Rayleigh numbers as high as $1.7\times10^9$. This is in contrast to what has been found for the same porous medium in a bottom-heated cavity [112], where it was observed that Nusselt values for the same sphere size ($d/H = 0.20$) reach (and even slightly exceed) those of the pure-fluid bottom-heated cavity at $Ra > 6\times10^8$. This implies that the interaction between the natural convection flow and porous media in the side-heated cavity is very different from that in the bottom-heated cavity.

#### *3.3.1.1 Effect of packing type*

To study the influence of the type of packing on Nusselt number in a side-heated cavity, three different packing types were examined: BCT packing, SC packing, and a random packing. Glass spheres with a diameter of 15.3 mm ($d/H = 0.20$) were used to make these packings. In the small cubical cavity considered in this study, a BCT packing resulted in a porosity of $\phi = 42.0\%$, a simple cubic packing in $\phi = 48.6\%$, and a random packing in $\phi = 49.8\%$. Fig. 3.3 shows the Nusselt number as a function of Rayleigh number for the three packings along with the pure-fluid reference curve, Eq. (3.5). It can be observed that the Nusselt numbers are slightly higher for random packing, which has the highest porosity and

permeability, and it is lower for BCT packing, which is the least permeable packing. The results generally imply that Nusselt number in packed beds of spheres is not largely influenced by the type of packing. This is due to the fact that the arrangements of the spheres adjacent to the hot/cold walls are very similar in all the three different packing structures. In both BCT and SC packings, the spheres have the same $5 \times 5$ arrangement at the hot/cold walls, whereas in random packing - due to the large value of $d/H$ and the effects of wall constraints - the spheres are spontaneously arranged in a similar way. While at the lowest Rayleigh number the largest difference in the Nusselt numbers of the three different packings is approximately 14%, the difference is less than 3% at the highest Rayleigh number. This behavior implies that as Rayleigh increases, the Nusselt number becomes more independent of the packing structure.

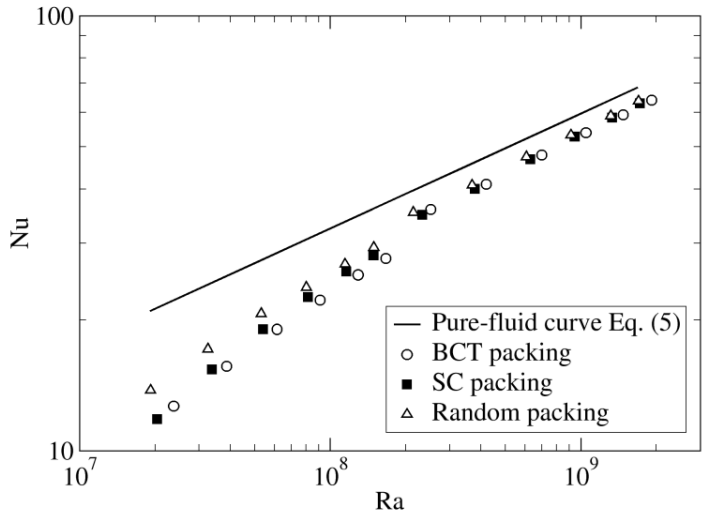


Fig. 3.3. Effect of packing. Nu-Ra data for porous media consisting of 15.3 mm ($d/H = 0.20$) glass spheres with three different packing types. The solid line denotes the fit to the Nu-Ra data for the pure-fluid cavity, Eq. (3.5).

### *3.3.1.2 Effect of sphere size*

To study the effect of the size of the spheres on the Nusselt number, glass spheres with three different sizes $d = 15.3$ mm, $d = 10.5$ mm, and $d = 5.0$ mm ($d/H = 0.20$, 0.14, and 0.065) in random packings have been examined. The resulting porosity values are $\phi = 49.8$ %, $\phi = 45.3$ %, and $\phi = 42.1$ %, respectively. The corresponding Nu-Ra data points are included in Fig. 3.4, which shows that the Nusselt number reduces with decreasing sphere size. The heat transfer reduction occurs over the entire range of Rayleigh number, but the reduction is strongest at lower Rayleigh numbers. This can be explained by the fact that, although the overall porosities for the three studied sphere sizes are not very different, the local

porosities near the hot/cold vertical walls are much lower for the 5 mm ($d/H$ = 0.065) spheres compared to those for 15.3 mm ($d/H$ = 0.20) spheres.

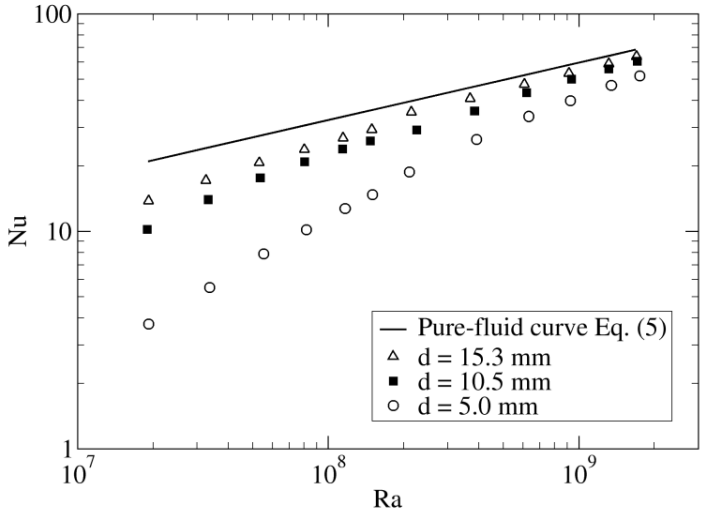


Fig. 3.4. Effect of sphere size. Nu-Ra data for porous media consisting of three different sizes of glass spheres in random packings compared to the pure-fluid reference curve.

#### *3.3.1.3 Effect of a gap between the hot/cold walls and the porous medium*

A 3D printed 4×5×5 simple cubic packing of 15.3 mm (d/H = 0.20) plastic spheres was placed in the cavity to create a gap between the porous medium and the thermally active hot/cold vertical walls. The (dimensionless) gap size is $w/H$ = 0.10, which is larger than the thickness of the thermal and velocity boundary layers obtained from $\delta_T/H = \mathrm{Ra}^{-1/4}$ and $\delta_v = \mathrm{Pr}^{1/2}\delta_T$ [115]. For the working fluids used in this study Pr > 1 so that the velocity boundary layer will be thicker than the thermal boundary layer. The thickness of the velocity boundary is $\delta_v/H$ ~0.039 at the lowest Rayleigh number, and $\delta_v/H$ ~0.014 at the highest Rayleigh number. The Nu-Ra data points obtained from this configuration are plotted in Fig. 3.5, along with the pure-fluid reference curve and the results from the porous medium consisting of 15.3 mm polypropylene spheres without the gap. The figure clearly shows that creating a sufficiently large gap near the thermally active walls can substantially enhance the Nusselt number with respect to the case where the spheres touch these walls. While in the packing without gap the Nusselt number is reduced by 53% at the lowest Ra, and by 13% at the highest Rayleigh number with respect to the pure-fluid cavity, the reduction is only 11% and 0.6% for the cases with a gap between the hot/cold walls and the porous medium. In other words, when the hot/cold walls are not covered by the porous medium, the heat transfer reduction is significantly smaller, and at the highest Rayleigh numbers (Ra > $10^9$) the Nusselt values reach those for the pure-fluid cavity. The reduction of the Nusselt number at low Rayleigh numbers can be explained by the

fact that heat should be convected horizontally from one side of the cell to the other side through the porous medium. At low Rayleigh numbers, the flow length scales are large compared to the pore length scale. Therefore, the flow cannot easily penetrate into the pores and, consequently, the convective transfer of heat in the horizontal direction through the porous medium is hampered. In general, it can be understood that the spheres located close to the vertical hot/cold walls play the most hindering role in the heat transfer mechanism. These observations imply that the interaction between the natural convection flow and the spheres near the hot/cold walls determines most of the heat transfer reduction in a side-heated cavity filled with spheres.

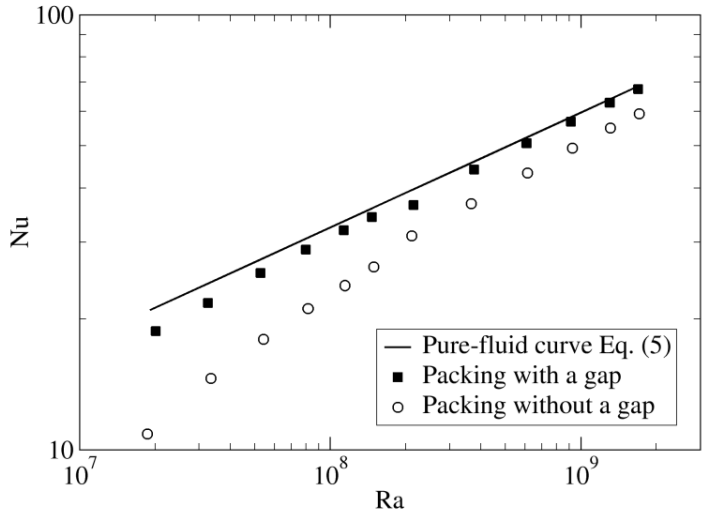


Fig. 3.5. Nu-Ra data for porous media consisting of 15.3 mm polypropylene spheres with and without a gap of $w/H = 0.10$ from the active walls. The solid line represents the pure-fluid reference curve, Eq. (3.5).

### *3.3.1.4 Effect of conductivity ratio*

To study the effect of the solid-to-fluid conductivity ratio in a coarse-grained porous media filled side heated cavity, porous media consisting of 15.3 mm spheres made from four different materials were placed in water and methanol in a BCT packing. The four materials are polypropylene, glass, steel, and brass, with the solid-to-fluid conductivity ratios $k_s/k_f$ listed in Table 3.1. Fig. 3.6 presents the Nu-Ra data points for the four materials along with the pure-fluid curve as a reference. Small discontinuities can be observed at the transition from water to methanol (around $Ra = 2\times10^8$), due to the associated jump in $k_s/k_f$. The results show that the Nusselt number increases with increasing conductivity ratio, for the entire range of Rayleigh numbers considered in this study. It is also observed that if a porous medium consists of highly conductive spheres, it can transport more heat compared to the pure-fluid cavity at sufficiently high Rayleigh numbers. The

increased heat transfer is due to the contribution of both conductive and convective heat transfer. In the studied cases, the heat transfer enhancement at the highest Rayleigh number with respect to the pure-fluid cavity is 29% for the brass spheres and 20% for the steel spheres. For the case with $k_s/k_f = 1$, the heat transfer reduction with respect to the pure-fluid cavity is 14% at the highest Rayleigh number.

The Nusselt number dependency on the conductivity ratio $k_s/k_f$ at a low ($Ra = 2.0\times10^7$), an intermediate ($Ra = 2.0\times10^8$), and a high ($Ra = 1.7\times10^9$) Rayleigh number is plotted in Fig. 3.7 by examining different combinations of the four solid materials and the two fluids. It is observed that the Nusselt number increases with solid-to-fluid conductivity ratio at all Rayleigh numbers. Fig. 3.7 shows that the equations that fit the data-points for all the three Rayleigh numbers are in the form of

$$Nu = Nu_0 (1 + k_s/k_f)^m. \quad (3.6)$$

Table 3.1. Ratio of Solid to fluid conductivity $k_s/k_f$ and ratio of porous medium to fluid conductivity $k_{eff}/k_f$ for the different combinations of solids and fluids considered in this study.

| Sphere and fluid materials | $\frac{k_s}{k_f}$ | $\frac{k_{eff}}{k_f}$ |
|---|---|---|
| Brass - Methanol | 618 | 17.3 |
| Steel - Methanol | 222 | 14.0 |
| Brass - Water | 196 | 13.6 |
| Steel - Water | 70.4 | 9.45 |
| Glass - Methanol | 4.19 | 2.30 |
| Glass - Water | 1.33 | 1.22 |
| Polypropylene - Methanol | 1.00 | 1.00 |
| Polypropylene - Water | 0.32 | 0.79 |

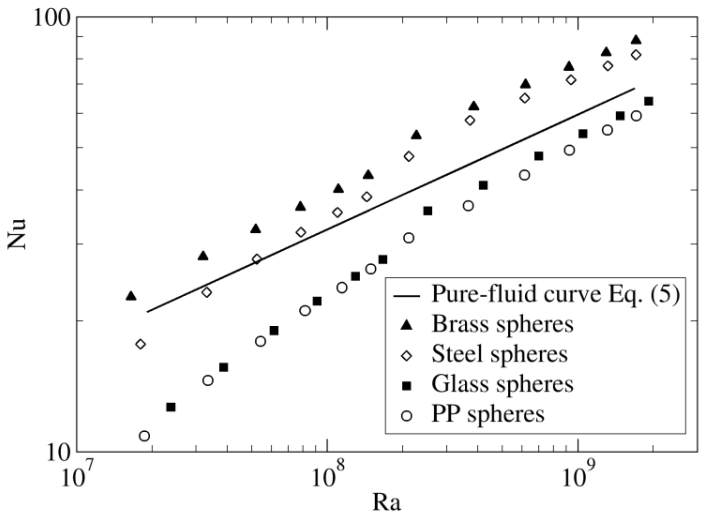


Fig. 3.6. Effect of sphere conductivity. Nu-Ra data for porous media consisting of 15.3 mm ($d/H = 0.20$) spheres in BCT packing with different conductivities compared to the pure-fluid reference curve.

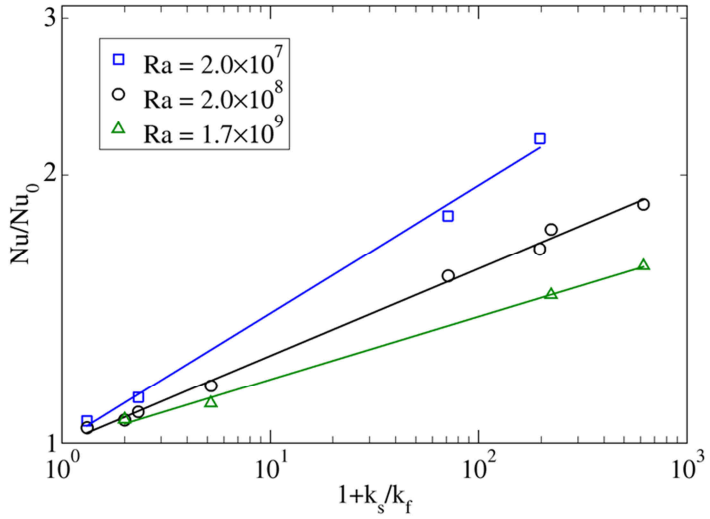


Fig. 3.7. Effect of the solid-to-fluid conductivity ratio on the Nusselt number at three different Rayleigh numbers Ra = $2.0\times10^7$, $2.0\times10^8$, and $1.7\times10^9$. The solid lines denote the fits to the data and represent $Nu = 10.6(1 + k_s/k_f)^{0.14}$, $Nu = 28.8(1 + k_s/k_f)^{0.10}$, $Nu = 55.6(1 + k_s/k_f)^{0.07}$, respectively.

Nusselt number asymptotically approaches a constant value of $Nu_0$ as $k_s/k_f$ goes to zero which represents the cavity filled with adiabatic spheres, where heat transfer is merely due to the fluid convection. The asymptotic values $Nu_0$ are found to be 10.6, 28.8, and 55.6 for the low, the intermediate, and the high Rayleigh numbers, respectively. Fig. 3.7 also shows that as the Rayleigh number increases, the Nusselt number dependency on solid-to-fluid conductivity ratio decreases. This is reflected in a decrease of the value of the slope $m$ value in Eq. (3.6) with increasing Rayleigh number, being 0.14, 0.10, and 0.07 for the low, intermediate,

and high Rayleigh numbers, respectively. This behavior indicates that at higher Rayleigh numbers conduction through the solid structure of a porous medium becomes less important compared to fluid convection.

#### 3.3.1.5 Heat transfer scaling based on porous medium dimensionless numbers

The heat transfer data for eight different solid-fluid combinations reported in the previous section cover a wide range of porous medium Rayleigh numbers $10^2 < Ra_m < 10^5$ (see Eq. (3.3) for definition), and porous medium conductivity ratios $0.79 \leq k_{eff}/k_f \leq 17.3$ (see section 3.2 for definition and Table 3.1). Fig. 3.8 shows $Nu_m\,(k_{eff}/k_f)^{0.49}$ versus $Ra_m$ for all combinations of solids and fluids considered in this study. It is seen that for coarse-grained porous media consisting of $d/H = 0.20$ spheres, $Nu_m$ is correlated to $Ra_m$ and $k_{eff}/k_f$ by the following relation

$$Nu_m = 1.349\, Ra_m^{0.325}\, (k_{eff}/k_f)^{-0.49}. \qquad (3.7)$$

The exponent of $Ra_m$ is found to be 0.325 which is in good agreement with the values that have been reported in the literature for the non-Darcy flow regime [71,72,108,116]. Eq. (3.7) also presents the scaling of $Nu_m$ with the porous medium conductivity ratio $(k_{eff}/k_f)$. This correlation confirms that the porous medium Nusselt number $Nu_m$ cannot be described as a function of $Ra_m$ only, but in addition, there is a strong dependence on thermal conductivity that is captured well by the term $(k_{eff}/k_f)^{-0.49}$. The porous medium Nusselt number $Nu_m$ represents the

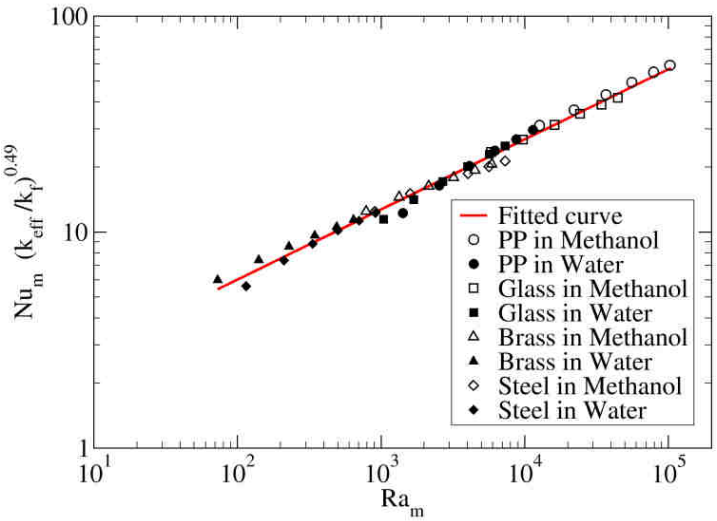


Fig. 3.8. Heat transfer data based on porous medium dimensionless numbers. $Nu_m\,(k_{eff}/k_f)^{0.49}$ versus $Ra_m$ for eight different solid-fluid combinations for 15.3 mm ($d/H = 0.20$) spheres. The red line denotes the fit to the data.

ratio of the total heat transfer over the conduction heat transfer through the combined stagnant fluid plus porous solid medium. At increased thermal

conductivity of the porous medium, a larger fraction of the heat is transferred by conduction compared to convection, and $Nu_m$ (but not Nu) decreases. Overall, the above correlation can be used to determine Nusselt numbers for side-heated natural convection in coarse porous media for a wide range of conductivity ratios $k_{eff}/k_f$ and porous medium Rayleigh numbers, $Ra_m$.

Fig. 3.9 shows $Nu_m (k_{eff}/k_f)^{0.49}$ versus $Ra_m$ for porous media consisting of glass spheres with three different sizes ($d/H = 0.20$, 0.14, and 0.065). The curves fitted to the data show that for $Ra_m$ higher than approximately $10^3$, $Nu_m$ scales with $Ra_m$ to the power 0.33 for $d/H = 0.20$ glass spheres, and to the power 0.36 for $d/H = 0.14$ glass spheres. For smaller $d/H = 0.065$ glass spheres, we observe a transition from a power 0.64 at $Ra_m$ lower than approximately $10^3$, to a smaller power of 0.42 at higher $Ra_m$. Such a decrease in the slope of the $Nu_m$-$Ra_m$ relation with increasing $d/H$ or $Ra_m$ is due to the breakdown of the Darcian behavior and was also observed in other experimental studies which reported values for the $Ra_m$ exponent from 0.61-0.64 [71,117] in the Darcy regime to 0.28-0.33 [71,72,108] when deviating from the Darcy regime at high $Ra_m$ and for larger grains. Theoretical studies suggest a decrease in the slope of the $Nu_m$-$Ra_m$ relation, with $Nu_m$ proportional to $Ra_m^{1/2}$ in the Darcy limit [58] and to $Ra_m^{1/4}$ in the non-Darcy limit [64]. Our present study suggests that for large spheres ($d/H = 0.14$-$0.20$) and $Ra_m$ larger than approximately $10^3$ the flow is non-Darcian, whereas for smaller spheres ($d/H = 0.065$) a transition from Darcy to non-Darcy behavior occurs around $Ra_m = 10^3$.

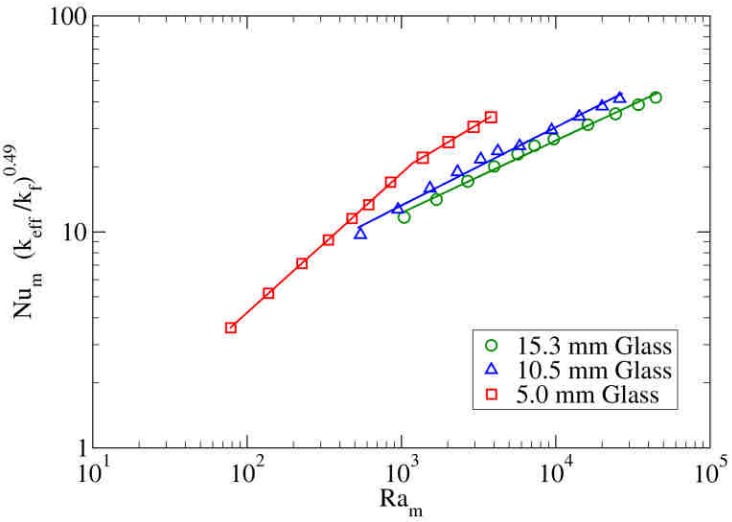


Fig. 3.9. Heat transfer data based on porous medium dimensionless numbers for three different glass sphere sizes ($d/H = 0.20$, 0.14, and 0.065). The solid lines denote power-law fits to the data.

### 3.3.2 Velocity and temperature distribution

PIV and LCT measurement techniques were used to provide insight into the pore-scale flow and heat transfer in differentially side heated coarse porous media. The resulting velocity and temperature fields are reported in this section.

#### *3.3.2.1 Velocity fields*

Fig. 3.10 shows the mean velocity fields in the pure-water cavity (left) and in the cavity filled with 15.3 mm ($d/H = 0.20$) hydrogel spheres in BCT packing (right) at $Ra = 9.0\times10^7$. The mean velocity fields were obtained by averaging over 7200 image pairs that were taken at 1 Hz. The color map represents the distribution of velocity magnitude. The velocity field in the pure-water side-heated cavity is dominated by thin high-velocity boundary layers close to the thermally active hot and cold vertical walls. The flow along the horizontal walls occurs in much thicker layers with much lower velocities, while the flow in the core of the cavity is quiescent. These results are consistent with what has been reported in other studies on pure-fluid differentially heated natural convection at similar Rayleigh numbers [33–35].

Fig. 3.10 shows that in the presence of the coarse porous medium consisting of relatively large solid spheres, the development of a thin high-velocity layer along the vertical walls is substantially hindered. Instead, a wavy behavior with local maxima and minima in velocity is observed. This wavy behavior is also visible in Fig. 3.12, which presents the vertical velocity component ($v_z$) along a vertical line very close to the hot wall at $x/H = 0.03$. In Fig. 3.11 the velocity magnitude color map is shown on a logarithmic scale in order to be able to observe the flow distribution in the regions away from the walls. It shows that a portion of the fluid penetrates into the adjacent pores and is thus channeled away from the main stream along the active hot/cold walls. Consequently, there is less interaction between the fluid and the hot/cold walls, which contributes to the heat transfer reduction with respect to the pure-fluid cavity, see red crosses in Fig. 3.2. This also explains the heat transfer results for the case with a gap between the active vertical walls and the porous medium presented in section 3.3.1.3. When the gap is sufficiently large to allow for the formation of the thin high-velocity boundary layer, the heat transfer reduction will be small.

To make a quantitative comparison of the local velocity distributions for the two studied cases, Fig. 3.13 depicts profiles of the vertical velocity component ($v_z$) along three horizontal lines at $z/H = 0.5$, 0.6, and 0.7. The velocity profiles in Fig. 3.13 as well as in Fig. 3.12 show that the local velocity can be higher or lower depending on the vertical position.

Fig. 3.14 shows profiles of the horizontal velocity component ($v_x$) along three vertical lines at $x/H = 0.37$, 0.50, and 0.63 for the pure-water and hydrogel sphere

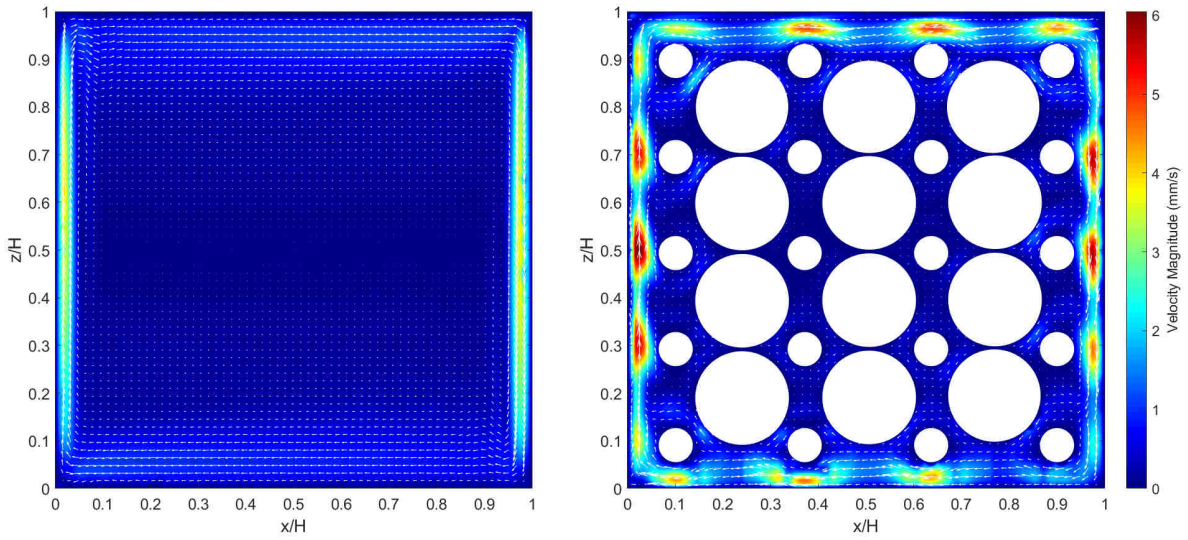


(a) (b)

Fig. 3.10. Mean velocity field at Ra = $9.0\times10^7$ (a) in the pure-water cavity, and (b) in the cavity filled with 15.3 mm hydrogel spheres in BCT packing.

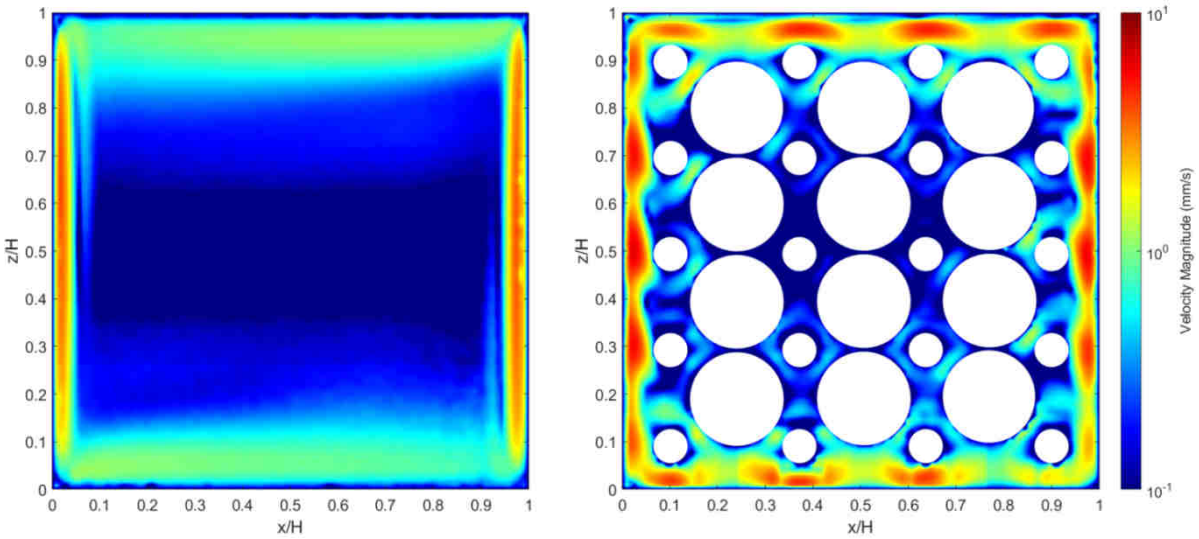


(a) (b)

Fig. 3.11. Mean velocity magnitude shown on a logarithmic scale at Ra = $9.0\times10^7$ (a) in the pure-water cavity, and (b) in the cavity filled with 15.3 mm hydrogel spheres in BCT packing.

filled cavity. The results in this figure and in Fig. 3.10 show that in the pure-water cavity the horizontal flow from one side of the cavity to the opposite side occurs over a relatively thick layer with relatively low velocities. In the cavity filled with spheres, the horizontal flow is more concentrated near the horizontal walls with significantly higher maximum velocities. (i.e. a factor of about 4.5 higher maximum horizontal velocity compared to the pure-water cavity). The slight heat

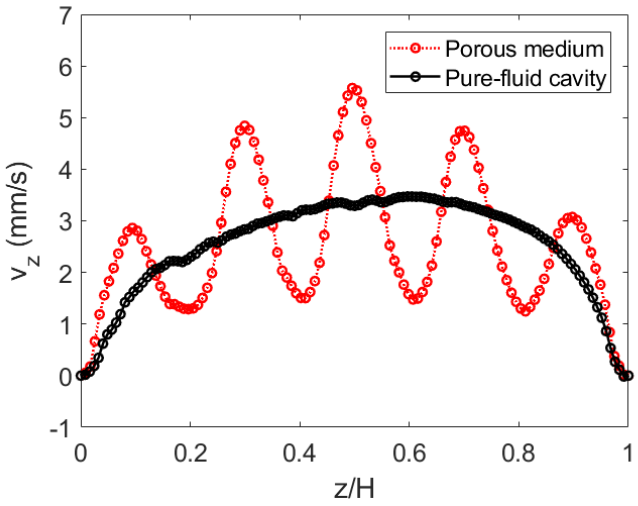


Fig. 3.12. Mean vertical velocity $v_z$ along a vertical line close to the hot wall at $x/H = 0.03$ for the pure-water cavity (black markers), and for the cavity filled with hydrogel spheres (red markers) at Ra = $9.0\times10^7$.

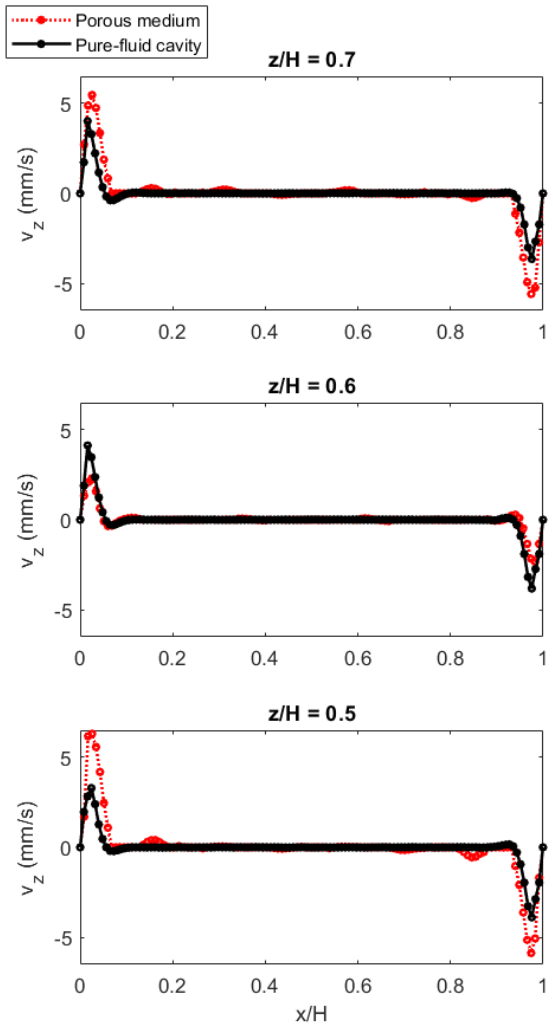


Fig. 3.13. Mean vertical velocity $v_z$ along horizontal lines ($z/H$ = 0.50, 0.60, and 0.70) for the pure-water cavity (black markers), and for the cavity filled with hydrogel spheres (red markers) at Ra = $9.0\times10^7$

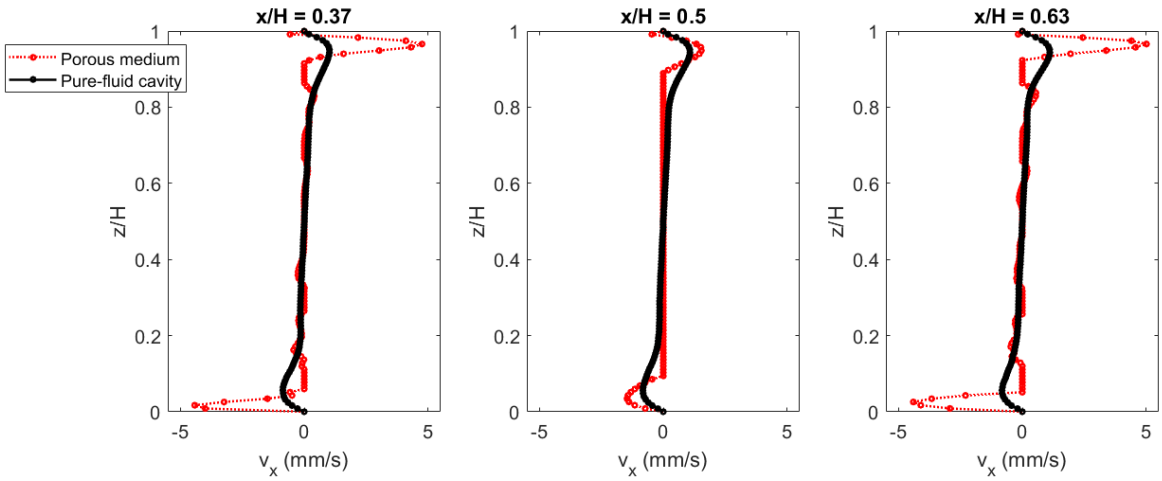


Fig. 3.14. Mean horizontal velocity $v_x$ along three vertical lines ($x/H = 0.37$, 0.50, and 0.63) for the pure-water cavity (black markers), and for the cavity filled with hydrogel spheres (red markers) at Ra = $9.0\times10^7$.

transfer reduction observed in Fig. 3.5 (section 3.3.1.3) for the case in which there is a gap between the vertical walls and the packing, relative to the pure-fluid cavity, could be due to the fact that the horizontal flow is hindered and confined to the region between the spheres and the horizontal walls. According to the heat transfer results, the hindering effect of the porous medium in the horizontal direction only accounts for 22% (at the lowest Ra) and 4.8% (at the highest Ra) of the total heat transfer reduction.

### *3.3.2.2 Temperature fields*

Fig. 3.15 shows the mean temperature fields obtained from LCT measurements in the pure-water cavity (left) and in the cavity filled with 15.3 mm ($d/H = 0.20$) hydrogel spheres in BCT packing (right). In both cases, the temperatures of the cold and hot walls were 20.0 °C and 30.2 °C, respectively, leading to Ra = $9.0\times10^7$. The temperature field in the pure-water cavity shown in Fig. 3.15a illustrates the characteristic stratification in the core of the cavity and the thin thermal boundary layers along the vertical hot/cold walls. The stratified temperature distribution was also reported in previous studies on differentially heated natural convection in pure-fluid cavities at similar Rayleigh numbers [33,35]. The temperature field in the cavity filled with spheres shown in Fig. 3.15b is very different from that in the pure-water cavity. While in the pure-water cavity isotherms are horizontal, in the cavity filled with spheres, these are tilted with the temperature gradient roughly in the diagonal direction. The reason is that a portion of the high-velocity flow near the hot/cold vertical walls diverts away from the walls and penetrates into the pores and subsequently moves diagonally towards the opposite corner. This is consistent with the observations in the velocity fields in

Fig. 3.11. The absence of temperature stratification also implies that the overall strength of convection decrease in the cavity filled with spheres, which leads to a reduced convective heat transfer as evidenced in the Nu-Ra results. Fig. 3.16 compares the fluid temperature profiles averaged over vertical lines spanning the entire height of the cavity ($H$) for the pure-water cavity and the cavity filled with spheres (excluding the locations occupied by the spheres), as a function of $x/L$. It can be seen that in the pure-water cavity, the temperature profile is nearly horizontal in the core region of the cavity and significant temperature variations take place only in the thin thermal boundary layers close to the hot/cold walls. In the cavity filled with spheres, the vertically-averaged fluid temperature profile clearly reflects the presence of the spheres, and on average varies much more gradually from one vertical plate to the other. Fig. 3.17 compares the vertically-averaged fluid temperature profiles in a narrow region near the cold wall $0.965 \leq x/H \leq 1$. (The cold wall is chosen due to the higher color-temperature sensitivity of the liquid crystals in the colder part of the effective temperature range which leads to higher accuracy.) This figure shows that the gradient of the vertically-averaged temperature profile near the cold wall is smaller for the cavity filled with spheres compared to that for the pure-water cavity. The overall Nusselt number is defined as $\mathrm{Nu} = q_{\mathrm{av}} H / (k_{\mathrm{f}} \Delta T)$ where $q_{\mathrm{av}}$ is the average heat flux (in W/m$^2$) at the cold wall. The heat flux at the cold wall is proportional to the slope of

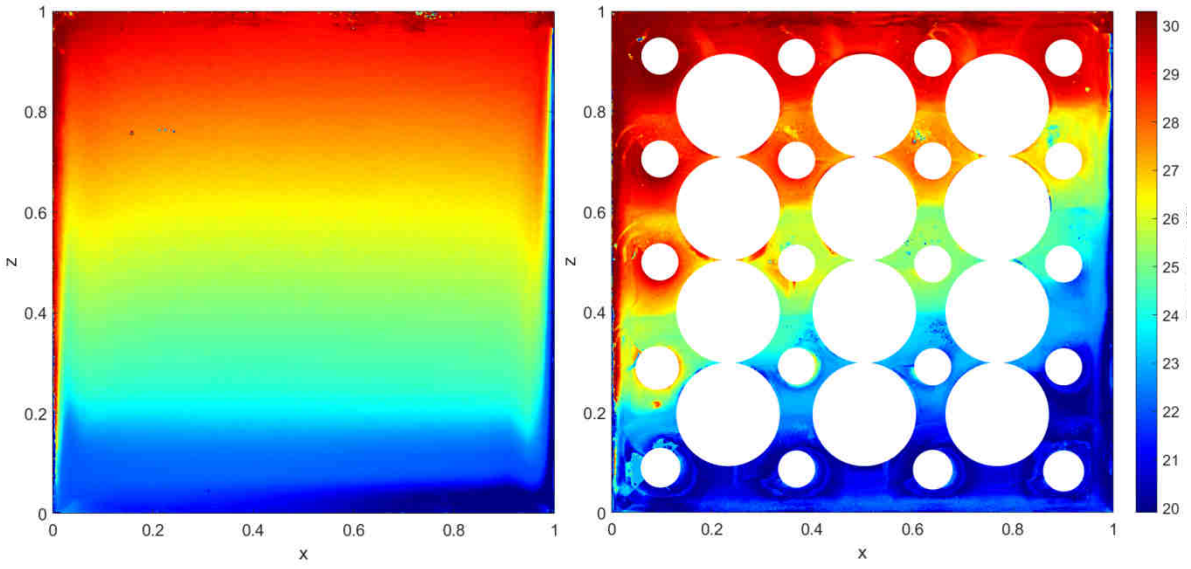


(a) (b)

Fig. 3.15. Mean temperature fields (a) in the pure-water cavity, and (b) in the cavity filled with hydrogel spheres of 15.3 mm diameter in BCT packing. The temperatures of the cold and hot side walls were 20.0 °C and 30.2 °C, respectively, resulting in a Rayleigh number of $\mathrm{Ra} = 9.0 \times 10^7$.

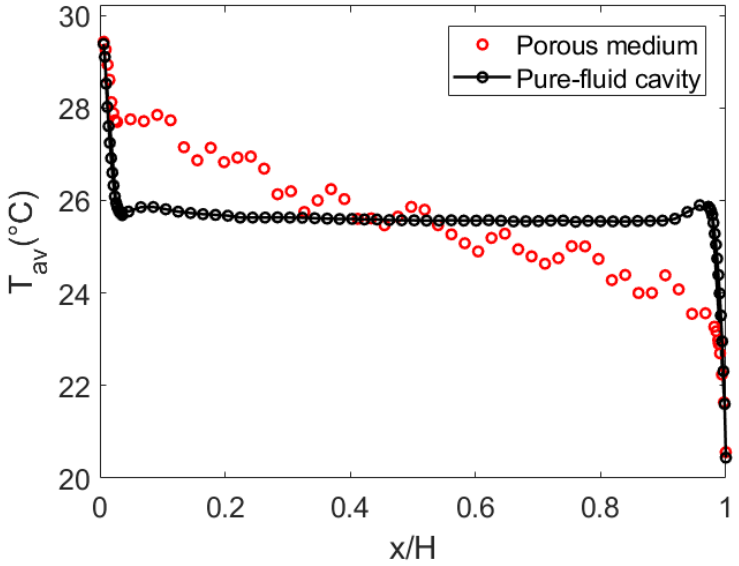


Fig. 3.16. Vertically-averaged temperature profiles for the pure-water cavity (black markers), and for the cavity filled with hydrogel spheres (red markers) at Ra = $9.0\times10^7$.

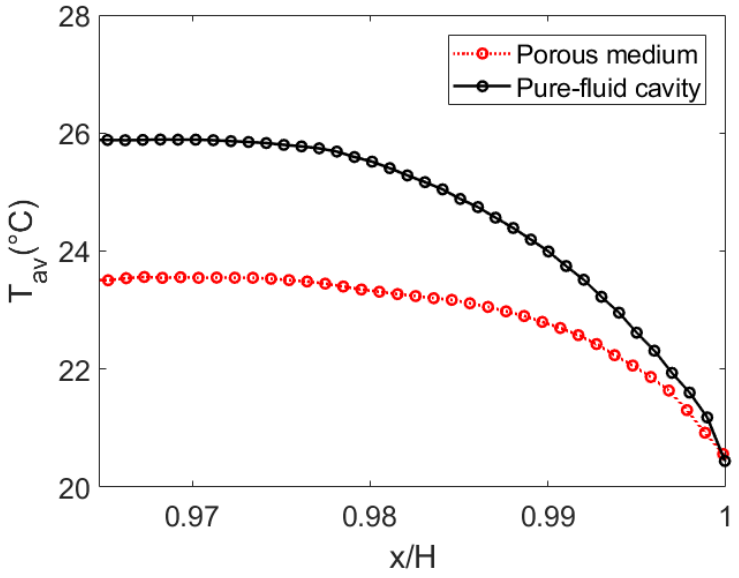


Fig. 3.17. Vertically-averaged temperature profiles at the cold wall for the pure-water cavity (black markers), and for the cavity filled with hydrogel spheres (red markers) at Ra = $9.0\times10^7$.

the vertically-averaged temperature profile (Fig. 3.17) at the wall at $x/H = 1$, i.e. $q_{av} = -k_f\,(\mathrm{d}T_{av}/\mathrm{d}x)|_{x=H}$. The reduced slope of the vertically-averaged temperature profile at the cold wall illustrates the reduced Nusselt number due to the presence of the porous medium. Fig. 3.17 shows that the slope of the vertically-averaged temperature profile at the cold wall for the cavity filled with spheres is approximately 30% smaller than that for the pure-water cavity which is consistent

with the 30% reduction of heat transfer at the same Rayleigh number seen in Fig. 3.2 (red crosses).

To study the temperature distributions at the cold wall in more detail, and to better understand the behavior of the temperature profiles at different heights, Fig. 3.18 shows temperature profiles along four horizontal lines at $z/H = 0.2, 0.4, 0.6,$ and 0.8. It can be seen that in the upper part of the cold wall at $z/H = 0.8$ the temperature gradients near the cold wall are very high for both cases and even higher for the cavity filled with spheres. This leads to a high heat flux in the upper part of the cold wall for both cases. However, when moving towards the bottom of the cavity, the temperature gradient at the cold wall reduces more significantly for the cavity filled with spheres compared to the pure-water cavity. At $z/H = 0.2$, the temperature is almost uniform near the cold wall so that the heat flux is almost zero at the lower part of the cold wall in the cavity filled with spheres. On the other hand, for the pure-water cavity, the heat flux reduces to a lesser extent from top to the bottom and there is a considerable temperature gradient at $z/H = 0.2$. This implies that the local Nusselt number at the hot and cold walls is less uniform for the cavity filled with spheres, and that the reduction in overall Nusselt number for the cavity filled with spheres is mostly caused by the very low heat flux in the lower part of the cold wall (and the upper part of the hot wall).

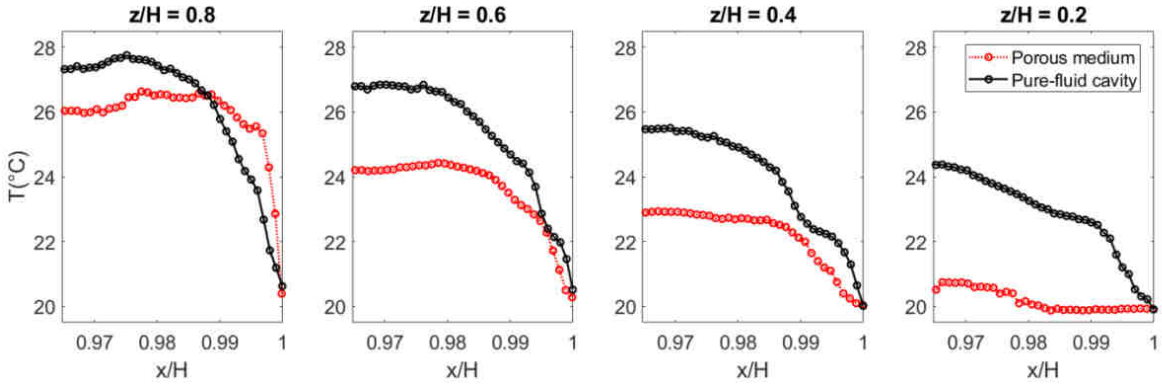


Fig. 3.18. Temperature profiles along four horizontal lines ($z/H = 0.2, 0.4, 0.6,$ and 0.8) for the pure-water cavity (black markers), and for the cavity filled with hydrogel spheres (red markers) at Ra = $9.0\times10^7$.

## 3.4 Conclusions

Natural convection flow and heat transfer in a differentially side heated cubic cavity filled with coarse porous media consisting of relatively large spheres were studied experimentally. Nusselt numbers were measured for fluid Rayleigh numbers varying between $10^7$ and $10^9$, solid-to-fluid conductivity ratios ranging from 0.32 to 618, three different sphere sizes ($d/H = 0.065, 0.14, 0.20$), and three

different packing types (body-centered tetragonal, simple cubic, and random). A partially-filled cavity with a gap between the porous medium and the hot/cold walls was also considered.

It was found that the Nusselt number is reduced in the cavity filled with spheres compared to the pure-fluid cavity, unless the solid spheres are highly conductive. The Nusselt number reduction is higher for smaller spheres and is not very sensitive to the packing type, especially at high Rayleigh numbers. For the porous medium with a gap between the hot/cold walls and the spheres, the heat transfer reduction is significantly smaller and the Nusselt numbers reach those for the pure-fluid cavity at the highest Rayleigh numbers ($Ra > 10^9$). The following Nusselt number correlation was derived for coarse porous media with $d/H = 0.2$

$$Nu_m = 1.349\ Ra_m^{0.325}\ (k_{eff}/k_f)^{-0.49}$$

for porous medium Rayleigh numbers $10^2 < Ra_m < 10^5$ and porous medium conductivity ratios $0.79 \leq k_{eff}/k_f \leq 17.3$. This expression takes into account the strong dependence of the porous medium Nusselt number on the porous medium conductivity ratio, and its scaling with the porous medium Rayleigh number is consistent with the power-law scaling reported in the literature for the non-Darcy regime.

Measured velocity and temperature fields show that the layers of spheres close to the vertical hot/cold walls hinder the formation of high-velocity boundary layers and divert a portion of the fluid away from these walls towards the inner pores. This phenomenon reduces the temperature stratification in the core of the cavity and leads to a reduced mean temperature gradient at the walls, which explains the heat transfer reduction in porous media.

It is also concluded that, although the overall Nusselt number is lower for the cavity filled with a coarse-grained porous medium, the local Nusselt number at the cold/hot walls can be significantly higher than in the corresponding pure-fluid cavity. The presence of a coarse-grained porous medium thus causes strong non-uniformities in the local wall heat transfer, leading to so-called hot-spots which may have severe consequences in practical applications such as lowering the lifespan of blast furnace refractory walls.

# Chapter 4

# Experiments on Mixed Convection in a Vented Differentially Side-heated Cavity Filled with a Coarse Porous Medium*

This chapter reports on an experimental study of mixed convection flow and heat transfer in a vented, differentially side-heated cubical cavity filled with a porous medium consisting of relatively large solid low-conductivity spheres. Rayleigh numbers and Reynolds numbers are varied over the ranges $6 \times 10^6 < \mathrm{Ra} < 7 \times 10^7$ and $240 < \mathrm{Re} < 4250$, respectively, for a fixed Prandtl number of $\mathrm{Pr} = 6.75$, thus covering more than three decades in Richardson numbers $\mathrm{Ri} = \mathrm{Ra}/(\mathrm{Re}^2\,\mathrm{Pr})$. Heat transfer measurements were combined with measurements of the velocity field (using particle image velocimetry) and the temperature field (using liquid crystal thermography) to better understand the dependence of the Nusselt number, Nu, on the Richardson number. We observed three different flow and heat transfer regimes depending on the Richardson number. For $\mathrm{Ri} < 10$, the flow structure and the Nusselt number scaling are similar to those for the pure forced convection, i.e., the Nusselt number scales as $\mathrm{Nu} \sim \mathrm{Re}^{0.61}$ independent of Rayleigh number. For $\mathrm{Ri} > 40$, natural convection dominates the flow in the vicinity of the heating wall. The Nusselt number becomes less sensitive to the Reynolds number and is mainly determined by the Rayleigh number. In the intermediate regime for $10 < \mathrm{Ri} < 40$, the upward directed natural convection flow at the heating wall competes with the downward directed forced flow leading to a minimum effective Nusselt number. A Nusselt number correlation is derived that is valid in the range $0.1 < \mathrm{Ri} < 100$ covering all three regimes.

* This chapter has been published in the *International Journal of Heat and Mass Transfer*, 149, 119238 (2020).

## 4.1 Introduction

Natural convection in closed cavities has been among the most widely studied topics in fluid dynamics due to its simple geometry and relevance to many engineering applications. Natural convection is characterized by the Rayleigh number, Ra, which measures the strength of the buoyancy forces relative to diffusive forces, and the Prandtl number, Pr, which is the ratio of the kinematic viscosity to the thermal diffusivity of the working fluid. When inlet and outlet vents are added to such a cavity, forced convection is introduced to the system as well, and, as a consequence, the Reynolds number, Re, also plays a role. Mixed convection is a result of the interaction between natural and forced convection and their relative strength is measured by the Richardson number $Ri = Ra/(Re^2 Pr)$. Mixed convection in vented cavities has attracted extensive attention during the past decades due to its application in, for example, electronics cooling [41,50], indoor air conditioning [43,118,119], solar ponds [120], and energy storage systems [121]. Various vented mixed convection configurations with different heating/cooling sources and inlet/outlet locations have been studied and the results have been reported in the form of flow and temperature fields and dimensionless heat transfer coefficients (i.e., Nusselt numbers, Nu) for a range of Rayleigh and Reynolds numbers [43,50,118], [49,122–129]. These studies are almost exclusively numerical studies solving the Navier-Stokes equations for two-dimensional geometries. Singh and Sharif [49] conducted a numerical study of a vented cavity with differentially heated side walls. They examined six different configurations of inlet and outlet locations and determined Nusselt numbers and spatially-averaged temperatures for Reynolds numbers from 50 to 500 and Richardson numbers from 0 to 10. They concluded that the configurations in which forced and natural convection assist each other produce more effective cooling. Deng et al. [43] numerically studied airflow and heat/contaminant transport structures in a vented cavity with discrete heat and contamination sources. They observed different transport structures and ventilation modes depending on the relative strength of natural convection and forced convection, which is important in determining the indoor air environment. Papanicolaou and Jaluria [50] numerically studied mixed convection in a vented cavity with an isolated thermal source for Reynolds numbers between 50 and 2000 and Richardson numbers between 0 and 10. They found a general trend of increase of the average heat transfer rate from the source to the airflow when the Richardson number increases at a fixed Reynolds number as well as when the Reynolds number increases at a fixed Richardson number. They also reported on the effect of the location of the heat source and the outlet port.

Mixed convection in vented cavities filled with porous media or solid obstacles has several industrial applications, for example in grain storage, food storage, solar

collectors, steel making furnaces, and electronics cooling. Despite its practical relevance, it has received much less attention than the case without porous media. Mahmud and Pop [63] were the first to publish on mixed convection in vented cavities filled with a porous medium. They numerically studied two-dimensional steady mixed convection using the Darcy flow model for porous medium Peclet numbers between 0.1 and 100, porous medium Rayleigh numbers between 0.1 and 1000, and inlet width to cavity height ratios between 0.1 and 0.6. The studied cavity was heated/cooled at the left wall and the forced flow was directed along the hot/cold wall with inlet and outlet vents at the top and bottom of the wall. They found that the flow pattern can change from a unicellular flow to a multicellular flow depending on the inlet width ratio, Peclet number, and Rayleigh number. Bhuiyan et al. [130] performed a similar study but considered three different cavity aspect ratios. Other researchers have studied vented cavities partially filled with porous media [131,132]. These studies used the Darcy model and its extensions, and solved volume-averaged continuum equations for the fluid and solid constituents.

In many of the above-mentioned applications of mixed convection in vented cavities, the porous medium consists of relatively large grains/obstacles. An example is the mixed convection at the hearth of steelmaking blast furnaces where the liquid iron is collected and tapped off [133]. The hearth is filled with relatively large coke particles with a typical size up to approximately 100 mm. With the hot liquid iron flowing in from the top, and leaving from the exit taphole, while the walls of the hearth are being cooled, the flow of liquid iron in the hearth is a mixed convection flow in a coarse-grained porous medium. Other examples include electronics cooling with relatively large electronic components [73] and cooling and storage of food packages and agricultural products [134]. In these cases, the pore length scale is not small compared to the flow and thermal length scales, and the validity of the Darcy model and the volume-averaged porous continuum approach is questionable. Moreover, for coarse porous media, it becomes more important to capture the details of the flow field and the temperature distribution at the pore-scale and to resolve the strong interaction between the flow and the solid grains. In this regard, a few of our recent studies have considered natural convection in closed cavities containing relatively large solid spheres at the pore level both experimentally [112,135] and numerically [1].

This study focuses on mixed convection in vented cavities filled with coarse-grained porous media. The objective is to provide detailed experimental data on the heat transfer scaling as a function of Reynolds and Rayleigh numbers. For this purpose, we used a cubical cavity with differentially heated side walls equipped with an inlet at the heating side and an outlet at the cooling side. The cavity is packed with relatively large solid spheres. To better understand the heat transfer

results, we also determined the velocity fields and temperature fields in the pores by using optical measurement techniques in conjunction with a refractive index matched porous medium.

## 4.2 Experimental setup

The experimental setup consists of a cubical cavity with an inner dimension of $L = 77$ mm (see Fig. 4.1a). The cavity has one hot and one cold side wall which are made of copper and the other four walls are made of 4 mm thick glass. The hot wall was heated by an electrical foil heater (Minco HK5955) and the cold wall was internally cooled with water from a temperature-controlled water circulator (Julabo FP51-SL). To minimize the heat leakage, the glass walls and the heating wall were completely insulated during heat transfer measurements using thick polystyrene sheets (see Fig. 4.1a). The cavity is equipped with an inlet port at the heating wall and an outlet port at the cooling wall with each port having an internal size of $h \times L = 10$ mm $\times$ 77 mm. The remaining heating/cooling area is $H \times L =$ 62 mm $\times$ 77 mm (see Fig. 4.1a). Fig. 4.1b illustrates two different mixed convection configurations A and B, and a pure forced convection configuration C considered in this study. The main focus of this study is on configuration A in which the inlet port is at the top of the heating wall and the outlet port at the bottom of the cooling wall. For comparison, a few experiments were performed in configuration B which results from rotating the same cavity positioned in configuration A about the x-axis. In configuration B, the inlet port is located at the bottom of the heating wall and the outlet port at the top of the cooling wall. To obtain pure forced convection data points, the same cavity was rotated about the y-axis such that the heating wall is at the top and the cooling wall is at the bottom, see configuration C in Fig. 4.1b. In this configuration, there is no natural convection and only forced convection takes place. In the heat transfer experiments, the cavity was filled with polypropylene spheres with a diameter $d = 15.3$ mm ($d/L = 0.20$) and solid-to-fluid conductivity ratio of $k_s/k_f = 0.32$. The spheres were packed in a Body-Centered Tetragonal (BCT) packing structure (see Fig. 4.1).

The temperature of the heating and cooling walls, $T_h$ and $T_c$, were monitored by four ultra-precise four-wire RTD sensors (Omega RTD-3-1PT100K2528-1M-T-1/10) with an inaccuracy of ± 0.03 °C. The same type of RTD sensors were used to measure the inflow temperature $T_{in}$ and the outflow temperature $T_{out}$. The inflow and the cold wall were kept at the same temperature $T_{in} = T_c$. The Rayleigh number is determined using the temperature difference between the heating wall and the inflow/cooling wall as in

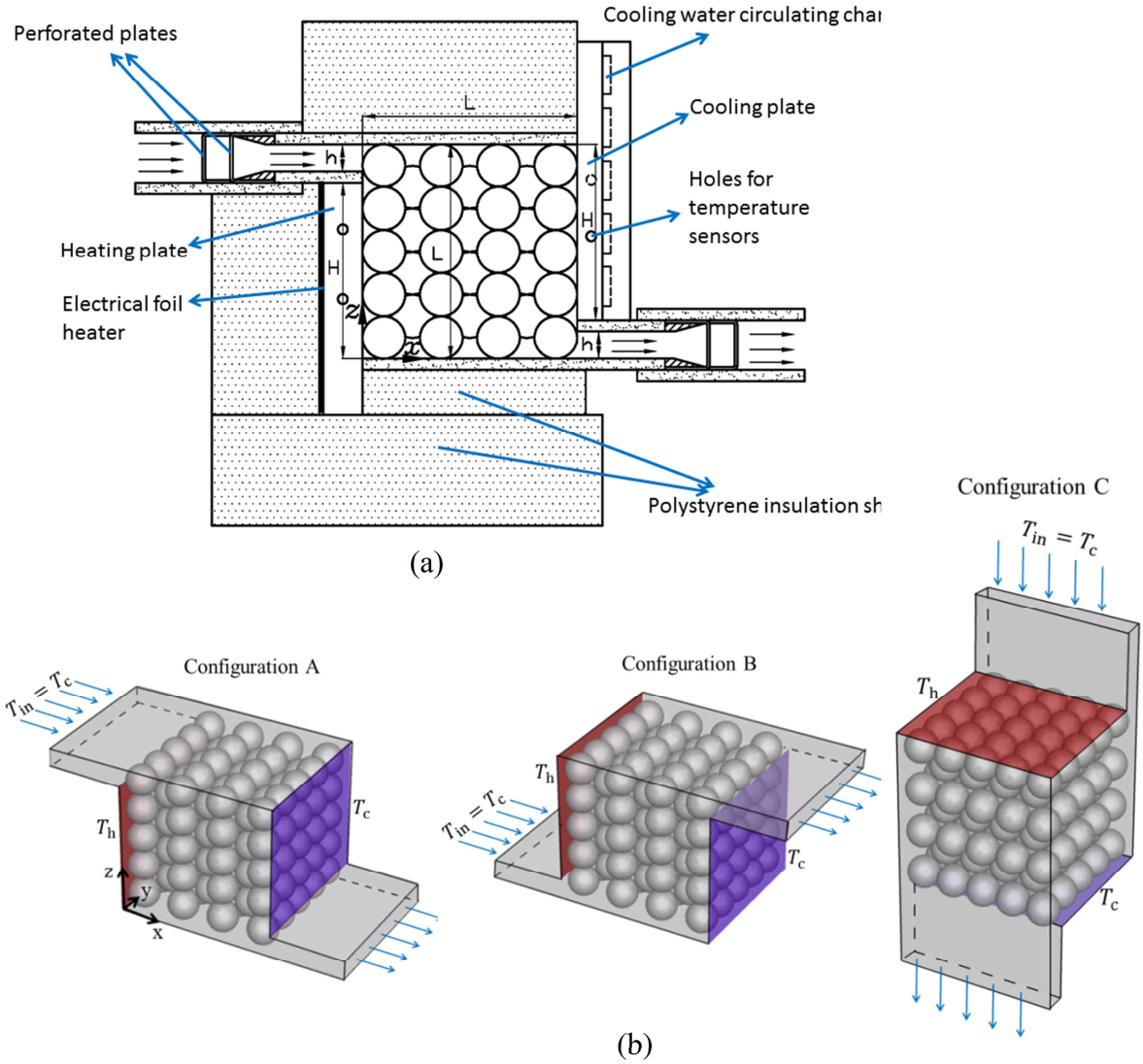


Fig. 4.1 The mixed convection cavity filled with $d/L = 0.20$ spheres in BCT packing: (a) Drawing and components of the cavity (configuration A), (b) Schematic view of the two studied mixed convection configurations A and B, and the pure forced convection configuration C. In all experiments the same cavity was used positioned in three different ways (Configuration A, B, and C). Results will be presented in the Cartesian coordinate system shown in Fig. 4.1b.

$$\mathrm{Ra} = \frac{\beta g (T_\mathrm{h} - T_\mathrm{in}) H^3}{\nu \alpha}, \tag{4.1}$$

where $g$ is the gravitational acceleration and $\beta$, $\nu$ and $\alpha$ are the thermal expansion coefficient, the kinematic viscosity, and the thermal diffusivity of the working fluid, respectively. The Nusselt number is determined using the electrical power supplied to the heating wall $P$ as in

$$\mathrm{Nu} = \frac{P - Q_{\mathrm{loss}}}{kH(T_{\mathrm{h}} - T_{\mathrm{in}})}, \tag{4.2}$$

where $k$ is the thermal conductivity of the working fluid. Water was used as the working fluid in all the experiments. $Q_{\mathrm{loss}}$ is the minor heat loss and is determined by measuring the heat transfer in the water-filled vented cavity positioned as in configuration C (see Fig. 4.1b), with closed inflow and outflow. In this situation, both natural and forced convection are inactive and the fluid is stagnant so that only conduction occurs. The measured heat transfer minus the known conductive heat transfer through the stagnant water layer only is considered as the heat loss in this system. The water inflow into the cavity was supplied by a temperature-controlled water bath (Julabo F32-HE). A rotary vane pump (Fluid-o-Tech PA111) was used to provide a constant volumetric flowrate from the water bath into the cavity. A variable frequency drive (Hitachi L100) was used to vary the volumetric flowrate by regulating the rotational speed of the pump motor. The volumetric flowrate was measured and monitored using a magnetic flowmeter (MAG-VIEW MVM-002-Q). The Reynolds number is determined using the inflow volumetric flowrate $\dot{V}$ as in

$$\mathrm{Re} = \frac{u_{\mathrm{in}} L}{\nu} = \frac{\dot{V}}{\nu h}, \tag{4.3}$$

where $u_{\mathrm{in}} = \dot{V} / (h \times L)$ is the bulk velocity of the water inflow/outflow. Using the Rayleigh and Reynolds numbers, the Richardson number can be obtained from

$$\mathrm{Ri} = \frac{\mathrm{Ra}}{\mathrm{PrRe}^2}, \tag{4.4}$$

where Pr is the Prandtl number of the working fluid. For water, at room temperature (22 °C) the Prandtl number is 6.75. In section 4.3.5. we study how the heat generated at the heating wall is distributed between the two heat removal pathways: the cooling wall, and the outflow. For this purpose, we introduce another dimensionless number which is the ratio of the heat leaving the cavity by the outflow, $Q_{\mathrm{flow}}$, and the total heat supplied to the hot wall, $Q_{\mathrm{total}}$, as in

$$\frac{Q_{\mathrm{flow}}}{Q_{\mathrm{total}}} = \frac{\rho \dot{V} c_{\mathrm{p}} (T_{\mathrm{out}} - T_{\mathrm{in}})}{P}, \tag{4.5}$$

where $\rho$ and $c_{\mathrm{p}}$ are the density and the specific heat capacity of the working fluid. In this study, the Rayleigh number is varied over the range $6 \times 10^6 < \mathrm{Ra} < 7 \times 10^7$ by varying the temperature difference $T_{\mathrm{h}} - T_{\mathrm{in}}$ between approximately 2 °C and 20

°C. The Reynolds number is varied over the range $240 < Re < 4250$ by varying the incoming volumetric flowrate from $2.4 \times 10^{-6}$ m$^3$/s to $4.2 \times 10^{-5}$ m$^3$/s. Consequently, the Richardson number is varied over a wide range of three decades, i.e., $0.1 < Ri < 100$. Depending on the set temperature difference $T_h - T_{in}$ and the set flowrate $\dot{V}$, the uncertainties in the measured Reynolds, Rayleigh, and Nusselt numbers are between 1.7 % and 3.6 %, 1.8 % and 3.9 %, and 1.5 % and 3.7 %, respectively. The resulting uncertainty for the Richardson number is between 3.9 % and 8.2 %.

As discussed in [112], refractive index matching of water and hydrogel spheres enables the use of optical measurement techniques for thermally-driven flows in porous media. In this study, we used hydrogel spheres in water ($k_s/k_f = 1$) to make a refractive index matched porous medium to be able to perform Particle Image Velocimetry (PIV) and Liquid Crystal Thermography (LCT) measurements. Hydrogel spheres with a diameter of approximately 15.3 mm ($d/L = 0.20$) were packed in a BCT structure. The PIV and LCT images were taken at the vertical plane $y/L = 0.4$, see Fig. 4.1.

Details of the PIV experimental setup are reported in [112]. The post-processing of PIV images was conducted using the commercial software Davis 8.4.0. A three-pass cross-correlation with final interrogation area of $16 \times 16$ pixels and 50 % overlap was used to obtain velocity fields with a vector resolution of 0.60 mm. The time difference between the PIV image pairs, $\Delta t$, was varied from $\Delta t = 3$ ms at the highest flowrate to $\Delta t = 30$ ms at the lowest flowrate in order to have a maximum particle displacement of around 8 pixels. The mean velocity fields were obtained by averaging over 7200 instantaneous velocity fields that were acquired at 2 Hz. It was checked that, during the 1 hour duration of measuring the mean velocity fields, the hot and the cold wall temperatures varied by less than 1 % of the lowest temperature difference and the liquid flowrate varied by less than 3 % of the lowest flowrate.

The LCT measurements were performed to determine the temperature distribution at the pore level in the porous medium. The LCT experimental setup is described in detail in [112]. The useful temperature range of the thermochromic liquid crystals used in this study (Hallcrest R25C60W) was determined to be from 21.6 °C to 31.1 °C. Accordingly, in the LCT experiments the cooling wall and the inflow temperatures were set to $T_{in} = T_c = 21.6$ °C, and the heating wall temperature was set to $T_h = 31.1$ °C which leads to a Rayleigh number of $Ra = 3.5 \times 10^7$. The color images of the thermochromic liquid crystals were finally converted to quantitative temperature fields based on a temperature-hue calibration procedure which is described in [112].

## 4.3 Results and discussions

### 4.3.1 Flow and heat transfer in the cavity with and without porous media

The Nusselt number was measured as a function of Reynolds number in the vented cavity with an inlet at the top of the heating wall and outlet at the bottom of the cooling wall (Configuration A, see Fig. 4.1b). The Nusselt numbers were measured both in the pure-fluid cavity without porous medium and in the same cavity filled with a porous medium consisting of a BCT packing of $d/H = 0.2$ spheres to identify the effect of the porous medium on the heat transfer. Fig. 4.2 shows the resulting Nu-Re data for two different Rayleigh numbers. It is observed that the heat transfer rate from the heating wall increases with Reynolds number in all cases. However, the slope of the Nu-Re curve is higher for the porous medium filled cavity. At low values of the Reynolds number, where natural convection dominates, the Nusselt number is higher for the pure-fluid cavity. This is consistent with what is reported for natural convection in side-heated cavities with and without porous media [135]. When increasing the Reynolds number, the Nusselt numbers for the porous medium filled cavity exceed those for the pure-fluid cavity. Fig. 4.3 shows that at low Reynolds number (Re = 280) in the porous medium filled cavity a portion of the cold inflow tends to move downward opposing the upward moving natural convection flow. However, in this case, the upward directed natural convection flow is sufficiently strong to prevent the cold inflow from reaching the hot wall. In this situation, hot fluid gets trapped in the region near the heating wall due to the presence of the spheres and the opposing inflow, resulting in a heat transfer rate lower than that for the pure-fluid cavity.

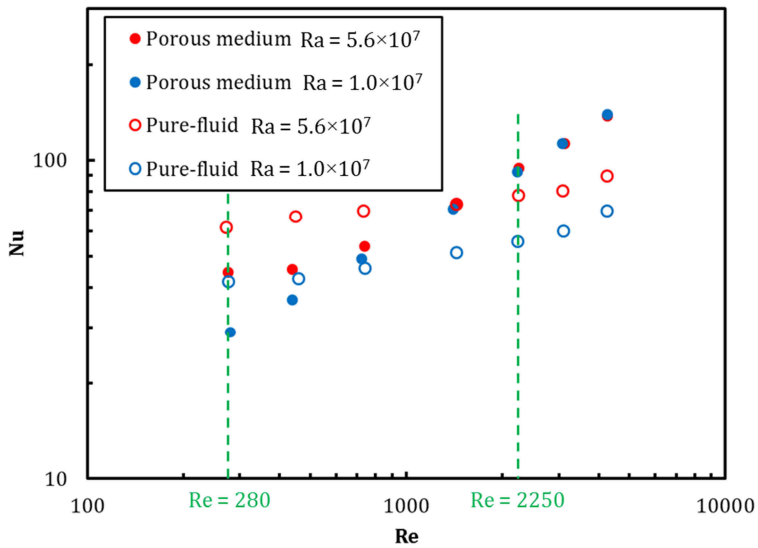


Fig. 4.2. Nu-Re data for the porous medium filled cavity compared to the pure-fluid cavity at two different Rayleigh numbers in configuration A.

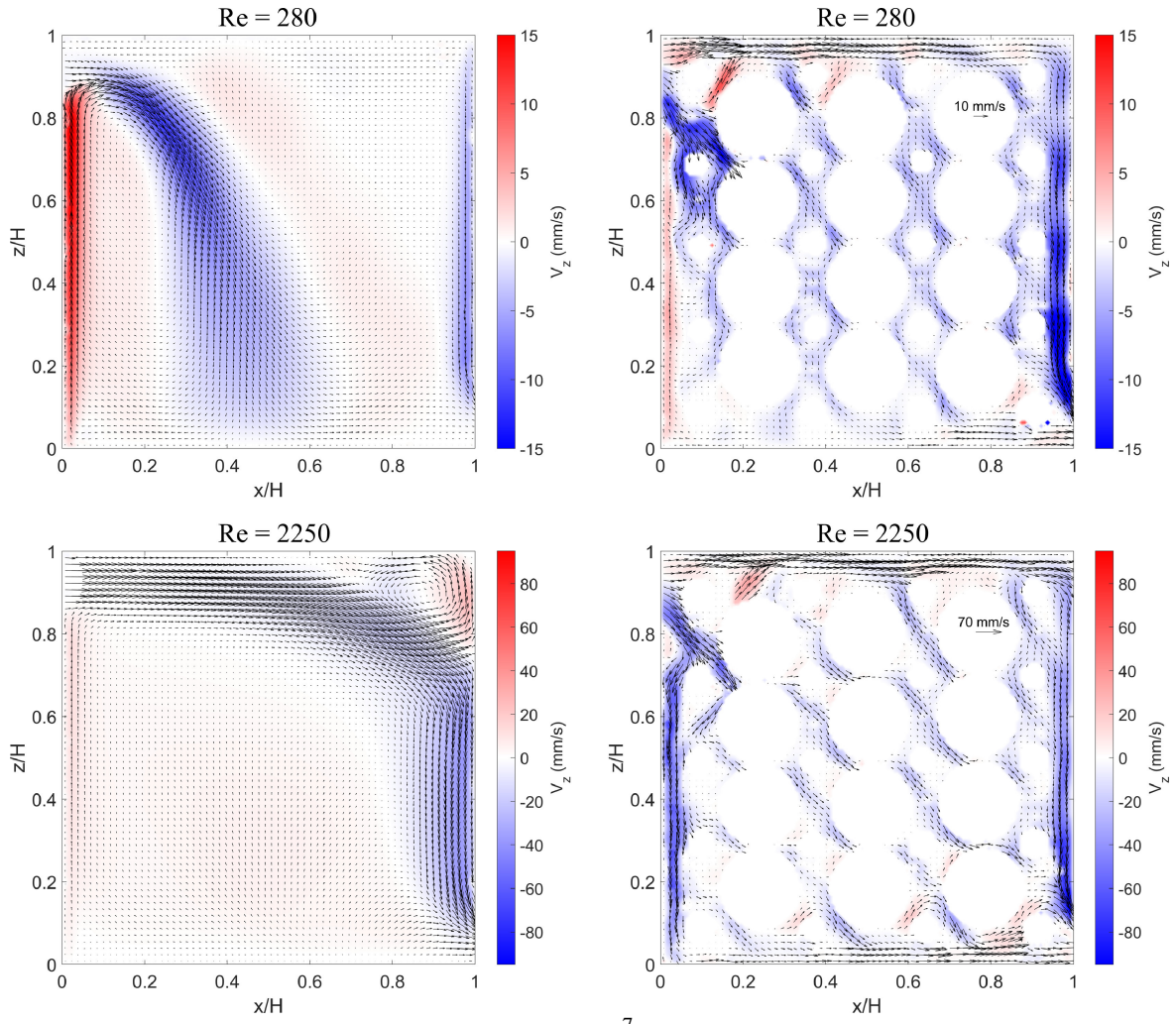


Fig. 4.3 Mean velocity fields at $Ra = 5.6 \times 10^7$ for the pure-fluid cavity (left) and the porous medium filled cavity (right) at $Re = 280$ (top) and $Re = 2250$ (bottom) in configuration A. The color map represents the vertical velocity component $v_z$.

However, as the Reynolds number increases, the forced convection gradually overcomes the natural convection such that a large portion of the cold inflow moves downward and comes in direct contact with the heating plate. This phenomenon causes a steep rise of Nusselt number with increasing Reynolds number. In contrast, in the pure-fluid cavity, the mechanism of heat removal and the flow pattern near the heating wall is qualitatively the same at low and high Reynolds numbers. The forced convection flow favors heat removal by aiding the natural convection flow, but the cold fluid never comes into direct contact with the heating wall. As the Reynolds number increases, the inflow moves more straight through the cavity and then impinges on the cold wall. The flow and heat transfer in similar configurations without porous media are discussed in more detail in [49,50,123].

### 4.3.2 Effect of Rayleigh and Reynolds numbers on flow and heat transfer

Fig. 4.4 shows the Nusselt number as a function of Rayleigh number for six different Reynolds numbers including Re = 0 (corresponding to pure natural convection) for the cavity filled with the porous medium. Natural convection data for a side-heated closed cavity filled with the same porous medium [135] is also included for comparison. A good agreement between the slope of the two natural convection curves is observed. The shift in the values is due to the different geometries of the hot/cold walls (with and without inflow/outflow ports) and thus different length scales used to define the Rayleigh and Nusselt numbers. First, it is observed that the mixed convection heat transfer is always higher than pure natural convection (Re = 0). This is due to introducing a cold fluid into the cavity which enhances the heat transfer from the heating plate to the fluid through a lowering of the bulk temperature. Second, it can be observed that at a constant Reynolds number Re > 0, the slope of the Nu-Ra curve is (nearly) zero at low Rayleigh numbers, and that this slope gradually increases with increasing Rayleigh number. This process also depends on the Reynolds number. The higher the Reynolds number, the later (in terms of Rayleigh number) the increase of the Nusselt number sets in and the smaller is the slope. In general, at higher Reynolds numbers and lower Rayleigh numbers (i.e. lower Ri), when forced convection is the dominant heat transfer regime, the Nusselt number becomes independent of the Rayleigh number and the scaling exponent $\alpha$ in $\mathrm{Nu} \sim \mathrm{Ra}^{\alpha}$ is zero. However, at lower Reynolds numbers and higher Rayleigh numbers (i.e. higher Ri), when natural convection is important, the value of the scaling exponent $\alpha$ increases. The highest scaling exponent is observed at the highest Rayleigh number and the lowest Reynolds number (i.e. the highest Ri) and is approximately 0.5.

Fig. 4.5 shows the Nusselt number as a function of Reynolds number at different Rayleigh numbers, along with the results for pure forced convection. The pure forced convection data points were obtained by rotating the cavity such that the heating plate is at the top and the cooling plate is at the bottom (see configuration C in Fig. 4.1b). The pure forced convection data points are fitted by the power-law

$$\mathrm{Nu_{FC}} = 0.836\,\mathrm{Re}^{0.610}\,, \tag{4.6}$$

which is shown as a solid line in Fig. 4.5. It is observed that at sufficiently high Reynolds numbers, the heat transfer rates for different Rayleigh numbers converge to the forced convection curve. This indicates that natural convection is negligible in this range of high Reynolds numbers and that the flow and heat transfer are fully dominated by forced convection. For the highest Rayleigh number, the heat transfer data start to branch away from the forced convection curve when the Reynolds number decreases below approximately Re = 1400. This is an indication of the onset of natural convection effects. The Reynolds number where branching

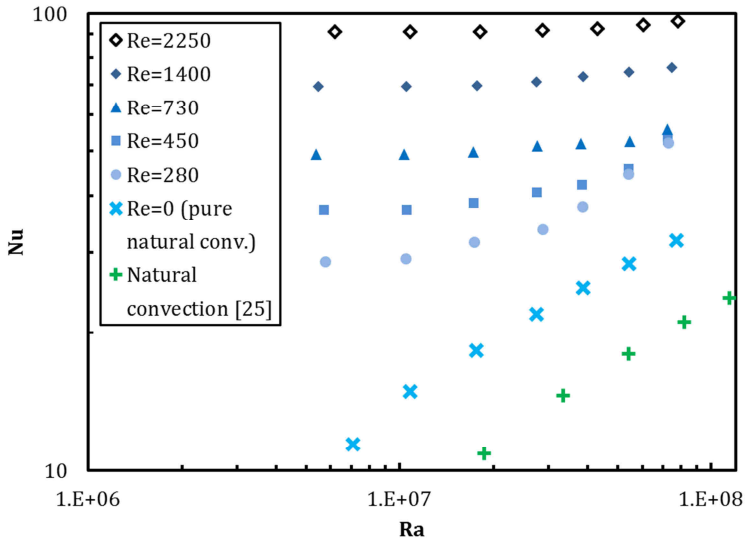


Fig. 4.4 Nu-Ra data for the porous medium filled cavity for different Reynolds numbers (configuration A). The crosses (×) pertain to the pure natural convection data for the same porous medium filled vented cavity with no inflow. The pluses (+) pertain to data for natural convection in a closed cavity filled with the same porous medium [135].

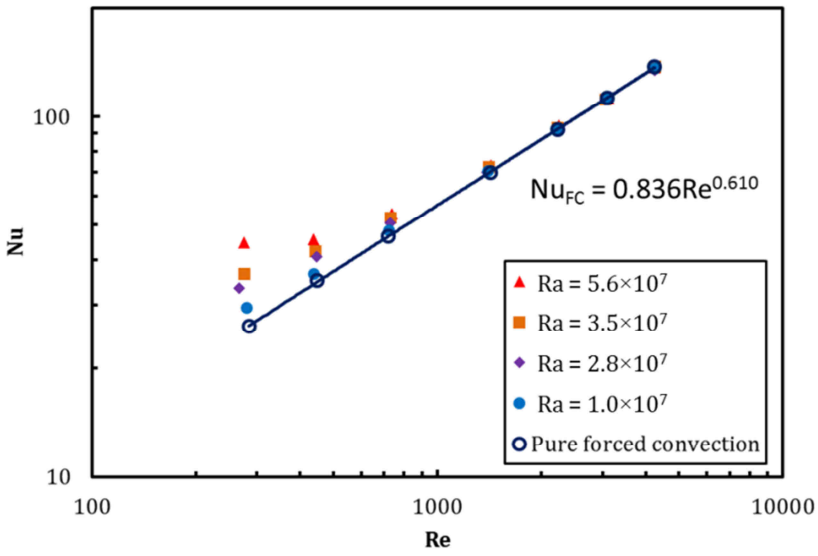


Fig. 4.5 Nu-Re data for the porous medium filled cavity for different Rayleigh numbers (configuration A). The solid line shows the power-law fit to the pure forced convection data, Eq. (4.6), for the same cavity.

first occurs increases with increasing Rayleigh number. It is observed that at the highest Rayleigh number (i.e. $Ra = 5.6 \times 10^7$) and the lowest Reynolds numbers, the Nusselt number becomes almost independent of Reynolds number such that the scaling exponent $\beta$ in $Nu \sim Re^{\beta}$ approaches zero. This is an indication of the dominance of natural convection over forced convection. Fig. 4.6 shows the mean velocity fields at low Reynolds number (Re = 280) for three different Rayleigh

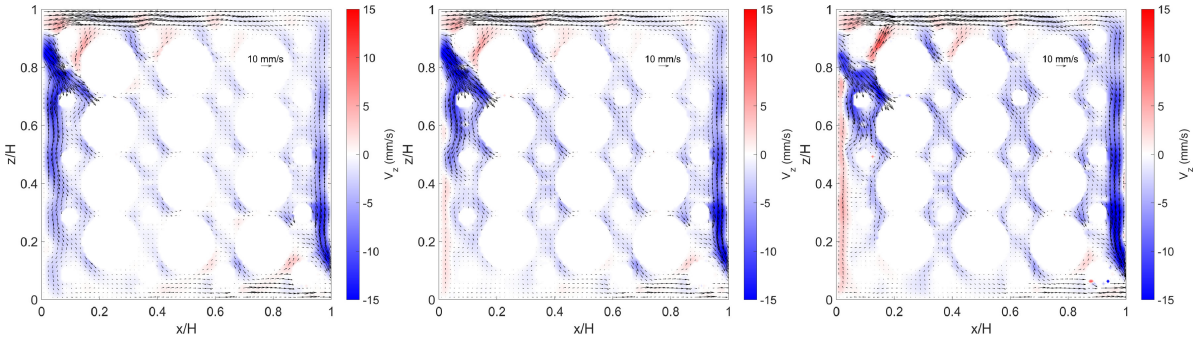


(a) Ri = 18.9 (b) Ri = 52.9 (c) Ri = 105.8

Fig. 4.6 Mean velocity fields at Re = 280 for (a) Ra = $1.0 \times 10^7$, (b) Ra = $2.8 \times 10^7$, and (c) Ra = $5.6 \times 10^7$ in configuration A.

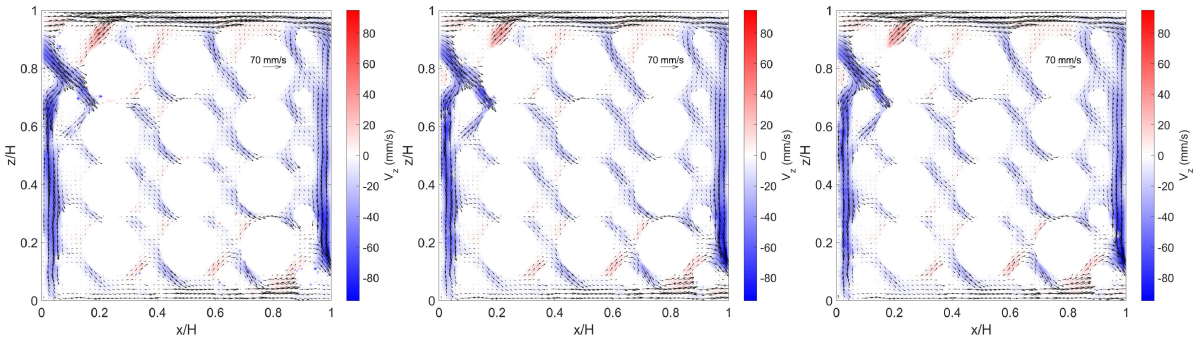


(a) Ri = 0.29 (b) Ri = 0.82 (c) Ri = 1.65

Fig. 4.7 Mean velocity fields at Re = 2250 for (a) Ra = $1.0 \times 10^7$, (b) Ra = $2.8 \times 10^7$ and (c) Ra = $5.6 \times 10^7$ in configuration A.

numbers. It is seen that at this low Reynolds number, increasing the Rayleigh number substantially changes the flow structure in the vicinity of the heating wall so that the upward natural convection flow gradually overcomes the imposed downward forced convection flow. This leads to an enhanced strength of natural convection at a fixed forced flow and therefore the Nusselt number increases with increasing Rayleigh number. On the other hand, Fig. 4.7 confirms that at high Reynolds numbers, forced convection fully dominates the flow structure and natural convection flow is completely suppressed, such that increasing the Rayleigh number has no influence on the flow field and the heat transfer. Fig. 4.8 shows the mean velocity fields at Ra = $3.5 \times 10^7$ for four different Reynolds numbers. It shows that by increasing Reynolds number, the downward forced convection flow overcomes the upward natural convection flow in the region near the heating wall. The flow field results show that for Re $\gtrsim$ 1400 the forced convection dominated regime is reached, such that a further increase of the Reynolds number (from 1400 to 2250) does not change the flow structure in the cavity. This is in agreement with the Nu-Re data in Fig. 4.5 which indicate that an

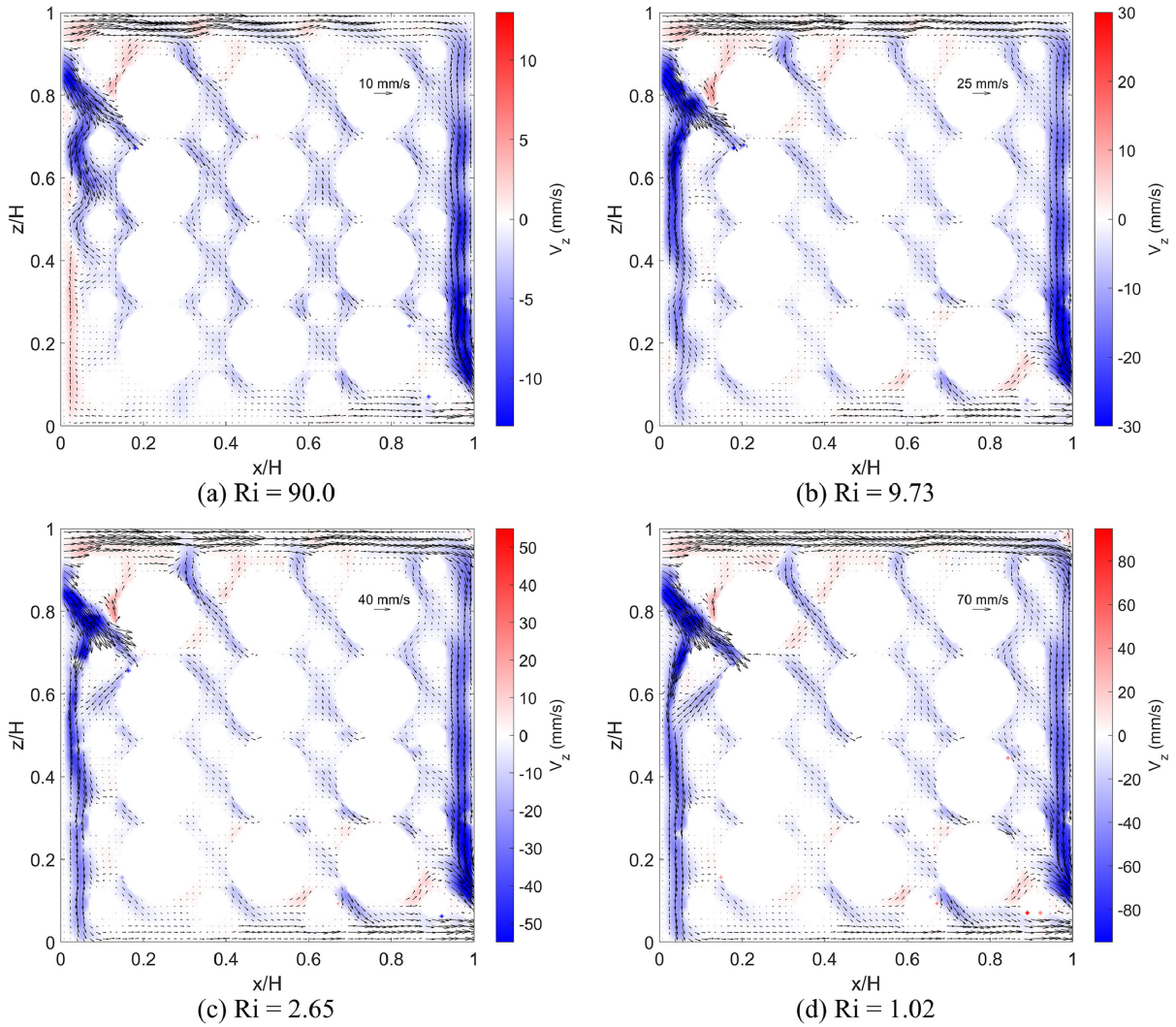


(a) Ri = 90.0 (b) Ri = 9.73

(c) Ri = 2.65 (d) Ri = 1.02

Fig. 4.8 Mean velocity fields at Ra = $3.5\times10^7$ for (a) Re = 240, (b) Re = 730, (c) Re = 1400, (d) Re = 2250 in configuration A.

asymptotic forced convection dominated regime is reached for Re ≳ 1400. Liquid Crystal Thermography (LCT) measurements were performed at the fixed Rayleigh number of Ra = $3.5\times10^7$ based on the effective temperature range of the used liquid crystals. Fig. 4.9 shows the resulting mean temperature fields for the same four Reynolds numbers as in Fig. 4.8. The temperature measurement results show that at the lowest Reynolds number, due to the opposing behavior of the forced flow and the presence of the spheres, the hot fluid is trapped in a recirculation zone near the heating wall leading to the formation of a high-temperature isolated region in the vicinity of the heating wall. Since the downward forced flow is not strong enough to overcome the upward natural convection flow, the interaction between the cold inflow and the heating wall is minimal. This explains the low slope of the

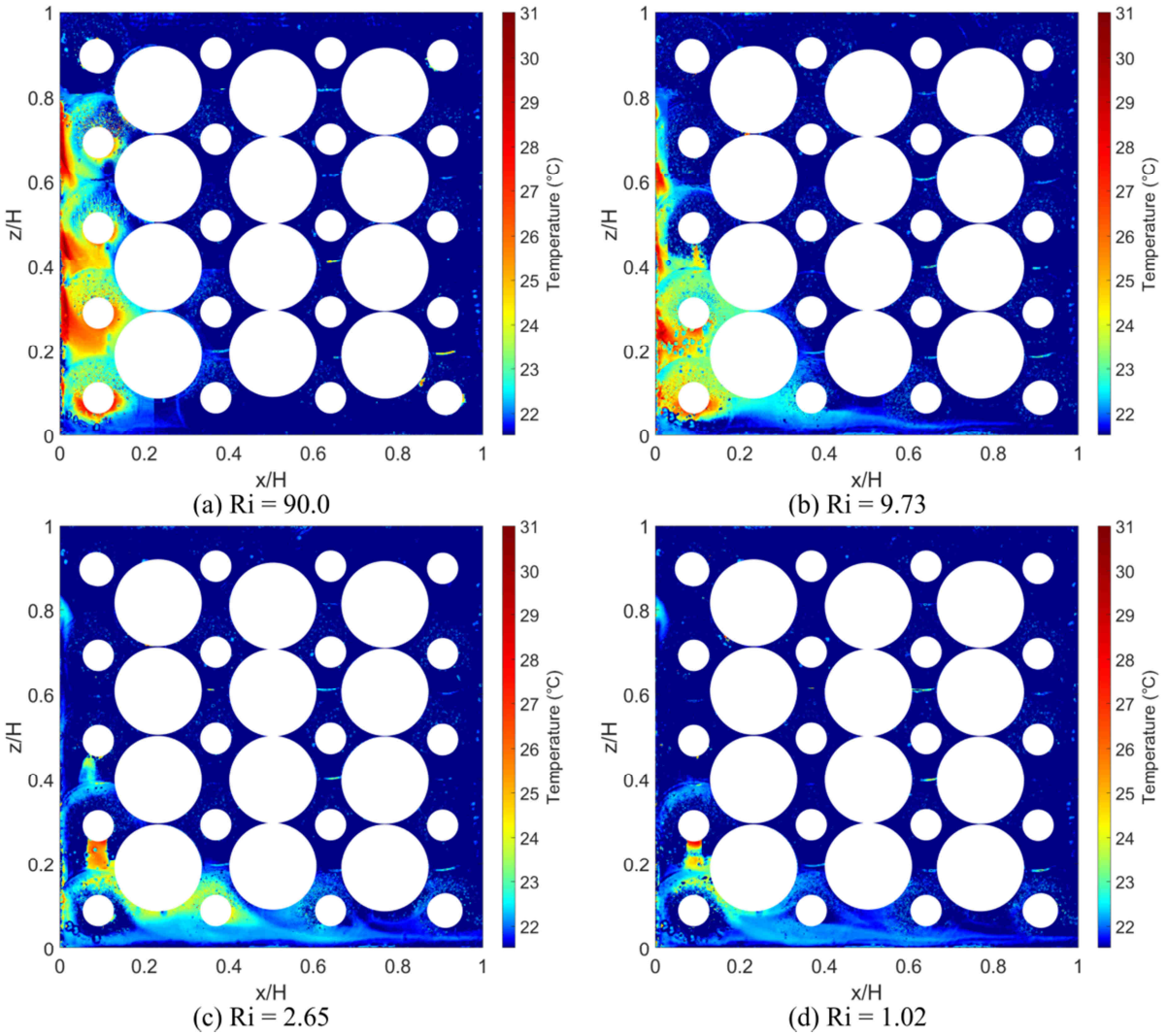


Fig. 4.9 Mean temperature fields at Ra = $3.5\times10^7$ for (a) Re = 240, (b) Re = 730, (c) Re = 1400, (d) Re = 2250 in configuration A.

Nu-Re curve in this regime, see Fig. 4.5. As the Reynolds number increases and the downward forced convection flow overcomes natural convection, a larger portion of the inflow moves downward along the heating wall and subsequently along the bottom wall. As a result, the cold inflow interacts more directly with the heating wall and carries away the heat toward the outlet. For Re $\gtrsim$ 1400, where forced convection dominates, it is observed that the cold inflow is in direct contact with the heating wall and the high-temperature region is driven away from the heating wall towards the bottom wall. This apparently leads to a higher sensitivity of the Nusselt number to variations in Reynolds number, and, as evidenced by the relatively large value of the scaling exponent in Eq. (4.6), the scaling exponent $\beta$ in Nu ~ $\mathrm{Re}^{\beta}$ becomes $\beta = 0.61$. The boundary condition values corresponding to the velocity and temperature fields in Fig. 4.8 and Fig. 4.9 are given in Table 4.1.

Table 4.1 The temperatures of the inflow, the cold wall, and the hot wall, and the bulk inlet velocities for the velocity and temperature fields shown in Figs. 4.8 and 4.9.

| Ra | Re | Ri | $T_c = T_{in}$ (°C) | $T_h$ (°C) | $u_{in}$ (mm/s) |
|---|---|---|---|---|---|
| $3.5 \times 10^7$ | 240 | 90.0 | 22.0 | 31.6 | 3.03 |
| $3.5 \times 10^7$ | 730 | 9.73 | 22.0 | 31.6 | 9.20 |
| $3.5 \times 10^7$ | 1400 | 2.65 | 22.0 | 31.6 | 17.6 |
| $3.5 \times 10^7$ | 2250 | 1.02 | 22.0 | 31.6 | 28.2 |

### 4.3.3 Effective scaling of Nusselt number

The results in Fig. 4.4 and Fig. 4.5 clearly imply that the Nusselt number is governed by the relative strength of natural and forced convection which can be represented by the Richardson number as discussed earlier in the introduction. Fig. 4.10 shows the ratio of the mixed convection heat transfer over the forced convection heat transfer (at the same Re) as a function of Richardson number for all measurements. The heat transfer data cover a wide range of Richardson numbers, i.e., $0.1 < \mathrm{Ri} < 100$. It is observed that the data collapse onto a single curve which can represent the mixed convection heat transfer behavior in this configuration. Fig. 4.10 shows that for $\mathrm{Ri} \lesssim 3$ the normalized Nusselt number is close to unity which indicates the dominance of forced convection over natural convection. This can be observed in the flow fields in Figs. 4.7, 4.8c, and 4.8d. The onset of natural convection effects corresponds to the point where the normalized heat transfer starts to deviate from unity at $\mathrm{Ri} \approx 3$. That is when natural convection flow emerges at the heating wall and by further increasing the Richardson number, it starts to take over the forced convection flow, see Figs. 4.6, 4.8a, and 4.8b. At $\mathrm{Ri} \gtrsim 3$ the increasing strength of the natural convection results in an enhanced heat transfer with respect to the pure forced convection. A curve is fitted to the data points considering the constraints at the two extremes: (i) Nu being independent of Ra for $\mathrm{Ri} \to 0$, and (ii) Nu being independent of Re for $\mathrm{Ri} \to \infty$. The fitted curve is shown as a solid (green) line in Fig. 4.10 and is given by

$$\frac{\mathrm{Nu}}{\mathrm{Nu_{FC}}} = (1 + 0.0375\ \mathrm{Ri})^{0.305}. \tag{4.7}$$

Substituting the power-law relation obtained for the forced convection heat transfer, Eq. (4.6), into Eq. (4.7) yields the following correlation for the Nusselt

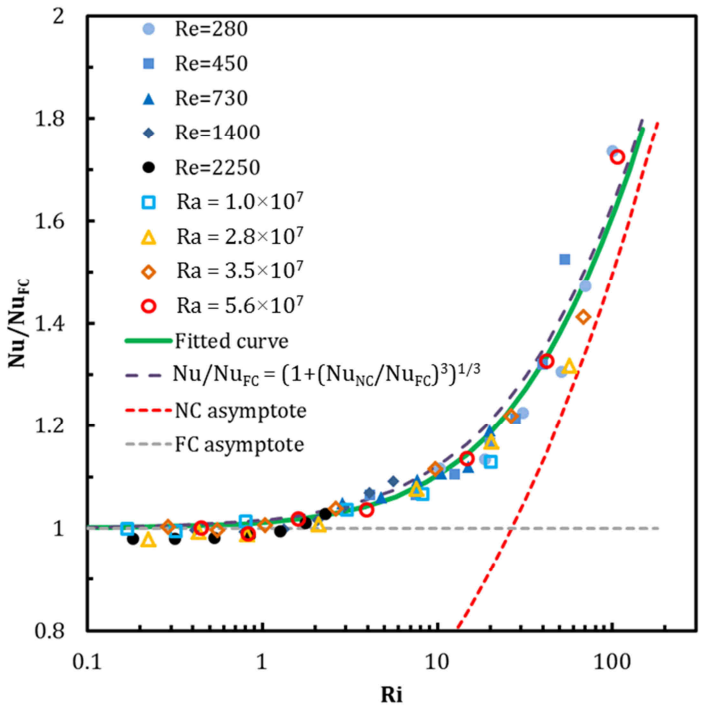


Fig. 4.10 Nusselt number, Nu, normalized with the pure forced convection Nusselt number, $Nu_{FC}$, as a function of Richardson number, Ri (configuration A). The solid line shows the curve that was fitted to the data according to Eq. (4.7). The dashed line pertains to the correlation in Eq. (4.9).

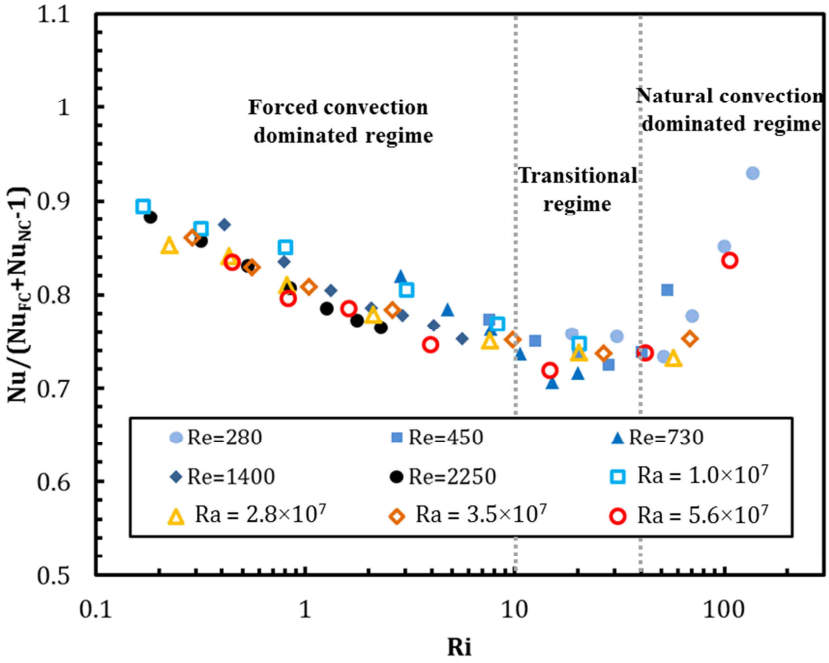


Fig. 4.11 Effective Nusselt number, $Nu_{eff}$ as a function of Richardson number, Ri in configuration A.

number as a function of Reynolds and Rayleigh number for low-conductivity spheres ($k_s/k_f \leq 1$)

$$\mathrm{Nu} = 0.836\mathrm{Re}^{0.610}\left(1 + 0.00556\frac{\mathrm{Ra}}{\mathrm{Re}^2}\right)^{0.305}. \tag{4.8}$$

In this correlation, for $\mathrm{Ri} \to 0$, the forced convection power-law function of Reynolds number, Eq. (4.6), is retrieved. Also, for $\mathrm{Ri} \to \infty$, the Nusselt number scales with $\mathrm{Ra}^{0.305}$ which is in agreement with classical natural convection scaling in cavities without porous medium [30]. As discussed in [112,135], natural convection scaling in porous media behaves very similar to the pure-fluid natural convection scaling at sufficiently high Rayleigh numbers. Both pure forced convection and pure natural convection asymptotes are shown in Fig. 4.10 as well.
Several theoretical studies of mixed convection along vertical flat plates have proposed correlations in the form of $\mathrm{Nu}^n = \mathrm{Nu_{FC}}^n + \mathrm{Nu_{NC}}^n$ [136,137], where $\mathrm{Nu_{FC}}$ and $\mathrm{Nu_{NC}}$ are the forced convection and the natural convection asymptotes for $\mathrm{Ri} \to 0$ and $\mathrm{Ri} \to \infty$, respectively. Different values for n have been proposed: n = 2 [138] , n = 3 [137,139], and n = 4 [136]. We found that for n = 3, the correlation agrees very well with our experimental data. The resulting correlation

$$\frac{\mathrm{Nu}}{\mathrm{Nu_{FC}}} = \sqrt[3]{1 + \left(\frac{\mathrm{Nu_{NC}}}{\mathrm{Nu_{FC}}}\right)^3}. \tag{4.9}$$

is plotted in Fig. 4.10 as a dashed line.
Another way of presenting the heat transfer data is to normalize the mixed convection heat transfer as follows

$$\mathrm{Nu_{eff}}(\mathrm{Re}, \mathrm{Ra}) = \frac{\mathrm{Nu\ (Ra,Re)}}{\mathrm{Nu_{NC}(Ra)} + \mathrm{Nu_{FC}(Re)} - 1}. \tag{4.10}$$

$\mathrm{Nu_{eff}}$ is the effective Nusselt number and is used to quantify the strength of mixed convection heat transfer Nu (Ra, Re) with respect to the sum of the pure natural convection heat transfer at that specific Rayleigh number $\mathrm{Nu_{NC}}$ (Ra) and the pure forced convection heat transfer at that specific Reynolds number $\mathrm{Nu_{FC}}$ (Re). Since the conductive heat transfer is included in both $\mathrm{Nu_{NC}}$ and $\mathrm{Nu_{FC}}$, 1 is subtracted from the sum to make sure that conduction is only considered once in the denominator. Fig. 4.11 shows the values of $\mathrm{Nu_{eff}}$ as a function of Richardson number for all heat transfer data points. It is observed that $\mathrm{Nu_{eff}} < 1$ for the entire range of Richardson numbers considered in this study. For $\mathrm{Ri} < 10$, the effective Nusselt number decreases with increasing Richardson number, which means that the enhancement of buoyancy-induced heat transfer is not as much as what it would be in the pure natural convection case. This is due to the fact that natural

convection is mostly suppressed by the strong forced convection in this range of Ri numbers. In this regime, forced convection dominates and the heat transfer is determined by the Reynolds number since the heat transfer reduction caused by decreasing the Reynolds number is stronger than the heat transfer enhancement caused by increasing the Rayleigh number. The decrease of the effective Nusselt number continues until a minimum is reached in the intermediate range $10 < Ri < 40$. Maximum competition between natural and forced convection occurs in this region which leads to the lowest effective Nusselt number. In this transitional regime, forced and natural convection have comparable strength acting opposite each other, and therefore the effective heat transfer is insensitive to changes in Richardson number. For $Ri > 40$, the effective Nusselt number starts to increase with increasing Richardson number. In this regime, the Rayleigh number determines the heat transfer since the effect of increasing Rayleigh number is stronger than that of decreasing Reynolds number. The shape of the $Nu_{eff}$ -Ri curve illustrates that in the studied configuration A (see Fig. 4.1), natural convection flow and forced convection flow work against each other as was readily seen in the flow fields in Fig. 4.6 and Fig. 4.8. In general, the shape of the $Nu_{eff}$ -Ri curve enables us to identify three different flow and heat transfer regimes depending on Richardson number, namely a forced convection dominated regime ($Ri < 10$), a natural convection dominated regime ($Ri > 40$), and a transitional regime ($10 < Ri < 40$). These three regimes are shown in Fig. 4.11.

### 4.3.4 Effect of Configuration on heat transfer

Although the majority of the experiments were conducted in configuration A, experiments were also performed in configuration B which has the inlet at the bottom of the heating wall and the outlet at the top of the cooling wall, see Fig. 4.1b. The Nu-Re data for the two configurations at two different Rayleigh numbers are compared in Fig. 4.12. The heat transfer behavior as a function of the Reynolds number and the Rayleigh number is qualitatively the same for both configurations, in the sense that there is 1) a general trend of increasing Nusselt number with increasing Rayleigh and Reynolds numbers, 2) Nusselt number is independent of Rayleigh number at high Reynolds numbers, and 3) Nusselt number only weakly depends on Reynolds number at low Reynolds numbers. The graph shows that at sufficiently high Reynolds numbers ($Re \gtrsim 2000$), the Nusselt numbers for both configurations converge to the forced convection curve, Eq. (4.6). As the Reynolds number decreases, the Nusselt number values for configuration B start to deviate from the forced convection curve and this deviation occurs at a higher Reynolds number than in configuration A. This means that natural convection effects emerge earlier in configuration B and are clearly noticeable at Reynolds numbers as high as $Re = 1400$. At lower Reynolds

numbers, where natural convection becomes more important, the configuration has a significant effect on the heat transfer, and the Nusselt numbers for configuration B are considerably higher than those for configuration A. This is most likely because in configuration B when natural convection is strong, a large portion of the cold incoming flow is entrained toward the heating wall by the upward buoyancy-induced natural convection flow. For Re $\gtrsim$ 2000 natural convection flow is suppressed by the intense forced convection flow, thus the opposing and assisting behavior near the heating wall for Configurations A and B, respectively, have no influence on the flow structure and subsequently the heat transfer. In general, higher Nusselt numbers were measured for configuration B which implies that this configuration can extract more heat from the heating source and has a better heat removal performance compared to configuration A.

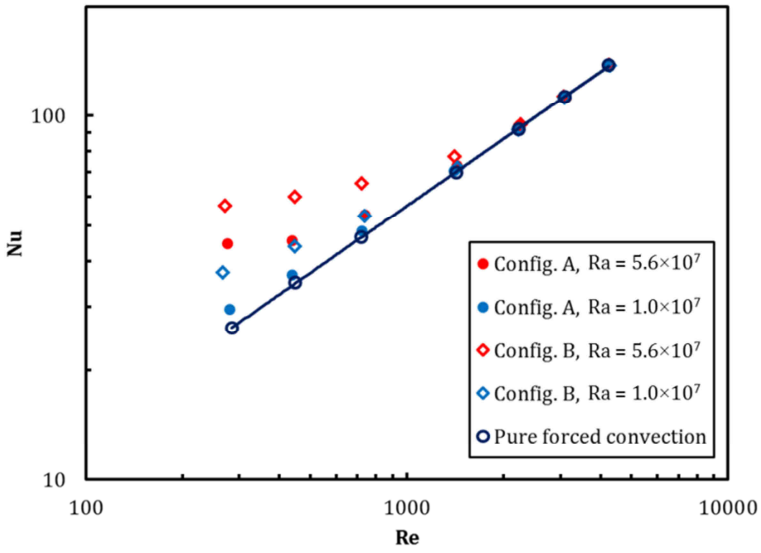


Fig. 4.12 Nu-Re data for configurations A and B at two different Rayleigh numbers.

### 4.3.5 Heat removal splitting behavior

It is important to investigate how the heat from the heating wall is removed from the cavity. Part of the heat is transferred to the cooling wall which is kept at a low temperature equal to the inflow temperature. The remaining part is carried away by the flow and exits the cavity through the outlet. In this section, we study how the heat generated at the heating wall is distributed over these two heat removal pathways for configuration A. For this, we use the ratio $Q_{flow}/Q_{total}$ as defined in Eq. (4.5). Fig. 4.13 and Fig. 4.14 show $Q_{flow}/Q_{total}$ values as a function of Reynolds number for different Rayleigh numbers, and as a function of Rayleigh number for different Reynolds numbers, respectively. When shown as a function of Richardson number in Fig. 4.15, the results indicate a consistent behavior with a

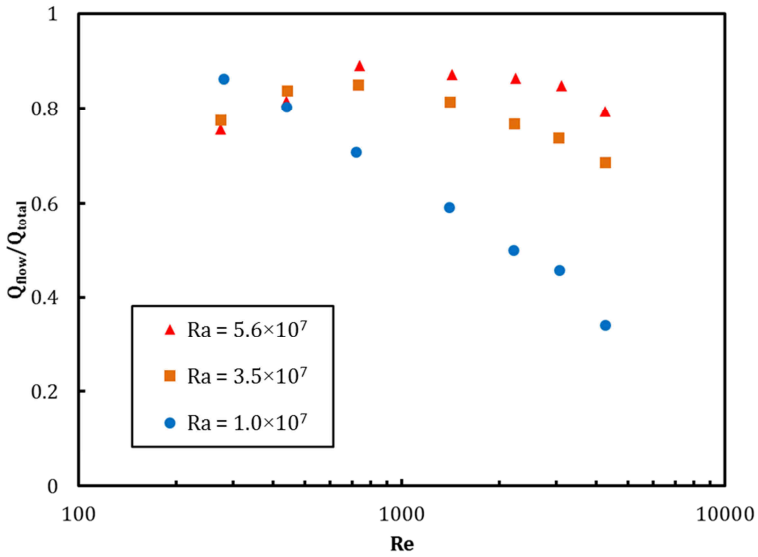


Fig. 4.13 The ratio $Q_{flow}/Q_{total}$ as a function of Reynolds number for different Rayleigh numbers in configuration A.

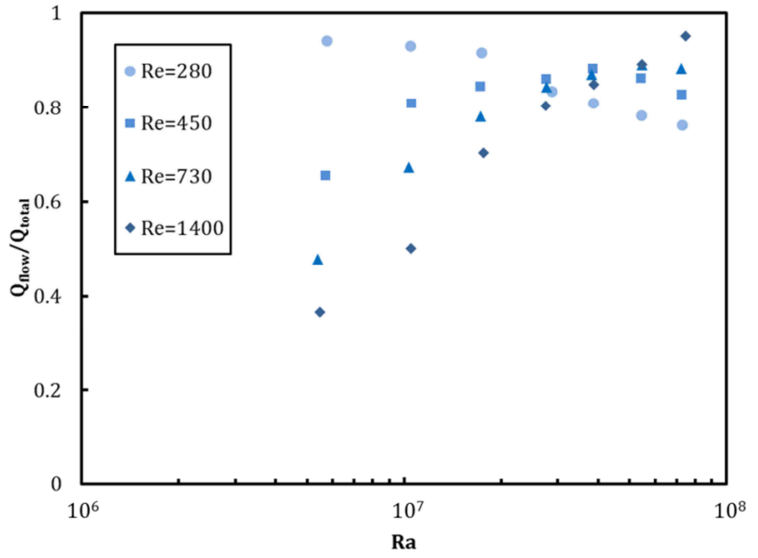


Fig. 4.14 The ratio $Q_{flow}/Q_{total}$ as a function of Rayleigh number for different Reynolds numbers in configuration A.

maximum at Ri ≈ 10. For Ri > 10 where natural convection flow is present at the heating wall, increasing the Richardson number (i.e. increasing Ra or decreasing Re) leads to a stronger upward natural convection flow overcoming the downward motion of the forced convection flow along the heating wall. This causes a larger portion of the forced inflow to move directly along the top and cold walls of the cavity leading to an increased heat transfer at the cold wall and, consequently, a reduced value of $Q_{flow}/Q_{total}$. This can be observed clearly in the mean velocity fields shown in Fig. 4.6. On the other hand, for Ri < 10 where forced convection dominates the flow structure, decreasing the Richardson number (i.e. increasing Re or decreasing Ra) leads to a decrease in $Q_{flow}/Q_{total}$. In the forced convection

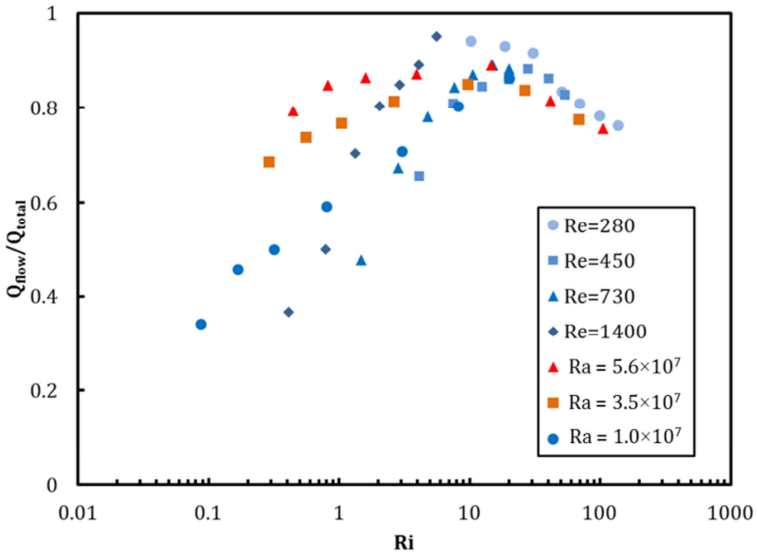


Fig. 4.15 The ratio $Q_{flow}/Q_{total}$ as a function of Richardson number for all experiments (configuration A).

dominated regime the inflow moves along both the hot/bottom walls and the top/cold walls. In this regime, as the Reynolds number increases, larger inertial forces cause the inflow to move more horizontally through the cavity and impinge on the cold wall which leads to a higher heat transfer at the cold wall and thus lower $Q_{flow}/Q_{total}$ (see Fig. 4.13). Moreover, increasing the Rayleigh number in the forced convection dominated regime causes a higher heat transport along the hot/bottom walls and therefore an increased value of $Q_{flow}/Q_{total}$ ratio (see Fig. 4.14). In general, the outflow is the main heat removal pathway at the intermediate range of Richardson numbers ($Ri \approx 10$). However, as either natural convection or forced convection dominates, the cooling wall becomes a major heat removal pathway in this mixed convection configuration.

## 4.4 Conclusions

Mixed convection in a vented cavity (with an inlet at the top of the heating wall and an outlet at the bottom of the cooling wall) filled with a porous medium consisting of relatively large ($d/L = 0.20$) low-conductivity ($k_s/k_f \leq 1$) spheres was experimentally studied. Nusselt numbers, as well as velocity and temperature fields, were measured for a wide range of Reynolds and Rayleigh numbers resulting in a Richardson number variation between 0.1 to 100. For comparison, a pure-fluid cavity without porous medium and a second configuration with the inlet at the bottom of the heating wall and the outlet at the top of the cooling wall (configuration B) were also considered. It was found that at high Reynolds numbers, the Nusselt number is considerably higher for the cavity with porous medium as compared to the pure-fluid cavity due to a portion of the cold inflow

directing toward the heating wall. For the cavity filled with spheres, a general trend of increasing Nusselt number with increasing Rayleigh and Reynolds numbers was observed. The Nusselt number normalized with the pure forced convection heat transfer depends only on the Richardson number which leads to the following correlation for the Nusselt number as a function of Reynolds and Rayleigh numbers (for $240 < Re < 4250$, $6 \times 10^6 < Ra < 7 \times 10^7$ and $0.1 < Ri < 100$)

$$Nu = 0.836Re^{0.610}(1 + 0.00556\frac{Ra}{Re^2})^{0.305}.$$

Based on the velocity fields and the behavior of the effective Nusselt number (which is defined as the Nusselt number normalized with the sum of pure natural and forced convection), three flow and heat transfer regimes can be identified depending on Richardson number: a forced convection dominated regime for $Ri < 10$; a transitional regime for $10 < Ri < 40$; and a natural convection dominated regime for $Ri > 40$. In the forced convection dominated regime, natural convection flow is suppressed and both flow and heat transfer are very similar to those for the pure forced convection, and the Nusselt number scales with Reynolds number as $Nu \sim Re^{0.610}$, and is independent of the Rayleigh number. In the transitional regime, natural convection and forced convection flow are of comparable strength competing against each other which leads to a minimum effective Nusselt number and a maximum heat removal contribution by the outflow. In the natural convection dominated regime, the upward buoyancy-driven flow dominates and prevents the entrainment of the cold forced flow toward the heating wall. In that case, the Nusselt number is mainly determined by the Rayleigh number and only weakly depends on the Reynolds number. In configuration B, higher Nusselt numbers were measured in the natural convection dominated and transitional regimes which implies a better heat removal performance of this configuration.

# Chapter 5

## Conclusions and outlook

## 5.1 Natural and mixed convection in coarse-grained porous media

This investigation has experimentally studied bottom-heated natural convection, side-heated natural convection, and vented mixed convection flow and heat transfer in cavities filled with coarse-grained porous media consisting of packed spheres. Nusselt numbers were measured for a wide range of Rayleigh and Reynolds numbers and for various sphere conductivities, sphere sizes, and sphere packings. The use of water and hydrogel spheres for refractive index matching enabled us to perform optical measurement techniques (Particle Image Velocimetry and Liquid Crystal Thermography) in natural and mixed convection flows for the first time. Using these techniques, velocity and temperature fields inside the pores at the entire porous medium domain were obtained. In the three studied cases, the results have been compared with the equivalent pure-fluid cavities (i.e. cavities without the porous medium).

A general observation is that, unlike fine-grained porous media, the local geometrical features of a coarse-grained porous material (such as local porosity and pore structure) have a large impact on local flow and heat transfer, which is reflected in overall features such as the global Nusselt number. The ratio between the size of typical flow features (such as thermal plumes and thermal boundary layers) and the typical pore size is found to play a decisive role in the impact of the packing on flow and heat transfer.

In bottom-heated natural convection, it was observed that the heat transfer reduction due to the presence of coarse-grained porous media vanishes at sufficiently high Rayleigh numbers, when the flow and thermal length scales become small enough (smaller than approximately 1/20 times the sphere diameter) to no longer be obstructed by the presence of coarse-grained porous media. As a result, the overall heat transfer asymptotically approaches that for the pure-fluid cavity when the Rayleigh number increases. On the other hand, in side-heated natural convection, the boundary layers along the hot and cold side walls are always being hindered and obstructed by the layers of the spheres touching the side walls, even at high Rayleigh numbers. As a result of this obstruction and the resulting deflection and penetration of the boundary layer flow into the inner pores, the temperature distribution is altered and the overall heat transfer remains smaller than that of the pure-fluid cavity even at the highest measured Rayleigh numbers. Only when a sufficiently large gap is created between the isothermal side walls and the porous structure, the Nusselt number values reach those for the pure-fluid cavity. We report on a transition from Darcy to non-Darcy behavior at increasing Rayleigh number and increasing sphere size. A new Nusselt number correlation is introduced for the non-Darcy regime which includes the strong effect of the porous medium conductivity on the overall heat transfer.

In the vented mixed convection, the presence of the coarse-grained porous medium reduces the heat transfer (similar to the natural convection cases) at low Reynolds numbers, whereas at high Reynolds numbers the heat transfer becomes significantly higher than that for the pure-fluid cavity. The porous medium directs a portion of the inflow towards the hot wall when the strength of the forced flow is increased in competition with the natural convection flow. The flow field results show how the interaction between the forced flow, the buoyancy induced flow and the grains determines the overall heat transfer and the flow structure. Three flow and heat transfer regimes are identified as a function of Richardson number: natural convection dominated regime, forced convection dominated regime, and a transitional regime. The scaling of Nusselt number with Reynolds number and Rayleigh number has been discussed and compared with the pure natural convection and pure forced convection cases. Based on the experimental data, a Nusselt number correlation has been derived which expresses Nusselt number as a function of Reynolds and Rayleigh numbers.

## 5.2 Relevance for understanding and modeling the blast furnace hearth

The driving force behind this study was the interest in flow and heat transfer in a blast furnace hearth, which is a mixed convection flow of high temperature molten metal in a packing of large and irregularly shaped coke particles of varying sizes. The experiments in this study, however, have been performed in generic, simplified model geometries using water as the working fluid to provide fundamental insight into the underlying physics of natural and mixed convection flow and heat transfer in coarse-grained porous media. Therefore, the experimental results cannot be used directly to design and optimize the blast furnace hearth. However, the detailed experimental data on flow, temperature, and heat transfer obtained in this investigation have been used to validate computational modeling approaches developed in the modeling activities within this project [140]. These improved and experimentally validated computational models may then be used by the industrial partner in the project, to enhance the understanding of the factors influencing the hearth process and to optimize the flow and heat transfer towards the improved protection of the hearth refractory wall. The experimental data will also be used by the steelmaking industry to validate their engineering-type computational models.

Although the experiments were carried out in simplified water models, the results capture some relevant physics of the transport phenomena in the blast furnace hearth and are useful on their own in the understanding of the fluid flow and heat transfer processes and hot spot formation in the hearth. The following conclusions can be drawn from the analysis of the experimental data.

- At sufficiently high Rayleigh numbers the global heat transfer characteristics in coarse-grained porous media are very similar to those in the absence of a porous medium. Therefore, since the typical Rayleigh numbers in the blast furnace hearth are very high ($Ra \approx 10^{11}$), engineers and researchers in industry might consider modeling the blast furnace as a system without porous medium. However, our experimental results in coarse-grained porous media show that the details of local flow velocity and temperature distributions are totally different from the pure-fluid cavity. This is of particular importance in studying local phenomena such as the formation of hot spots in the blast furnaces hearth. The concluding remark is that the presence of the coarse-grained porous medium in the hearth may be ignored when the interest is in global heat transfer characteristics, but should not be overlooked when addressing local phenomena.

- At sufficiently high Rayleigh numbers, where the flow and thermal length scales become sufficiently smaller than the pore length scales, the flow penetrates into the pores with high velocities and without being obstructed by the presence of the coarse-grained porous medium. The increased velocities lead to an enhanced strength of thermal advection compared to thermal diffusion. As a result, the hot flow directly impinges on the opposite wall with a high temperature since the heat does not have enough time to diffuse. Since the flow in the blast furnace hearth is already in the high Rayleigh number asymptotic regime, this phenomenon can obviously lead to hot spot formation on the refractory walls containing the hearth.

- It was observed that in side-heated natural convection, although the overall heat transfer is lower for the cavity filled with the coarse-grained porous medium compared to the pure-fluid cavity, the local heat transfer at the cold and hot walls can be significantly higher than that of the corresponding pure-fluid cavity. In other words, the presence of a coarse-grained porous medium causes strong non-uniformities in the local wall heat transfer. These local heat transfer non-uniformities may lead to the formation of hot-spots which have severe consequences in lowering the lifespan of the blast furnace refractory walls.

- A transition from Darcy to non-Darcy behavior was observed when increasing the Rayleigh number and the pore size. It was concluded that the flow in the blast furnace hearth, which is filled with large grains and has very high Rayleigh numbers ($Ra \approx 10^{11}$), is in the non-Darcy regime.

Therefore, it is not recommended to use Darcy-based simulation models to predict the flow and heat transfer in the blast furnace hearth. The models need to include the non-Darcy effects and the effects of the coarse-grained porous medium.

- It was observed that the mixed convection flow and heat transfer in coarse-grained porous media is mainly determined by the interaction between natural convection flow and forced convection flow in the higher-porosity region between the active walls and the porous structure. In the blast furnace hearth, if the taphole is placed at the top of the hearth and natural convection cooling is strong enough, the downward-directed natural convection flow can prevent the hot incoming flow to get in direct contact with the walls of the hearth.

## 5.3 Relevance for other application fields

### 5.3.1 Food industry

The natural and mixed convection configurations studied in this investigation are commonly used for cooling purposes in the food industry. Examples are cold rooms and refrigeration equipment loaded with stacks of food products. The food products can have spherical shape such as many fruits and some vegetable, or cuboid and cylindrical shapes such as food packages and cans. With the walls of the container exchanging heat with the outside, natural convection flow emerges. Furthermore, for the cooling of horticultural products, it is very common that a cold air flow is forced through the stack of food products in the container. In all these natural, mixed, and forced convection cooling situations, the local temperature distribution near individual products is of great importance. Food products that are exposed to warmer fluid are more vulnerable to quality degradation and spoilage. The results of this investigation give a first impression of the fluid temperature distribution in typical natural convection configurations and also show how introducing and increasing the forced convection cold inflow can enhance the temperature uniformity and heat transfer.

The bottom-heated natural convection results presented in this thesis are also relevant to the understanding of heating processes in the food industry, such as thermal processing and cooking of canned fruits, vegetables, and grains.

### 5.3.2 Indoor air-conditioning

The results of this investigation can indirectly improve the understanding of indoor heating, cooling, and ventilation. We have considered cases without ventilation (pure natural convection) and with ventilation (mixed convection). We have

provided the flow and temperature distributions for the empty enclosures as well as the enclosures filled with relatively large objects which can mimic a room filled with furniture and appliances. The results indicate that when a room is filled with multiple objects and obstacles, the flow and temperature distribution might significantly be altered. Moreover, we have examined two different ventilation configurations and found the one that has better heat removal performance. We also identified how the heat generated at one wall is distributed over two heat removal pathways: the isothermal cooled wall and the outflow.

## 5.4 Research Opportunities

### 5.4.1 Applicability of refractive index matching in thermally-driven flows

In this investigation, the idea of using water and hydrogel beads to create a refractive index matched porous medium that is not very sensitive to temperature variations was presented. This enabled us to use optical techniques, such as PIV and LCT, to study natural and mixed convection flows in porous media. Using this idea, highly-resolved velocity and temperature fields for natural and mixed convection in porous media were measured for the first time. This experimental innovation can open a new direction in studying natural and mixed convection flows in porous media, both in science and industry. Industries dealing with natural and forced convection in packed bed-like systems (chemical industry, oil producing industry, food industry, steelmaking industry, etc.) can use this technique in their R&D to experimentally investigate the flow and thermal phenomena in water models and to validate their developed engineering simulation tools. The industrial partner of this project, Tata Steel Europe, is currently using this experimental technique in its R&D laboratories to mimic the flow and heat transfer processes in the blast furnace hearth.

### 5.4.2 Non-monodisperse and non-spherical objects

This study focused on packed beds of monodisperse spherical particles. However, in most real applications this is not the case. For example, in the blast furnace hearth, the porous medium consists of coke particles with a range of sizes (approximately from 20 to 100 mm) and with non-spherical, irregular shapes. In refrigerating equipment in the food industry, the fruits and vegetables can have non-spherical shapes and the packages have mostly cylindrical or cuboidal shapes. Also, in indoor building air-conditioning and electronics cooling, there are obstacles of different shapes and sizes. In general, the results of this investigation can qualitatively be extended and used for understanding the natural and mixed convection flow in packed beds of non-monodisperse and non-spherical particles.

However, quantitative differences are expected to exist due to the change of the pore length scale and the different positioning of particles with respect to the walls. A packed bed of monodisperse particles with a non-spherical shape will lead to a different pore length scale distribution. The results of this investigation showed that for smaller spheres the asymptotic regime and the non-Darcy flow regime are reached at a higher Rayleigh number. In a packed bed of non-monodisperse particles, a range of pore length scales are present. In this case, it is presumed that the smallest pore length scale would determine the flow and heat transfer in the porous medium. To verify these speculations more research should be carried out to characterize the Nusselt number scaling rules and to fully understand the natural convection flow in packed beds of non-monodispersed and non-spherical particles.

### 5.4.3 Liquid metal as working fluid

To make the experimental results more relevant for understanding the actual liquid metal flow in the hearth of the blast furnace, it would be ideal to use a liquid metal as a working fluid rather than water. In fluids with Pr = O(1) such as water and air, the velocity and thermal boundary layers have similar thicknesses. However, liquid metals have low Prandtl numbers Pr = $O(10^{-2})$ which lead to much thicker thermal boundary layer compared to velocity boundary layer. By using a liquid metal as the working fluid, it would be possible to mimic the proper dynamics of natural and mixed convection flow associated with a dissimilar thickness of the velocity and temperature boundary layers. The main disadvantage of liquid metals is that they are not transparent and thus the optical measurement techniques such as PIV cannot be applied to measure the desired flow fields.

In this PhD project, it was attempted to perform X-ray particle tracking in galinstan in order to obtain quantitative and local information on the flow of a liquid metal. Galinstan is a commercially-available liquid metal alloy of gallium, indium, and tin. Galinstan was used because it is in the liquid state at room temperature (melting point at -19 °C), it has a low Prandtl number (Pr = 0.043), and it is relatively less toxic. The aim was to study natural convection flow of galinstan by using X-ray particle tracking. To achieve this goal, a quasi-two-dimensional test cavity containing a number of cylindrical obstacles was designed and built. Also, ~ 2 mm almost-neutrally-buoyant particles with a tungsten core were made. These particles were visualized in the galinstan-filled cavity using X-ray imaging. However, the particles did not follow the low-velocity natural convection flow in galinstan and were stuck to the solid surfaces. It turned out that galinstan always contains/develops some amount of gallium oxide which is very sticky and accumulates on solid surfaces. This makes the low-velocity X-ray particle tracking in galinstan very difficult and almost impossible, especially when there are multiple solid surfaces involved.

As a future research opportunity, it is proposed to use Ultrasound Doppler Velocimetry (UDV) technique to measure natural convection velocities in opaque liquid metals. In this technique, an ultrasound pulse is emitted from a transducer and travels along a measurement line into the liquid. The pulse hits the micro-particles suspended in the liquid metal and part of the ultrasound energy is reflected back to the transducer. The time delay between the emission and the reception determines the spatial position of a micro-particle from the transducer [141]. The velocity is obtained by detecting the Doppler shift of the reflected ultrasound wave [142]. This technique has the ability to obtain velocity profiles as a function of time in opaque liquids in a non-intrusive way. The main advantage of UDV over the particle tracking technique that we explored is that it does not need large O (1 mm) tracer particles, and even natural impurities in a liquid metal such as oxides can act as reflecting tracer particles. Therefore, UDV is the best choice to measure low-velocity natural convection flow fields in a liquid metal.

# References


[1] M. Chakkingal, S. Kenjereš, I. Ataei-Dadavi, M.J. Tummers, C.R. Kleijn, Numerical analysis of natural convection with conjugate heat transfer in coarse-grained porous media, Int. J. Heat Fluid Flow. 77 (2019) 48–60. doi:10.1016/j.ijheatfluidflow.2019.03.008.

[2] D.L. Hartmann, L.A. Moy, Q. Fu, Tropical Convection and the Energy Balance at the Top of the Atmosphere, J. Clim. 14 (2001) 4495–4511. doi:10.1175/1520-0442(2001)014<4495:TCATEB>2.0.CO;2.

[3] J. Marshall, F. Schott, Open-ocean convection: Observations, theory, and models, Rev. Geophys. 37 (1999) 1–64. doi:10.1029/98RG02739.

[4] T.M. Dokken, E. Jansen, Rapid changes in the mechanism of ocean convection during the last glacial period, Nature. 401 (1999) 458–461. doi:10.1038/46753.

[5] W.J. Morgan, Convection Plumes in the Lower Mantle, Nature. 230 (1971) 42–43. doi:10.1038/230042a0.

[6] D.P. Mckenzie, J.M. Roberts, N.O. Weiss, Convection in the earth's mantle: towards a numerical simulation, J. Fluid Mech. 62 (1974) 465. doi:10.1017/S0022112074000784.

[7] F. Cattaneo, T. Emonet, N. Weiss, On the Interaction between Convection and Magnetic Fields, Astrophys. J. 588 (2003) 1183–1198. doi:10.1086/374313.

[8] H.B. Awbi, A. Hatton, Natural convection from heated room surfaces, Energy Build. 30 (1999) 233–244. doi:10.1016/S0378-7788(99)00004-3.

[9] C. Beckermann, H.J. Diepers, I. Steinbach, A. Karma, X. Tong, Modeling melt convection in phase-field simulations of solidification, J. Comput. Phys. 154 (1999) 468–496. doi:10.1006/jcph.1999.6323.

[10] C.J. Chang, R.A. Brown, Radial segregation induced by natural convection and melt/solid interface shape in vertical bridgman growth, J. Cryst. Growth. 63 (1983) 343–364. doi:10.1016/0022-0248(83)90225-7.

[11] A. Bar-Cohen, W.W. Rohsenow, Thermally optimum spacing of vertical, natural convection cooled, parallel plates, J. Heat Transfer. 106 (1984) 116–123. doi:10.1115/1.3246622.

[12] S. Grossmann, D. Lohse, Scaling in thermal convection: a unifying theory, J. Fluid Mech. 407 (2000) 27–56. doi:10.1017/S0022112099007545.

[13] S. Grossmann, D. Lohse, Prandtl and Rayleigh number dependence of the Reynolds number in turbulent thermal convection, Phys. Rev. E. 66 (2002) 016305. doi:10.1103/PhysRevE.66.016305.

[14] R.J.A.M. Stevens, E.P. van der Poel, S. Grossmann, D. Lohse, The unifying theory of scaling in thermal convection: the updated prefactors, J. Fluid Mech. 730 (2013) 295–308. doi:10.1017/jfm.2013.298.

[15] B. Castaing, G. Gunaratne, F. Heslot, L. Kadanoff, A. Libchaber, S. Thomae, X.-Z. Wu, S. Zaleski, G. Zanetti, Scaling of hard thermal turbulence in Rayleigh-Bénard convection, J. Fluid Mech. 204 (1989) 1. doi:10.1017/S0022112089001643.

[16] F. Heslot, B. Castaing, A. Libchaber, Transitions to turbulence in helium gas, Phys. Rev. A. 36 (1987) 5870–5873. doi:10.1103/PhysRevA.36.5870.

[17] D. Funfschilling, E. Brown, A. Nikolaenko, G. Ahlers, Heat transport by turbulent Rayleigh-Bénard convection in cylindrical samples with aspect ratio one and larger, J. Fluid Mech. 536 (2005) 145–154. doi:10.1017/S0022112005005057.

[18] G. Ahlers, Low-temperature studies of the Rayleigh-Bénard instability and turbulence, Phys. Rev. Lett. 33 (1974) 1185–1188. doi:10.1103/PhysRevLett.33.1185.

[19] K.R. Sreenivasan, A. Bershadskii, J.J. Niemela, Mean wind and its reversal in thermal convection, Phys. Rev. E. 65 (2002) 056306. doi:10.1103/PhysRevE.65.056306.

[20] C. Sun, K.-Q. Xia, P. Tong, Three-dimensional flow structures and dynamics of turbulent thermal convection in a cylindrical cell, Phys. Rev. E. 72 (2005) 026302. doi:10.1103/PhysRevE.72.026302.

[21] J. Verdoold, M.J. Tummers, K. Hanjalić, Oscillating large-scale circulation in turbulent Rayleigh-Bénard convection, Phys. Rev. E. 73 (2006) 056304. doi:10.1103/PhysRevE.73.056304.

[22] S. Kenjereš, K. Hanjalić, Convective rolls and heat transfer in finite-length Rayleigh-Bénard convection: A two-dimensional numerical study, Phys. Rev. E. 62 (2000) 7987–7998. doi:10.1103/PhysRevE.62.7987.

[23] R. Du Puits, C. Resagk, A. Tilgner, F.H. Busse, A. Thess, Structure of

thermal boundary layers in turbulent Rayleigh–Bénard convection, J. Fluid Mech. 572 (2007) 231–254. doi:10.1017/S0022112006003569.

[24] C. Sun, Y.-H. Cheung, K.-Q. Xia, Experimental studies of the viscous boundary layer properties in turbulent Rayleigh–Bénard convection, J. Fluid Mech. 605 (2008) 79–113. doi:10.1017/S0022112008001365.

[25] J. Verdoold, M. van Reeuwijk, M.J. Tummers, H.J.J. Jonker, K. Hanjalić, Spectral analysis of boundary layers in Rayleigh-Bénard convection, Phys. Rev. E. 77 (2008) 016303. doi:10.1103/PhysRevE.77.016303.

[26] X.-Z. Wu, A. Libchaber, Non-Boussinesq effects in free thermal convection, Phys. Rev. A. 43 (1991) 2833–2839. doi:10.1103/PhysRevA.43.2833.

[27] G. Ahlers, F.F. Araujo, D. Funfschilling, S. Grossmann, D. Lohse, Non-Oberbeck-Boussinesq Effects in Gaseous Rayleigh-Bénard Convection, Phys. Rev. Lett. 98 (2007) 054501. doi:10.1103/PhysRevLett.98.054501.

[28] V. Valori, G. Elsinga, M. Rohde, M. Tummers, J. Westerweel, T. van der Hagen, Experimental velocity study of non-Boussinesq Rayleigh-Bénard convection, Phys. Rev. E. 95 (2017) 053113. doi:10.1103/PhysRevE.95.053113.

[29] E.D. Siggia, High Rayleigh number convection, Annu. Rev. Fluid Mech. 26(1) (1994) 137–168.

[30] G. Ahlers, S. Grossmann, D. Lohse, Heat transfer and large scale dynamics in turbulent Rayleigh-Bénard convection, Rev. Mod. Phys. 81 (2009) 503–537. doi:10.1103/revmodphys.81.503.

[31] T. Fusegi, J.M. Hyun, K. Kuwahara, B. Farouk, A numerical study of three-dimensional natural convection in a differentially heated cubical enclosure, Int. J. Heat Mass Transf. 34 (1991) 1543–1557. doi:10.1016/0017-9310(91)90295-P.

[32] F.X. Trias, M. Soria, A. Oliva, C.D. Perez-segarra, Direct numerical simulations of two- and three-dimensional turbulent natural convection flows in a differentially heated cavity of aspect ratio 4, J. Fluid Mech. 586 (2007) 259–293. doi:10.1017/S0022112007006908.

[33] P. Wang, Y. Zhang, Z. Guo, Numerical study of three-dimensional natural convection in a cubical cavity at high Rayleigh numbers, Int. J. Heat Mass Transf. 113 (2017) 217–228. doi:10.1016/j.ijheatmasstransfer.2017.05.057.

[34] M.R. Ravi, R.A.W.M. Henkes, C.J. Hoogendoorn, On the high-Rayleigh-

number structure of steady laminar natural-convection flow in a square enclosure, J. Fluid Mech. 262 (1994) 325. doi:10.1017/S0022112094000522.

[35] Y.S. Tian, T.G. Karayiannis, Low turbulence natural convection in an air filled square cavity: Part I: the thermal and fluid flow fields, Int. J. Heat Mass Transf. 43 (2000) 849–866. doi:10.1016/S0017-9310(99)00199-4.

[36] J. Salat, S. Xin, P. Joubert, A. Sergent, F. Penot, P. Le Quéré, Experimental and numerical investigation of turbulent natural convection in a large air-filled cavity, Int. J. Heat Fluid Flow. 25 (2004) 824–832. doi:10.1016/J.IJHEATFLUIDFLOW.2004.04.003.

[37] G. Biswas, N.K. Mitra, M. Fiebig, Computation of laminar mixed convection flow in a channel with wing type built-in obstacles, J. Thermophys. Heat Transf. 3 (1989) 447–453. doi:10.2514/3.28769.

[38] H. van Santen, C.R. Kleijn, H.E.A. van den Akker, On multiple stability of mixed-convection flows in a chemical vapor deposition reactor, Int. J. Heat Mass Transf. 44 (2001) 659–672. doi:10.1016/S0017-9310(00)00121-6.

[39] C.R. Kleijn, C.J. Hoogendoorn, A study of 2- and 3-D transport phenomena in horizontal chemical vapor deposition reactors, Chem. Eng. Sci. 46 (1991) 321–334. doi:10.1016/0009-2509(91)80141-K.

[40] A. Dogan, M. Sivrioglu, S. Baskaya, Experimental investigation of mixed convection heat transfer in a rectangular channel with discrete heat sources at the top and at the bottom, Int. Commun. Heat Mass Transf. 32 (2005) 1244–1252. doi:10.1016/J.ICHEATMASSTRANSFER.2005.05.003.

[41] E. Papanicolaou, Y. Jaluria, Mixed convection from simulated electronic components at varying relative positions in a cavity, J. Heat Transfer. 116 (2008) 960–970. doi:10.1115/1.2911472.

[42] P.F. Linden, The fluid mechanics of natural ventilation, Annu. Rev. Fluid Mech. 31 (1999) 201–238. doi:10.1146/annurev.fluid.31.1.201.

[43] Q.-H. Deng, J. Zhou, C. Mei, Y.-M. Shen, Fluid, heat and contaminant transport structures of laminar double-diffusive mixed convection in a two-dimensional ventilated enclosure, Int. J. Heat Mass Transf. 47 (2004) 5257–5269. doi:10.1016/j.ijheatmasstransfer.2004.06.025.

[44] H.J.S. Fernando, Fluid dynamics of urban atmospheres in complex terrain, Annu. Rev. Fluid Mech. 42 (2010) 365–389. doi:10.1146/annurev-fluid-

121108-145459.

[45] P.J.C. Schrijvers, H.J.J. Jonker, S. Kenjereš, S.R. de Roode, Breakdown of the night time urban heat island energy budget, Build. Environ. 83 (2015) 50–64. doi:10.1016/J.BUILDENV.2014.08.012.

[46] F.P. Incropera, J.S. Kerby, D.F. Moffatt, S. Ramadhyani, Convection heat transfer from discrete heat sources in a rectangular channel, Int. J. Heat Mass Transf. 29 (1986) 1051–1058. doi:10.1016/0017-9310(86)90204-8.

[47] C. Kuan-Cheng, J. Ouazzani, F. Rosenberger, Mixed convection between horizontal plates—II. Fully developed flow, Int. J. Heat Mass Transf. 30 (1987) 1655–1662. doi:10.1016/0017-9310(87)90311-5.

[48] H. Van Santen, C.R. Kleijn, H.E.. Van Den Akker, Mixed convection in radial flow between horizontal plates—II. Experiments, Int. J. Heat Mass Transf. 43 (2000) 1537–1546. doi:10.1016/S0017-9310(99)00233-1.

[49] S. Singh, M.A.R. Sharif, Mixed convective cooling of a rectangular cavity with inlet and exit openings on differentially heated side walls, Numer. Heat Transf. Part A Appl. 44 (2003) 233–253. doi:10.1080/716100509.

[50] E. Papanicolaou, Y. Jaluria, Mixed convection from an isolated heat source in a rectangular enclosure, Numer. Heat Transf. Part A Appl. 18 (1991) 427–461. doi:10.1080/10407789008944802.

[51] R. Iwatsu, J.M. Hyun, K. Kuwahara, Mixed convection in a driven cavity with a stable vertical temperature gradient, Int. J. Heat Mass Transf. 36 (1993) 1601–1608. doi:10.1016/S0017-9310(05)80069-9.

[52] M.K. Moallemi, K.S. Jang, Prandtl number effects on laminar mixed convection heat transfer in a lid-driven cavity, Int. J. Heat Mass Transf. 35 (1992) 1881–1892. doi:10.1016/0017-9310(92)90191-T.

[53] H.F. Oztop, I. Dagtekin, Mixed convection in two-sided lid-driven differentially heated square cavity, Int. J. Heat Mass Transf. 47 (2004) 1761–1769. doi:10.1016/J.IJHEATMASSTRANSFER.2003.10.016.

[54] P. Cheng, Heat Transfer in Geothermal Systems, Adv. Heat Transf. 14 (1979) 1–105. doi:10.1016/S0065-2717(08)70085-6.

[55] M. Nijemeisland, A.G. Dixon, Comparison of CFD simulations to experiment for convective heat transfer in a gas–solid fixed bed, Chem. Eng. J. 82 (2001) 231–246. doi:10.1016/S1385-8947(00)00360-0.

[56] K. Aziz, S.A. Bories, M.A. Combarnous, The Influence of natural convection in gas, oil and water reservoirs, J. Can. Pet. Technol. 12 (1973). doi:10.2118/73-02-05.

[57] R.L. Van Dam, C.T. Simmons, D.W. Hyndman, W.W. Wood, Natural free convection in porous media: First field documentation in groundwater, Geophys. Res. Lett. 36 (2009) L11403. doi:10.1029/2008GL036906.

[58] J.E. Weber, The boundary-layer regime for convection in a vertical porous layer, Int. J. Heat Mass Transf. 18 (1975) 569–573. doi:10.1016/0017-9310(75)90298-7.

[59] G.S. Shiralkar, M. Haajizadeh, C.L. Tien, Numerical study of high rayleigh number convection in a vertical porous enclosure, Numer. Heat Transf. 6 (1983) 223–234. doi:10.1080/01495728308963084.

[60] V. Prasad, F.A. Kulacki, Natural convection in a vertical porous annulus, Int. J. Heat Mass Transf. 27 (1984) 207–219. doi:10.1016/0017-9310(84)90212-6.

[61] D.R. Hewitt, J.A. Neufeld, J.R. Lister, High Rayleigh number convection in a three-dimensional porous medium, J. Fluid Mech. 748 (2014) 879–895. doi:10.1017/jfm.2014.216.

[62] R.A. Wooding, Steady state free thermal convection of liquid in a saturated permeable medium, J. Fluid Mech. 2 (1957) 273. doi:10.1017/S0022112057000129.

[63] S. Mahmud, I. Pop, Mixed convection in a square vented enclosure filled with a porous medium, Int. J. Heat Mass Transf. 49 (2006) 2190–2206. doi:10.1016/j.ijheatmasstransfer.2005.11.022.

[64] D. Poulikakos, A. Bejan, The departure from Darcy flow in natural convection in a vertical porous layer, Phys. Fluids. 28 (1985) 3477. doi:10.1063/1.865301.

[65] C. Beckermann, R. Viskanta, S. Ramadhyani, A numerical study of non-Darcian natural convection in a vertical enclosure filled with a porous medium, Numer. Heat Transf. 10 (1986) 557–570. doi:10.1080/10407788608913535.

[66] G. Lauriat, V. Prasad, Non-Darcian effects on natural convection in a vertical porous enclosure, Int. J. Heat Mass Transf. 47 (1989) 2135–2148.

[67] D.D. Joseph, D.A. Nield, G. Papanicolaou, Nonlinear equation governing

flow in a saturated porous medium, Water Resour. Res. 18 (1982) 1049–1052. doi:10.1029/WR018i004p01049.

[68] N. Kladias, V. Prasad, Experimental verification of Darcy-Brinkman-Forchheimer flow model for natural convection in porous media, J. Thermophys. Heat Transf. 5 (1991) 560–576. doi:10.2514/3.301.

[69] C.R.B. Lister, An explanation for the multivalued heat transport found experimentally for convection in a porous medium, J. Fluid Mech. 214 (1990) 287. doi:10.1017/S0022112090000143.

[70] D.J. Keene, R.J. Goldstein, Thermal convection in porous media at high Rayleigh numbers, J. Heat Transfer. 137 (2015) 034503. doi:10.1115/1.4029087.

[71] V. Prasad, F.A. Kulacki, M. Keyhani, Natural convection in porous media, J. Fluid Mech. 150 (1985) 89. doi:10.1017/S0022112085000040.

[72] N. Seki, S. Fukusako, H. Inaba, Heat transfer in a confined rectangular cavity packed with porous media, Int. J. Heat Mass Transf. 21 (1978) 985–989. doi:10.1016/0017-9310(78)90190-4.

[73] J.T. Hu, X.H. Ren, D. Liu, F.Y. Zhao, H.Q. Wang, Conjugate natural convection inside a vertical enclosure with solid obstacles of unique volume and multiple morphologies, Int. J. Heat Mass Transf. 95 (2016) 1096–1114. doi:10.1016/j.ijheatmasstransfer.2015.12.070.

[74] M.A. Delele, E. Tijskens, Y.T. Atalay, Q.T. Ho, H. Ramon, B.M. Nicolaï, P. Verboven, Combined discrete element and CFD modelling of airflow through random stacking of horticultural products in vented boxes, J. Food Eng. 89 (2008) 33–41. doi:10.1016/J.JFOODENG.2008.03.026.

[75] O. Laguerre, S. Ben Amara, J. Moureh, D. Flick, Numerical simulation of air flow and heat transfer in domestic refrigerators, J. Food Eng. 81 (2007) 144–156. doi:10.1016/J.JFOODENG.2006.10.029.

[76] A.A. Merrikh, J.L. Lage, Natural convection in an enclosure with disconnected and conducting solid blocks, Int. J. Heat Mass Transf. 48 (2005) 1361–1372. doi:10.1016/j.ijheatmasstransfer.2004.09.043.

[77] E.J. Braga, M.J.S. De Lemos, Heat transfer in enclosures having a fixed amount of solid material simulated with heterogeneous and homogeneous models, Int. J. Heat Mass Transf. 48 (2005) 4748–4765. doi:10.1016/j.ijheatmasstransfer.2005.05.016.

[78] A. Guardo, M. Coussirat, F. Recasens, M.A. Larrayoz, X. Escaler, CFD study on particle-to-fluid heat transfer in fixed bed reactors: Convective heat transfer at low and high pressure, Chem. Eng. Sci. 61 (2006) 4341–4353. doi:10.1016/j.ces.2006.02.011.

[79] A. Guardo, M. Coussirat, M.A. Larrayoz, F. Recasens, E. Egusquiza, Influence of the turbulence model in CFD modeling of wall-to-fluid heat transfer in packed beds, Chem. Eng. Sci. 60 (2005) 1733–1742. doi:10.1016/j.ces.2004.10.034.

[80] O. Laguerre, S. Ben Amara, G. Alvarez, D. Flick, Transient heat transfer by free convection in a packed bed of spheres: Comparison between two modelling approaches and experimental results, Appl. Therm. Eng. 28 (2008) 14–24. doi:10.1016/j.applthermaleng.2007.03.014.

[81] A. Raji, M. Hasnaoui, M. Naïmi, K. Slimani, M.T. Ouazzani, Effect of the subdivision of an obstacle on the natural convection heat transfer in a square cavity, Comput. Fluids. 68 (2012) 1–15. doi:10.1016/j.compfluid.2012.07.014.

[82] L.E. Howle, R.P. Behringer, J.G. Georgiadis, Convection and flow in porous media. Part 2. Visualization by shadowgraph, J. Fluid Mech. 332 (1997) 247–262. doi:10.1017/S0022112096004004.

[83] H. Lein, R.S. Tankin, Natural convection in porous media—I. Nonfreezing, Int. J. Heat Mass Transf. 35 (1992) 175–186. doi:10.1016/0017-9310(92)90018-N.

[84] K.J. Renken, D. Poulikakos, Mixed convection experiments about a horizontal isothermal surface embedded in a water-saturated packed bed of spheres, Int. J. Heat Mass Transf. 33 (1990) 1370–1373. doi:10.1016/0017-9310(90)90268-Y.

[85] Y.A. Hassan, E.E. Dominguez-Ontiveros, Flow visualization in a pebble bed reactor experiment using PIV and refractive index matching techniques, Nucl. Eng. Des. 238 (2008) 3080–3085. doi:10.1016/J.NUCENGDES.2008.01.027.

[86] O. Uzol, Y.-C. Chow, J. Katz, C. Meneveau, Unobstructed particle image velocimetry measurements within an axial turbo-pump using liquid and blades with matched refractive indices, Exp. Fluids. 33 (2002) 909–919. doi:10.1007/s00348-002-0494-8.

[87] M.K. Lyon, L.G. Leal, An experimental study of the motion of concentrated

suspensions in two - dimensional channel flow . Part 1 . Monodisperse systems, J. Fluid Mech. (2012). doi:10.1017/S0022112098008817.

[88] R. Häfeli, M. Altheimer, D. Butscher, P. Rudolf von Rohr, PIV study of flow through porous structure using refractive index matching, Exp. Fluids. 55 (2014) 1717. doi:10.1007/s00348-014-1717-5.

[89] K. Bai, J. Katz, On the refractive index of sodium iodide solutions for index matching in PIV, Exp. Fluids. 55 (2014) 1704. doi:10.1007/s00348-014-1704-x.

[90] D. Butscher, C. Hutter, S. Kuhn, P. Rudolf von Rohr, Particle image velocimetry in a foam-like porous structure using refractive index matching: a method to characterize the hydrodynamic performance of porous structures, Exp. Fluids. 53 (2012) 1123–1132. doi:10.1007/s00348-012-1346-9.

[91] E.R. Lapwood, Convection of a fluid in a porous medium, Math. Proc. Cambridge Philos. Soc. 44 (1948) 508. doi:10.1017/S030500410002452X.

[92] J. OTERO, L.A. DONTCHEVA, H. JOHNSTON, R.A. WORTHING, A. KURGANOV, G. PETROVA, C.R. DOERING, High-Rayleigh-number convection in a fluid-saturated porous layer, J. Fluid Mech. 500 (2004) 263–281. doi:10.1017/S0022112003007298.

[93] J.W. Elder, Steady free convection in a porous medium heated from below, J. Fluid Mech. 27 (1967) 29. doi:10.1017/S0022112067000023.

[94] M.D. Shattuck, R.P. Behringer, G.A. Johnson, J.G. Georgiadis, Convection and flow in porous media. Part 1. Visualization by magnetic resonance imaging, J. Fluid Mech. 332 (1997) 215–245. doi:10.1017/S0022112096003990.

[95] M.L. Byron, E.A. Variano, Refractive-index-matched hydrogel materials for measuring flow-structure interactions, Exp. Fluids. 54 (2013) 1456. doi:10.1007/s00348-013-1456-z.

[96] J.S. Weitzman, L.C. Samuel, A.E. Craig, R.B. Zeller, S.G. Monismith, J.R. Koseff, On the use of refractive-index-matched hydrogel for fluid velocity measurement within and around geometrically complex solid obstructions, Exp. Fluids. 55 (2014) 1862. doi:10.1007/s00348-014-1862-x.

[97] S. Klein, M. Gibert, A. Bérut, E. Bodenschatz, Simultaneous 3D measurement of the translation and rotation of finite-size particles and the

flow field in a fully developed turbulent water flow, Meas. Sci. Technol. 24 (2013) 024006. doi:10.1088/0957-0233/24/2/024006.

[98] A.R. Smith, Color gamut transform pairs, ACM SIGGRAPH Comput. Graph. 12 (1978) 12–19. doi:10.1145/965139.807361.

[99] S. Grossmann, D. Lohse, Scaling in thermal convection: a unifying theory, J. Fluid Mech. 407 (2000) S0022112099007545. doi:10.1017/S0022112099007545.

[100] D. Kunii, J.M. Smith, Heat transfer characteristics of porous rocks, AIChE J. 6 (1960) 71–78. doi:10.1002/aic.690060115.

[101] P. Zehner, E.U. Schlünder, Wärmeleitfähigkeit von Schüttungen bei mäßigen Temperaturen, Chemie Ing. Tech. 42 (1970) 933–941. doi:10.1002/cite.330421408.

[102] C.T. Hsu, P. Cheng, K.W. Wong, Modified Zehner-Schlunder models for stagnant thermal conductivity of porous media, Int. J. Heat Mass Transf. 37 (1994) 2751–2759. doi:10.1016/0017-9310(94)90392-1.

[103] W. van Antwerpen, C.G. du Toit, P.G. Rousseau, A review of correlations to model the packing structure and effective thermal conductivity in packed beds of mono-sized spherical particles, Nucl. Eng. Des. 240 (2010) 1803–1818. doi:10.1016/j.nucengdes.2010.03.009.

[104] D.R. Hewitt, J.A. Neufeld, J.R. Lister, Ultimate Regime of High Rayleigh Number Convection in a Porous Medium, Phys. Rev. Lett. 108 (2012) 224503. doi:10.1103/PhysRevLett.108.224503.

[105] V. Panjkovic, J.S. Truelove, P. Zulli, Numerical modelling of iron flow and heat transfer in blast furnace hearth, Ironmak. Steelmak. 29 (2002) 390–400. doi:10.1179/030192302225005187.

[106] K. Horikiri, Y. Yao, J. Yao, Numerical optimisation of thermal comfort improvement for indoor environment with occupants and furniture, Energy Build. 88 (2015) 303–315. doi:10.1016/J.ENBUILD.2014.12.015.

[107] G. Lauriat, V. Prasad, Natural Convection in a Vertical Porous Cavity: A Numerical Study for Brinkman-Extended Darcy Formulation, J. Heat Transfer. 109 (1987) 688. doi:10.1115/1.3248143.

[108] K.J. Schneider, Investigation of the influence of free thermal convection on heat transfer through granular material, in: Proc. 11th Int. Congr. Refrig., 1963: p. 4.

[109] D. Iyi, R. Hasan, R. Penlington, Experimental and numerical study of Buoyancy-driven low turbulence flow in rectangular enclosure partially filled with isolated solid blockages, Int. J. Heat Mass Transf. 127 (2018) 534–545. doi:10.1016/j.ijheatmasstransfer.2018.07.031.

[110] F. Bambauer, S. Wirtz, V. Scherer, H. Bartusch, Transient DEM-CFD simulation of solid and fluid flow in a three dimensional blast furnace model, Powder Technol. 334 (2018) 53–64. doi:10.1016/J.POWTEC.2018.04.062.

[111] O. Laguerre, S. Benamara, D. Remy, D. Flick, Experimental and numerical study of heat and moisture transfers by natural convection in a cavity filled with solid obstacles, Int. J. Heat Mass Transf. 52 (2009) 5691–5700. doi:10.1016/j.ijheatmasstransfer.2009.07.028.

[112] I. Ataei-Dadavi, M. Chakkingal, S. Kenjeres, C.R. Kleijn, M.J. Tummers, Flow and heat transfer measurements in natural convection in coarse-grained porous media, Int. J. Heat Mass Transf. 130 (2019) 575–584. doi:10.1016/j.ijheatmasstransfer.2018.10.118.

[113] Ergun, S., Fluid flow through packed columns, Chem. Eng. Prog. 48 (1952) 89–94.

[114] E. Tric, G. Labrosse, M. Betrouni, A first incursion into the 3D structure of natural convection of air in a differentially heated cubic cavity, from accurate numerical solutions, Int. J. Heat Mass Transf. 43 (2000) 4043–4056. doi:10.1016/S0017-9310(00)00037-5.

[115] J. Patterson, J. Imberger, Unsteady natural convection in a rectangular cavity, J. Fluid Mech. 100 (1980) 65. doi:10.1017/S0022112080001012.

[116] V. Prasad, A. Tuntomo, Inertia Effects On Natural Convection In A Vertical Porous Cavity, Numer. Heat Transf. 11 (1987) 295–320. doi:10.1080/10407788708913556.

[117] R.M. Fand, T.E. Steinberger, P. Cheng, Natural convection heat transfer from a horizontal cylinder embedded in a porous medium, Int. J. Heat Mass Transf. 29 (1986) 119–133. doi:10.1016/0017-9310(86)90040-2.

[118] L. Koufi, Z. Younsi, Y. Cherif, H. Naji, Numerical investigation of turbulent mixed convection in an open cavity: Effect of inlet and outlet openings, Int. J. Therm. Sci. 116 (2017) 103–117. doi:10.1016/j.ijthermalsci.2017.02.007.

[119] F.-Y. Zhao, D. Liu, G.-F. Tang, Multiple steady fluid flows in a slot-

ventilated enclosure, Int. J. Heat Fluid Flow. 29 (2008) 1295–1308. doi:10.1010.1016/j.ijheatfluidflow.2008.06.005.

[120] C.K. Cha, Y. Jaluria, Effect of thermal buoyancy on the recirculating flow in a solar pond for energy extraction and heat rejection, J. Sol. Energy Eng. 106 (1984) 428–437. doi:10.1115/1.3267622.

[121] C.K. Cha, Y. Jaluria, Recirculating mixed convection flow for energy extraction, Int. J. Heat Mass Transf. 27 (1984) 1801–1812. doi:10.1016/0017-9310(84)90162-5.

[122] A. Raji, M. Hasnaoui, Mixed convection heat transfer in a rectangular cavity ventilated and heated from the side, Numer. Heat Transf. Part A Appl. 33 (1998) 533–548. doi:10.1080/10407789808913953.

[123] A. Omri, S. Ben Nasrallah, Control volume finite element numerical simulation of mixed convection in an air-cooled cavity, Numer. Heat Transf. Part A Appl. 36 (1999) 615–637. doi:10.1080/104077899274606.

[124] D. Angirasa, Mixed convection in a vented enclosure with an isothermal vertical surface, Fluid Dyn. Res. 26 (2000) 219–233. doi:10.1016/S0169-5983(99)00024-6.

[125] J. Serrano-Arellano, J. Xamán, G. Álvarez, Optimum ventilation based on the ventilation effectiveness for temperature and CO2 distribution in ventilated cavities, Int. J. Heat Mass Transf. 62 (2013) 9–21. doi:10.1016/j.ijheatmasstransfer.2013.02.051.

[126] F.-Y. Zhao, D. Liu, L. Tang, Y.-L. Ding, G.-F. Tang, Direct and inverse mixed convections in an enclosure with ventilation ports, Int. J. Heat Mass Transf. 52 (2009) 4400–4412. doi:10.1010.1016/j.ijheatmasstransfer.2009.03.017.

[127] E. Bilgen, A. Muftuoglu, Cooling strategy by mixed convection of a discrete heater at its optimum position in a square cavity with ventilation ports, Int. Commun. Heat Mass Transf. 35 (2008) 545–550. doi:10.1016/j.icheatmasstransfer.2008.01.001.

[128] S. Kenjereš, S.B. Gunarjo, K. Hanjalić, Contribution to elliptic relaxation modelling of turbulent natural and mixed convection, Int. J. Heat Fluid Flow. 26 (2005) 569–586. doi:10.1016/j.ijheatfluidflow.2005.03.007.

[129] S. Murakami, S. Kato, T. Chikamoto, D. Laurence, D. Blay, New low-Reynolds-number k-ε model including damping effect due to buoyancy in a

stratified flow field, Int. J. Heat Mass Transf. 39 (1996) 3483–3496. doi:10.1016/0017-9310(95)00356-8.

[130] A.A. Bhuiyan, M.H. Banna, S.F. Barna, M.R. Amin, A.K.M. Sadrul Islam, Numerical modelling of thermal characteristics in a microstructure filled porous cavity with mixed convection, Int. J. Heat Mass Transf. 93 (2016) 464–476. doi:10.1016/j.ijheatmasstransfer.2015.10.004.

[131] N.S. Gibanov, M.A. Sheremet, M.A. Ismael, A.J. Chamkha, Mixed convection in a ventilated cavity filled with a triangular porous layer, Transp. Porous Media. 120 (2017) 1–21. doi:10.1007/s11242-017-0888-y.

[132] N.O. Moraga, G.C. Sánchez, J.A. Riquelme, Unsteady mixed convection in a vented enclosure partially filled with two non-darcian porous layers, Numer. Heat Transf. Part A Appl. 57 (2010) 473–495. doi:10.1080/10407781003659391.

[133] W.T. Cheng, C.N. Huang, S.W. Du, Three dimensional iron flow and heat transfer in the hearth of a blast furnace during tapping process, Chem. Eng. Sci. 60 (2005) 4485–4492. doi:10.1016/j.ces.2005.03.012.

[134] A. Ambaw, M.A. Delele, T. Defraeye, Q.T. Ho, L.U. Opara, B.M. Nicolaï, P. Verboven, The use of CFD to characterize and design post-harvest storage facilities: Past, present and future, Comput. Electron. Agric. 93 (2013) 184–194. doi:10.1016/j.compag.2012.05.009.

[135] I. Ataei-Dadavi, N. Rounaghi, M. Chakkingal, S. Kenjeres, C.R. Kleijn, M.J. Tummers, An experimental study of flow and heat transfer in a differentially side heated cavity filled with coarse porous media, Int. J. Heat Mass Transf. 143 (2019) 118591. doi:10.1016/j.ijheatmasstransfer.2019.118591.

[136] A. Acrivos, On the combined effect of forced and free convection heat transfer in laminar boundary layer flows, Chem. Eng. Sci. 21 (1966) 343–352. doi:10.1016/0009-2509(66)85027-3.

[137] S.W. Churchill, A comprehensive correlating equation for laminar, assisting, forced and free convection, AIChE J. 23 (1977) 10–16. doi:10.1002/aic.690230103.

[138] J.C. Hsieh, T.S. Chen, B.F. Armaly, Nonsimilarity solutions for mixed convection from vertical surfaces in porous media: variable surface temperature or heat flux, Int. J. Heat Mass Transf. 36 (1993) 1485–1493. doi:10.1016/S0017-9310(05)80059-6.

[139] T.S. Chen, B.F. Armaly, N. Ramachandran, Correlations for laminar mixed convection flows on vertical, inclined, and horizontal flat plates, J. Heat Transfer. 108 (1986) 835–840. doi:10.1115/1.3247020.

[140] M. Chakkingal, S. Kenjereš, I. Ataei-Dadavi, M.J. Tummers, C.R. Kleijn, Numerical analysis of natural convection with conjugate heat transfer in coarse-grained porous media, Int. J. Heat Fluid Flow. 77 (2019) 48–60. doi:10.1016/j.ijheatfluidflow.2019.03.008.

[141] S. Eckert, A. Cramer, G. Gerbeth, Velocity measurement techniques for liquid metal flows, Fluid Mech. Its Appl. 80 (2007) 275–294. doi:10.1007/978-1-4020-4833-3_17.

[142] S. Eckert, G. Gerbeth, Velocity measurements in liquid sodium by means of ultrasound Doppler velocimetry, Exp. Fluids. 32 (2002) 542–546. doi:10.1007/s00348-001-0380-9.

# List of Publications

## Journal Papers

- **Ataei-Dadavi, I.**, Chakkingal, M., Kenjeres, S., Kleijn, C. R., & Tummers, M. J. (2020). Experiments on mixed convection in a vented differentially side-heated cavity filled with a coarse porous medium. *International Journal of Heat and Mass Transfer*, 149, 119238.

- **Ataei-Dadavi, I.**, Rounaghi, N., Chakkingal, M., Kenjeres, S., Kleijn, C. R., & Tummers, M. J. (2019). An experimental study of flow and heat transfer in a differentially side heated cavity filled with coarse porous media. *International Journal of Heat and Mass Transfer*, 143, 118591.

- **Ataei-Dadavi, I.**, Chakkingal, M., Kenjeres, S., Kleijn, C. R., & Tummers, M. J. (2019). Flow and heat transfer measurements in natural convection in coarse-grained porous media. *International Journal of Heat and Mass Transfer*, 130, 575-584.

- Chakkingal, M., Schiavo, S., **Ataei-Dadavi, I.**, Tummers, M. J., Kleijn, C. R., & Kenjeres, S. (2020). Effect of packing height and location of porous media on heat transfer in a cubical cavity: Are extended Darcy simulations sufficient? *Accepted in International Journal of Heat and Fluid Flow*.

- Chakkingal, M., de Geus, J., Kenjeres, S., **Ataei-Dadavi, I.**, Tummers, M. J., & Kleijn, C. R. (2020). Assisting and opposing mixed convection with conjugate heat transfer in a differentially heated cavity filled with coarse-grained porous media. *International Communications in Heat and Mass Transfer*, 111, 104457.

- Chakkingal, M., Kenjeres, S., **Ataei-Dadavi, I.**, Tummers, M. J., & Kleijn, C. R. (2020). Numerical analysis of natural convection in a differentially heated packed bed with non-uniform wall temperature. *International Journal of Heat and Mass Transfer*, 149, 119168.

- Contreras, P. S., **Ataei-Dadavi, I.**, Speetjens, M. F. M., Kleijn, C. R., Tummers, M. J., & Clercx, H. J. H. (2019). Topological equivalence

between two classes of three-dimensional steady cavity flows: A numerical-experimental analysis. *Physics of Fluids*, 31(12), 123601.

- Chakkingal, M., Kenjeres, S., **Ataei-Dadavi, I.**, Tummers, M. J., & Kleijn, C. R. (2019). Numerical analysis of natural convection with conjugate heat transfer in coarse-grained porous media. *International Journal of Heat and Fluid Flow*, 77, 48-60.

## Conference papers

- **Ataei-Dadavi, I.**, Kenjeres, S., Kleijn, C. R., & Tummers, M. J. (2017). Natural convection heat transfer measurements in coarse-grained porous media. In *9th World Conference on Experimental Heat Transfer, Fluid Mechanics and Thermodynamics, Iguazu Falls, Brazil.*

## Conference presentations

- Presentation at 11$^{th}$ annual meeting of the International Society of Porous Media InterPore 2019, Valencia, Spain. (2019)
- Presentation at 21$^{st}$ Meeting Materials 2018, Noordwijkerhout, the Netherlands (2018)
- Presentation at J. M. Burgerscentrum Turbulence Contact Day, Delft, the Netherlands (2017)
- Presentation at 9$^{th}$ World Conference on Experimental Heat Transfer, Fluid Mechanics and Thermodynamics, Iguazu Falls, Brazil. (2017)

# Curriculum Vitae

## Iman Ataei Dadavi

05-04-1988 Born in Qaemshahr, Iran.

## Education and experience

1999 – 2006 High School Diploma in Mathematics & Physics
National Organization for Development of Exceptional Talents, Qaemshahr, Iran

2006 – 2010 BSc in Mechanical Engineering
Sharif University of Technology, Tehran, Iran
Thesis: "Modelling of Compressed Air Energy Storage (CAES) cycle and output optimization of Wind-CAES plants"

2010 – 2012 MSc in Aerospace Engineering – Aerodynamics & Propulsion
Sharif University of Technology, Tehran, Iran
Thesis: "Experimental study of flow characteristics in the wake of various V-shaped bluff bodies, using Particle Image Velocimetry"

2013 – 2014 Energy Engineer
Energy Systems Improvement Lab, Tehran, Iran

2014 – 2015 Research Scientist
Helmholtz Centre for Environmental Research, Halle, Germany

2015 – 2020 PhD in Chemical Engineering – Transport Phenomena
Delft University of Technology, Delft, The Netherlands
Thesis: "Experimental study of natural and mixed convection in coarse-grained porous media"

# Acknowledgements

After a Skype interview with Chris, Sasa, and Jos in March 2015, I was offered this very nice PhD position at TU Delft. At the same time, I got another offer from the University of Alberta, but finally, we decided to continue our journey in the Netherlands. We took a train from Germany to the Netherlands with a few suitcases on a sunny summer day on 17$^{th}$ July 2015. We arrived in Delft in the afternoon, put our stuff in our temporary 21 m$^2$ pre-arranged apartment, and then I immediately walked to the ChemE old building on Julianalaan to meet Chris before he leaves for a four-week holiday.

Now that I look back to this four-year journey at Delft, I see that it has been an amazing experience for me. It was a great opportunity to improve myself on technical grounds in the field of fluid dynamics and heat transfer and also interpersonally. I had the privilege of working with and meeting several great people from all around the world in and to learn from them.

First of all, I would like to thank my promoter Chris who has been very understanding and supportive all the way during my PhD. Thanks for giving me the freedom to become the project manager of my own project but at the same time being available whenever needed. Thanks for believing in me and guiding me through this challenging but beautiful path. You are a great leader. Thanks for understanding me during the most difficult time of my PhD when my brother-in-law passed away. I never forget your kindness when you offered your 7-seater car at the time my family was coming from Iran to visit me.

I am also very grateful to my daily supervisor Mark. You are an extremely pleasant person to work with. You could artfully make the ups and downs of my PhD life very smooth. I always felt relaxed and confident when talking with you about challenges. Thanks for all the frequent meetings and for thinking together with me towards finding solutions to different experimental and scientific puzzles. Your extensive experience and knowledge on optical measurement techniques have been very helpful to me. Also, thank you for reading my papers over and over again and providing me with detailed feedback.

Also many thanks to Sasa and Rob to be parts of my project team. Rob, although it was unfortunate that you left TP and therefore my project, I am proud to see that you are now the vice president of education at TU Delft. Sasa, thanks for all your useful and inspiring comments during the progress meetings and for always giving positive energy in difficult times.

I would like to thank our research technician Bart Hoek. Thanks for all your proficient technical and practical support in designing and preparation of the experimental setups. You are a very patient and knowledgeable person and you can come up with solutions for almost every practical problem. You have been like

a close friend of mine to whom I could openly talk about everything even about my personal life and career decisions.
My special thanks also go the involved people from the R&D department of our industrial partner, Tata Steel. Dirk, Sjaak, and Jan thanks for the great collaboration, fruitful discussions, and also your flexibility and support regarding my research directions. Also thanks to Viktoria from M2i for her continuous support. I would like to thank Sebastian from TU/e for our experimental-numerical collaboration which led to a great publication. Your dedication and commitment in this work is very much appreciated.
Although I have spent most of my time in the P&E lab and office, I have always considered the TP group as my main home and I truly enjoyed being a member of TP. Thank you Anita, Jennifer, and Sandra for your continuous support. Thank you Evert for all the time we spent together to conduct the liquid metal experiments and to jointly supervise Bachelor students. Thanks Christiaan for your technical support when needed especially with the electromagnetic flowmeter. Stefan, thanks for making very accurate components of the test cavities. Manu, thanks for always being available for scientific and non-scientific discussions and brain-storming. We have had a great experimental-numerical collaboration and we have published seven high-quality articles together. Aside from the scientific collaboration, we have always been good friends. Nima, you have contributed a lot in the third chapter of this thesis which is also published in IJHMT. I am really happy that our relationship has gone beyond a supervisor-student relationship and we have become life-long friends. Also thank you for providing the Dutch translation of my thesis summary. Anand, although we had only a year of overlap at TP, we have stayed in touch since then and became true friends. Thank you for being such a supportive and nice friend. Kevin and Wenji, I enjoyed sharing an office with you during the first year of my PhD. Elin, thank for caring about all PhD students in our group and trying to improve their PhD life. Sid, it was always nice to have chats with you on various topics such as Persian food and culture. Maulik and Manas, I have been always happy to have great friends like you in TP. Jasper, I enjoyed working with you and helping you towards finishing your BEP. Julia and Sabino, thanks for your great work together with Manu in our research project. Saeid and Ahad, it was always nice to have some Iranians in TP and have chats in Persian. Luis, David, Valeria, Cees, Gerasimos, Chirag, Annekatrien, Amin, Fei, Artem, Romana, Saidah, Lorentz, Matheus, Xiaolin, Kostadin, Peng, Debasish, Brice, thank for all the pleasant moments we have shared and thanks for making TP a great group to be part of.
I spent more than half of my PhD in my lab and office at the P&E department at 3ME. I would like to thank all the nice people who made my stay at P&E very pleasant. Edwin, thank you for your help with setting up the PIV system. Jaap,

thanks for all your support in the P&E lab while having a permanent smile on your face. Mohammad, you made working in our windowless laser lab very enjoyable during the year we shared the same lab. Thanks for all the funny moments you created in the lab, our lunch and coffee breaks, and the joyful discussions on socio-political topics. Liangyuan thank for all the evenings we have worked till late in the office. Johan, Hadi, Aviral, Rong, Hengame, Shilong, Simone, Boaz, Nandalal, and Daniel, I enjoyed sharing the same office with you during the last year of my PhD and having chats during coffee and lunch times. Xu, Yashar, Ali, Elyas, Mohsen, Seyed, Parviz, Ankur, Filippo, it was all nice to have you around in P&E and have chats once in a while near the coffee machine.

Last but not least, I would like to thank my family. My lovely wife, Afsane, many thanks for your unconditional love and support during my PhD. You have been my best friend to whom I could share all my stressful and frustrating moments. Thank you for always being there for me and for keeping my spirits high during all difficult times. I love you. My beloved mom and dad thank you for years of continuous support, love, and devotion and your special attention to my studies. Dad, you are not in this world now but you are always in my heart and I am grateful to you for all my achievements. Thank you my dear brother and sister, Ehsan and Afrough for always being by my side and for supporting me through different stages of my life. Also, many thanks to my father-in-law, my mother-in-law, and my sister-in-law Eli, who have been always very supportive and motivative during the challenging years of my PhD.